UNIVERSIDADE DO PORTO

FACULDADE DE ENGENHARIA

Master's Thesis

Design and Analysis of Hybrid Composite Shields for Military Aircraft

Catarina Gonçalves Rodrigues da Silva

Supervisor: Volnei Tita

Thesis submitted to Universidade do Porto – Faculdade de Engenharia
in partial fulfillment of the requirements for the degree of
Master in Mechanical Engineering - Aeronautical and Vehicles Structures

MEM

U. PORTO

FEUP FACULDADE DE ENGENHARIA UNIVERSIDADE DO PORTO

DEPARTAMENTO DE ENGENHARIA MECÂNICA

Faculdade de Engenharia

September, 2025

Candidate: Catarina Gonçalves Rodrigues da Silva, No. 202008517, up202008518@up.pt

Scientific Guidance: Prof. Dr. Volnei Tita, voltita@sc.usp.br

DEPARTAMENTO DE ENGENHARIA MECÂNICA
Faculdade de Engenharia
Rua Dr. Roberto Frias, Porto

September, 2025

"Engineers like to solve problems. If there are no problems handily available, they will create their own."

Scott Adams

Acknowledgements

I would like to express my heartfelt gratitude to Professor Dr. Volnei Tita for his constant guidance, insightful feedback, and steadfast backing throughout my research. His mentorship has been crucial in navigating the challenges of this work and has enriched my learning experience.

I am also especially grateful to Professor Marco Parente for his invaluable assistance in the simulation process. His availability, technical insight, and the computational resources he provided, including access to a dedicated machine that significantly accelerated my work, were instrumental to the development of this thesis.

My sincere thanks go as well to André Rocha, who was always available when I faced greater difficulties. His clear guidance, patience, and consistent assistance were key to helping me stay on track and complete this work with confidence.

To my family, I owe a profound debt of gratitude. To my parents, Carla and Arménio, and my sister Carolina, thank you for your endless love, patience, and encouragement. Your unfailing backing through every step of this journey has been the foundation that kept me going, and this accomplishment is as much yours as it is mine.

To my godmother Belmira, thank you for reading my thesis over and over again with care and attention. Your help, time, and genuine interest meant more than I can express.

Furthermore, I wish to acknowledge my friends from both my bachelor's and master's studies. Their camaraderie, stimulating discussions, and encouragement have not only made this journey enjoyable but have also helped me overcome difficult moments along the way.

This thesis is the result of the contributions and assistance of all these remarkable people, and I am truly grateful for their part in this chapter of my life.

Abstract

Composite materials are widely used in civil and military aviation because of their high specific stiffness and strength. Defence applications adopted them early due to performance-driven requirements. Beyond primary structures, composites enable lighter ballistic protection than metallic solutions. Recent work has focused on hybrid laminates that combine ceramics and polymer composites to improve resistance under high-velocity impact.

This dissertation develops and evaluates an explicit finite element framework in Abaqus/-Explicit to study normal high-velocity impact on alumina and composite targets. The targets use a 10 mm alumina strike face and a 4.8 mm laminate backing. Impacts at 400 m/s and 600 m/s are simulated with a rigid projectile. Alumina behaviour follows the Johnson–Holmquist II (JH-2) model. Composite intralaminar failure is captured with a three dimensional (3D) Hashin formulation implemented in a Vectorized User Material subroutine (VUMAT). Interlaminar damage in Carbon Fiber Reinforced Polymers (CFRP) is modelled with a cohesive zone approach in Abaqus. Interfaces in the Ultra-High Molecular Weight Polyethylene (UHMWPE) laminate are tied to focus on intralaminar response.

Mesh and time increment choices follow wave resolution and stability criteria to ensure consistent comparison across materials. Results show distinct arrest mechanisms for CFRP and UHMWPE backings. For CFRP, the projectile is arrested at 400 m/s with an absorbed energy plateau of approximately 900 J and an interaction time of approximately 150 microseconds. At 600 m/s, the projectile perforates the CFRP, and the absorbed energy exceeds 1800 J without reaching a plateau, which indicates residual velocity. For UHMWPE, the projectile is arrested at both velocities. The absorbed energy reaches 900 J at 400 m/s and 1900 J at 600 m/s, with clear plateaus and faster deceleration. The UHMWPE configuration achieves improved stopping capability at the cost of larger rear face deflection, especially at 600 m/s.

The study consolidates a practical workflow that couples JH-2 ceramics with a VUMAT-based Hashin formulation for composites, cohesive interlaminar modelling for CFRP, and tied interfaces for UHMWPE. It provides model setup guidance and post-impact metrics that support early design screening of hybrid armour concepts.

Keywords: Ballistic impact, Hybrid armour, Alumina, CFRP, UHMWPE, Abaqus Explicit, Hashin failure, Cohesive zone model, JH-2.

Resumo

Os materiais compósitos são amplamente utilizados na aviação civil e militar devido à sua elevada rigidez e resistência específicas. As aplicações de defesa adotaram-nos cedo por exigirem desempenho elevado. Para além das estruturas primárias, os compósitos permitem soluções de proteção balística mais leves do que as metálicas. A investigação recente tem-se concentrado em laminados híbridos que combinam cerâmicas e compósitos poliméricos para melhorar a resistência sob impacto de alta velocidade.

Esta dissertação desenvolve e avalia uma metodologia explícita de elementos finitos no Abaqus/Explicit para estudar o impacto normal de alta velocidade em alvos híbridos de alumina e compósito. Os alvos incluem uma face de impacto em alumina com 10 mm e um laminado de suporte com 4.8 mm. Simulam-se impactos a 400 m/s e 600 m/s com um projétil rígido. O comportamento da alumina segue o modelo Johnson–Holmquist II. A falha intralaminar do compósito é descrita com uma formulação de Hashin tridimensional implementada numa sub-rotina VUMAT. A danificação interlaminar no compósito de fibra de carbono e epóxi é modelada com uma zona coesiva no Abaqus. Nas simulações com polietileno de ultra alto peso molecular, as interfaces do laminado são modeladas com ligações do tipo tied para focar a resposta intralaminar.

As escolhas de malha e de incremento temporal seguem critérios de resolução de ondas e de estabilidade para garantir uma comparação coerente entre materiais. Os resultados evidenciam mecanismos de paragem distintos para o laminado de fibra de carbono/epóxi e para o laminado de polietileno de ultra alto peso molecular. No compósito de fibra de carbono e epóxi, o projétil é imobilizado a 400 m/s, com um patamar de energia absorvida de aproximadamente 900 J e um tempo de interação de aproximadamente 150 microsegundos. A 600 m/s ocorre perfuração, e a energia absorvida ultrapassa 1800 J sem atingir patamar, o que indica velocidade residual. No polietileno de ultra alto peso molecular, o projétil é imobilizado em ambas as velocidades. A energia absorvida atinge cerca de 900 J a 400 m/s e cerca de 1900 J a 600 m/s, com patamares claros e desaceleração mais rápida. Esta configuração melhora a capacidade de paragem à custa de maior deflexão da face traseira, especialmente a 600 m/s.

O estudo consolida um fluxo de trabalho prático que combina a modelação JH-2 para a cerâmica com a formulação de Hashin numa sub-rotina VUMAT para o compósito, a modelação coesiva interlaminar para o laminado de fibra de carbono/epóxi e ligações tied no laminado de polietileno de ultra alto peso molecular. São fornecidas orientações de configuração do modelo e métricas pós-impacto que apoiam a seleção preliminar de soluções de

blindagem híbrida.

Palavras-Chave: Impacto balístico, Blindagem híbrida, Alumina, Compósito de fibra de carbono e epóxi, Polietileno de ultra alto peso molecular, Abaqus Explicit, Critério de falha de Hashin, Modelo de zona coesiva, JH-2.

UN Sustainable Development Goals

This dissertation aligns its innovations in sustainable materials, efficient structural design, and enhanced protection technologies with several United Nations Sustainable Development Goals (SDGs). The selected goals are drawn directly from the official UN SDG descriptions to ensure fidelity to their original framing [1]. Below are the identified SDGs that resonate most with this research:

- **SDG 9** – Industry, Innovation and Infrastructure: Build resilient infrastructure, promote inclusive and sustainable industrialization and foster innovation.
- **SDG 12** – Responsible Consumption and Production: Ensure sustainable consumption and production patterns.
- **SDG 13** – Climate Action: Take urgent action to combat climate change and its impacts.
- **SDG 16** – Peace, Justice and Strong Institutions: Promote peaceful and inclusive societies for sustainable development, provide access to justice for all and build effective, accountable and inclusive institutions at all levels.

Table 1: Relevant UN Sustainable Development Goals for this dissertation [1].

SDG	**Goal**	**Relevance to this dissertation**
9	Industry, innovation and infrastructure	This research advances resilient and sustainable infrastructure by developing novel composite structures integrating design innovation in lightweight materials that support efficient aerospace and defence systems.
12	Responsible consumption and production	By employing advanced composites efficiently and optimising material use, the work promotes environmentally responsible production, reduced waste, and circularity in advanced structural design.
13	Climate action	The creation of lightweight, durable structural elements contributes to lower system energy demands and helps decarbonise transportation and defence, mitigating climate impact.
16	Peace, justice and strong institutions	Improved ballistic and protective technologies support security and peacekeeping efforts, indirectly fostering societal stability and safe environments.

Contents

List of Figures

List of Tables

Listings

List of Acronyms

2D	two dimensional
3D	three dimensional
AFLCMC	Air Force Life Cycle Management Center
AMC	Acceptable Means of Compliance
B-K	Benzeggagh–Kenane
CAE	Computer-Aided Engineering
CFRP	Carbon Fiber Reinforced Polymers
CP	Complete Penetration
CPU	Central Processing Unit
DOA	Design Organisation
DoD	Department of Defense
EASA	European Union Aviation Safety Agency
EDA	European Defence Agency
EMADs	European Military Airworthiness Documents
EMARs	European Military Airworthiness Requirements
EMDOA	European Military Design Organisation Approval
EOS	equation of state
EU	European Union
FAA	Federal Aviation Administration
FEM	Finite Element Method
FRP	Fibre-Reinforced Polymer
GUI	Graphical User Interface

HEL	Hugoniot Elastic Limit
JH-2	Johnson–Holmquist II
MAA	Military Aviation Authority
MAWA	Military Airworthiness Authorities
MFTP	Military Flight Test Permit
MTC	Military Type Certificate
NAMP	Naval Aviation Maintenance Program
NAVAIR	Naval Air Systems Command
PAN	Polyacrylonitrile
PEEK	polyether ether ketone
PEKK	polyether ketone ketone
PP	Partial Penetration
PPS	polyphenylene sulfide
RTS	Release to Service
TAA	Technical Airworthiness Authority
UD	unidirectional
UHMWPE	Ultra-High Molecular Weight Polyethylene
US	United States
USAF	United States Air Force
VUMAT	Vectorized User Material subroutine

List of Symbols

Symbol	Description	Units
α	Exponent in power law fracture energy interaction	-
β	Mode mixity ratio between shear and normal displacement	-
$\mathbf{C}$	Damping matrix	N·s/m
$\mathbf{C}_0$	Undamaged stiffness tensor	MPa
$\mathbf{C}_d$	Damaged stiffness tensor	MPa
d	Scalar damage variable	-
δ_0	Initial displacement at which softening begins	mm
δ_1'	First shear component of relative displacement for decohesion	mm
δ_2'	Second shear component of relative displacement for decohesion	mm
δ_3	Normal component of relative displacement for decohesion	mm
δ_{eff}	Effective displacement magnitude across the interface	mm
δ_{eff}^0	Effective displacement at onset of damage	mm
δ_{eff}^f	Effective displacement at complete failure	mm
$\delta_{\text{eff}}^{\max}$	Maximum effective displacement over the loading history	mm
δ_f	Final displacement used in softening law	mm

Symbol	Description	Units
$\delta^0_{I,\mathrm{eq}}$	Threshold equivalent displacement for onset of damage	mm
$\delta_{I,\mathrm{eq}}$	Equivalent displacement for failure mode I	mm
$\delta^0_{I,\mathrm{eq}}$	Equivalent displacement at damage initiation for mode I	mm
$\delta^f_{I,\mathrm{eq}}$	Equivalent displacement at full failure for mode I	mm
$\delta^f_{I,\mathrm{eq}}$	Final equivalent displacement corresponding to full failure	mm
δ'_m	Critical relative displacement for complete decohesion	mm
δ_n	Relative displacement in the normal direction	mm
δ_s	Relative displacement in the first tangential direction	mm
δ_t	Relative displacement in the second tangential direction	mm
d_I	Damage variable associated with failure mode I	-
$\mathbf{D}$	Diagonal matrix of damage variables for each failure mode	-
E_1	Young's modulus in the fibre direction	GPa
E_2	Young's modulus in the transverse direction	GPa
$\dot{\varepsilon}_0$	Reference strain rate	s^{-1}
$\varepsilon_{f\max}$	Maximum failure strain	-
$\varepsilon_{f\min}$	Minimum failure strain	-
ε	Strain tensor	-
η	Exponent in B-K fracture energy interaction law	-
f	External force vector	N
F_s	Failure criterion scaling factor	-
G	Shear modulus	GPa

Symbol	Description	Units
G_{12}	Shear modulus in the 1-2 plane	GPa
G_{23}	Shear modulus in the 2-3 plane	GPa
G_c	Fracture energy (area under traction–displacement curve)	N/mm
G_{fc}	Fracture toughness under compression	N/mm
G_{ft}	Fracture toughness under tension	N/mm
G_I	Mode I energy release rate	N/mm
G_{IC}	Mode I critical fracture energy	N/mm
G_i^C	Critical energy release rate	N/mm
G_{II}	Mode II energy release rate	N/mm
G_{IIC}	Mode II critical fracture energy	N/mm
G_{III}	Mode III energy release rate	N/mm
G_{mc}	Fracture toughness under compression	N/mm
G_{mt}	Fracture toughness under tension	N/mm
G_{shear}	Shear energy release rate $(G_{II}+G_{III})$	N/mm
G_T	Total energy release rate $(G_I+G_{II}+G_{III})$	N/mm
$\mathbf{K}$	Stiffness matrix	N/m
K_i	Interface initial stiffness	N/mm^3
K_n	Penalty stiffness in the normal direction	N/mm^3
K_s	Penalty stiffness in the first tangential direction	N/mm^3
K_t	Penalty stiffness in the second tangential direction	N/mm^3
$\mathbf{M}$	Mass matrix	kg
ν_{12}	Poisson's ratio in the 1-2 plane	-
ν_{23}	Poisson's ratio in the 2-3 plane	-

Symbol	Description	Units
P_{Hel}	Pressure at Hugoniot Elastic Limit	GPa
ρ	Density	kg/m^3
S_{12}	Strength in the 1-2 plane	MPa
S_{13}	Shear strength in the 1-3 plane	MPa
S_{23}	Strength in the 2-3 plane	MPa
σ_{11}	Normal stress in the fibre direction	MPa
σ_{12}	Shear stress in the 1-2 plane	MPa
σ_{13}	Shear stress in the 1-3 plane	MPa
σ_{22}	Normal stress in the transverse direction	MPa
σ_{23}	Shear stress in the 2-3 plane	MPa
σ_{33}	Normal stress in the thickness direction	MPa
$\sigma_{f\text{max}}$	Maximum failure stress	GPa
$\sigma_{I\text{max}}$	Maximum principal stress	GPa
σ	Cauchy stress tensor	MPa
T	Engineer stress tensor	MPa
t_0	Stress at damage initiation	MPa
T_{eff}^0	Initial effective traction at damage onset	MPa
t_i^{max}	Interfacial strength	MPa
$\mathbf{T}$	Transformation matrix from local to global coordinates	-
t_n	Normal across the interface	MPa
$t_{n,\text{max}}$	Critical normal for damage initiation	MPa
t_s	Shear in the first tangential direction	MPa
$t_{s,\text{max}}$	Critical tangential shear for damage initiation	MPa
t_t	Shear in the second tangential direction	MPa
$t_{t,\text{max}}$	Critical transverse shear for damage initiation	MPa
$\ddot{u}$	Acceleration vector	m/s^2
u	Displacement vector	m

Symbol	Description	Units
$\dot{u}$	Velocity vector	m/s
X_c	Compressive strength in the fibre direction	MPa
X_t	Tensile strength in the fibre direction	MPa
Y_c	Compressive strength in the transverse direction of the fibre	MPa
Y_t	Tensile strength in the transverse direction of the fibre	MPa

Chapter 1

Introduction

1.1 Contextualisation and Objectives

In recent years, composite materials have become central to modern aircraft owing to their high specific stiffness and strength. Their introduction in civil aviation was initially conservative, largely because of certification requirements and the necessity to demonstrate long-term durability, inspectability and repairability. Once established, the benefits became clear: lower structural mass leading to reduced fuel burn, improved payload margins and opportunities for aerodynamic optimisation [2]. Today, wide-body platforms such as the Boeing 787 and Airbus A350 include on the order of half of their structural weight in composites [3]–[6].

In military aviation, the adoption of composites has been driven primarily by performance, including speed, manoeuvrability, range and mission capability, which has allowed earlier and broader use than in the civil sector [7], [8]. Beyond airframe efficiency, composites have also been investigated for ballistic protection. Traditional armour solutions based on steel or titanium provide localised protection but at a significant weight penalty, which can compromise aircraft performance. CFRP deliver excellent stiffness and load-bearing capacity, yet their brittle failure mechanisms and propensity for delamination limit their ability to absorb the energy of high-velocity projectiles [9]. UHMWPE laminates, by contrast, exhibit high strain-to-failure and pronounced energy dissipation capacity, making them attractive as backing layers in hybrid armour concepts [10].

In this sense, the main motivation behind this dissertation is the assessment of hybrid composite targets for the ballistic protection of military aircraft, with particular focus on the effect of replacing a conventional CFRP backing with UHMWPE. The design of protective structures of this type may be divided into conceptual, preliminary and detailed phases. Since this work represents an initial approach to the problem, it is positioned within the conceptual stage, where absolute optimisation of weight and thickness is considered secondary.

The primary objective of this dissertation is therefore to evaluate numerical modelling strategies capable of simulating ceramic–composite laminates under high-velocity impact. Explicit dynamic analyses are employed using 3D models that incorporate strain-rate dependence in the composite material definition. Cohesive elements are not used in the UHMWPE simulations, although the implications of this modelling choice are discussed.

1.2 Methodology

The research follows a simulation-driven strategy based entirely on 3D explicit dynamics. The reference configuration consists of a hybrid target composed of a ceramic strike face and a composite backing. The ceramic layer is described using a high strain rate brittle constitutive model appropriate for impact loading, namely the Johnson–Holmquist II (JH-2) formulation as implemented in Abaqus/Explicit. The backing is defined ply by ply through orthotropic elasticity combined with mode specific failure criteria, implemented in a user-defined material subroutine called VUMAT, which is based on the 3D Hashin formulation. Strain rate dependence is included in the composite response to capture the strength enhancement observed under ballistic loading conditions.

All components, including the projectile, the ceramic plate and the laminate plies, are modelled with three dimensional solid elements, and interactions use general contact. The two backings differ only in their interlaminar treatment. In the CFRP case, adjacent plies are bonded by epoxy interfaces defined in Abaqus with a surface based cohesive traction separation law. When the cohesive damage criterion is met, stiffness decreases and the interface can open or slide under contact. In the UHMWPE case, ply interfaces are tied, so delamination is suppressed and the response is governed by intralaminar failure within the plies. This arrangement maintains stable explicit time integration while capturing the distinct through thickness behaviour of each backing.

Impacts at 400 m/s and 600 m/s are applied to both configurations. The comparison focuses on projectile residual velocity, the time history of absorbed energy, and the spatial distribution of damage in the backing. To ensure a fair assessment, all other modelling choices, including element formulation, mesh, contact settings, time step control and requested outputs, are kept identical across cases.

1.3 Document Organization

The structure of the document is presented below. The chapters follow the order in which the project is developed, emphasising the progressive approach to the problem.

Chapter 1 - Presents the context and motivation for ballistic protection using composites in military aviation, states the objectives, summarises the modelling methodology, and outlines the document.

Chapter 2 - Provides a literature review that serves as the theoretical foundation for the dissertation. It begins with an overview of composite materials and laminated structures in aerospace applications, followed by the certification framework of military aircraft and the requirements for ballistic protection systems. The chapter also reviews the development of hybrid armour concepts and concludes with an introduction to numerical modelling approaches, focusing on explicit dynamic simulations for impact problems.

Chapter 3 - Describes in detail the constitutive models and failure criteria employed in the numerical simulations. It explains the 3D Hashin formulation used for intralaminar failure in the composite plies, its implementation in a user-defined VUMAT subroutine, and the associated property degradation laws. Considerations for interlaminar modelling and the JH-2 model for ceramics are also addressed, providing the theoretical framework required for the subsequent case studies.

Chapter 4 - Details the finite element model setup in Abaqus/Explicit and reports high-velocity impact results for the ceramic/CFRP target, including projectile kinematics, absorbed energy histories and damage fields.

Chapter 5 - Adapts the model to UHMWPE plies, presents the corresponding ballistic simulations, and compares the outcomes with the CFRP baseline to assess potential advantages and trade-offs.

Chapter 6 - Summarises the main findings relative to the stated objectives and outlines recommendations for further development, including model refinements and experimental validation.

Chapter 2

Literature Review

2.1 Composite Materials

The use of composite materials dates back to ancient civilizations, with early examples such as mud bricks reinforced with straw [11]. However, the modern era of composites began in the 20th century with the industrial production of glass fibre composites, followed by the introduction of carbon fibre composites in the 1960s, which significantly advanced their structural capabilities [12]. Since then, composites have become essential in demanding engineering applications where high specific strength and stiffness are required.

Composite materials are engineered heterogeneous systems composed of two or more distinct phases, typically consisting of high-performance fibres embedded in a polymeric matrix. While the fibres, such as carbon or aramid, provide strength and stiffness, the matrix, usually a thermoset or thermoplastic resin, serves to maintain the geometric arrangement of the fibres, transfer loads between them, and protect them from environmental damage [13], [14].

In structural composites, the fibre-matrix architecture is fundamental. The fibre acts as the primary load-bearing component, while the matrix distributes stress and supports the fibres against buckling and environmental effects. The properties of the resulting material system can be tailored through the selection of fibre type, volume fraction, and orientation, offering significant advantages over monolithic materials [15], [16]. Generally, a composite material consists of two primary constituents: the matrix and the reinforcement, as depicted in the following Figure 2.1. The reinforcement refers primarily to the fibre phase, which is responsible for providing strength and stiffness to the composite and constitutes its critical load-bearing element [17].

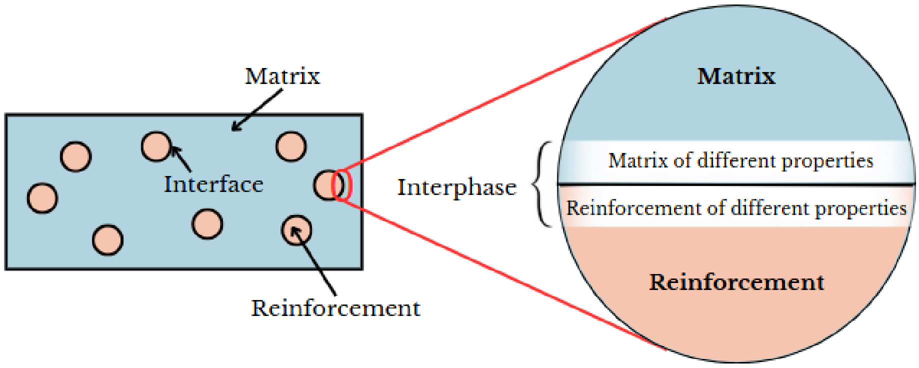

Figure 2.1: Schematic representation of the two primary constituents of a composite material.

The following subsections will provide a detailed analysis of the main constituents of composite materials, focusing on the different types of reinforcement fibres and matrix systems. Their individual properties, roles, and interactions will be examined to support a deeper understanding of the mechanical performance of composite structures in advanced applications.

2.1.1 Reinforcements

Reinforcements in composite materials are essential for enhancing the mechanical properties of the resin system, contributing significantly to the overall strength, stiffness, and durability of the composite. These reinforcements, usually composed of strong materials with defined morphologies, are incorporated into the matrix to enhance its physical properties. The selection and arrangement of reinforcement fibres are critical, as they directly influence the composite's performance in various applications [18], [19].

In practice, fibres are often organised into sheets or fabrics to facilitate handling and processing. Because different types of reinforcements possess unique mechanical and physical properties, their incorporation into the composite results in diverse performance outcomes. Therefore, the final properties of a composite material are inherently dependent on the nature of the reinforcement, its quantity, and its configuration within the matrix, allowing composites to be categorised according to their reinforcement types [17].

In the present work, the focus will be placed on both synthetic and organic fibre reinforcements that are most relevant to high-performance structural and ballistic applications. Specifically, carbon fibres and glass fibres are considered for their widespread use and well-documented balance of strength, stiffness, and cost-effectiveness. In addition, two high-performance synthetic organic fibres, such as aramid and UHMWPE, are examined in detail due to their outstanding impact resistance and specific strength. This selection reflects the materials most commonly employed in aerospace, automotive, and personal protection systems, and provides a representative overview of the reinforcement types relevant to the modelling and experimental work undertaken in this study [20].

2.1.1.1 Carbon Fibres

Carbon fibre reinforcement is renowned for its exceptional mechanical properties, including high tensile strength and low density. Carbon fibres exhibit a tensile strength seven to ten times greater than that of steel with the same cross-sectional area, offering an exceptional strength-to-weight ratio. This makes them especially valuable in weight-sensitive applications, such as aerospace and structural components [9].

Polyacrylonitrile (PAN) is the primary precursor for carbon fibre production, accounting for about 90% of the global market, owing to its ability to produce high-performance fibres with a high carbon content. The manufacturing process involves multiple stages. Initially, PAN fibres are subjected to thermal stabilization in an oxygen-rich environment at temperatures between 200°C and 300°C. During this phase, the molecular structure of the fibres is altered into a ladder-like arrangement, increasing their thermal stability [21].

Following stabilization, the fibres undergo carbonization in an inert atmosphere at temperatures exceeding 1000°C, converting the ladder structure into a planar configuration composed predominantly of carbon. This transformation results in carbon content levels of approximately 95%, though further treatment at temperatures ranging from 1982.22°C to 3037.78°C can increase the carbon content to around 99%, producing highly graphitic fibres [21], [22].

The final stages of carbon fibre production involve surface treatment and sizing, during which the fibre surfaces are etched to improve adhesion with resin matrices. A protective coating, often an epoxy, is then applied to prevent surface damage and to optimize interfacial bonding during composite manufacturing [21].

Carbon fibres are primarily characterized by their graphitic structure, consisting of carbon atoms arranged in a hexagonal lattice. This structure imparts significant anisotropy, resulting in a high modulus along the layer plane, potentially reaching 1000 GPa, while the modulus along the c-axis remains comparatively lower, at approximately 35 GPa [22]. The density of carbon fibres varies based on the precursor and processing parameters, typically ranging from 1.6 to 2.2 g/cm^3, with PAN-based fibres exhibiting densities between 1.75 and 1.93 g/cm^3 [22], [23].

2.1.1.2 Glass Fibres

Glass fibres are widely used as synthetic reinforcements in polymer composites due to their high tensile strength, cost-effectiveness, and chemical resistance. Additionally, they exhibit excellent insulating properties, making them suitable for electrical and thermal applications. Despite their advantages, these materials also pose challenges, including high density, vulnerability to abrasion, and relatively low fatigue resistance, all of which can affect negatively the structural performance during handling and extended use [22].

The production of glass fibres involves two main methods: the indirect marble melting process and the direct melt process. In the indirect method, raw materials are first formed into glass marbles measuring 15 to 20 mm in diameter, which are then re-melted and extruded into fibres. The direct melt process bypasses the intermediate cooling stage, allowing the raw materials to be melted and extruded in a single step [22].

During fibreization, molten glass is drawn through fine orifices to produce fibres with diameters typically ranging from 3 to 20 μm. The diameter of E-glass fibres, the most commonly used type, is generally between 8 and 15 μm, offering a balance between mechanical strength and ease of processing. Once drawn, the fibres are coated with a sizing agent to improve adhesion to resin matrices and protect against surface damage, before being wound onto spools for subsequent use [22], [24].

Among the various glass fibre types, E-glass remains the most prevalent due to its cost-effectiveness and balanced mechanical, thermal, and electrical properties, making it suitable for a wide range of structural and electrical applications [22], [24]. Other specialized glass fibres include S-glass, which exhibits significantly higher tensile strength and improved fatigue resistance compared to E-glass, making it more suitable for high-performance structural applications where superior mechanical performance is critical. AR-glass, which is alkali-resistant, and ECR-glass, recognized for its enhanced corrosion resistance, are also employed in more chemically aggressive environments [22].

2.1.1.3 Organic Fibres

Organic fibres, composed of carbon-based materials, are employed as reinforcements in composite systems to improve mechanical properties while maintaining a relatively low weight. These fibres can be classified into two main categories: natural and synthetic [25].

Natural fibres are derived from plant, animal, or mineral origins and offer advantageous characteristics such as high specific strength and modulus, flexibility in processing, low density, affordability, and notable resistance to corrosion and fatigue [26]. Despite these benefits, natural fibres also present certain limitations, including significant moisture absorption, pronounced anisotropy, reduced compatibility with conventional resin systems, and a lower degree of homogeneity compared to glass and carbon fibres [27]. Consequently, these limitations can restrict their applicability in high-performance structural applications.

Synthetic organic fibres are produced through chemical processes, typically involving polymerization of petrochemical-based monomers. These are engineered for exceptional tensile strength, impact resistance, and thermal stability. Organic fibres can be broadly classified into two main categories: aramid fibres and UHMWPE.

Aramid Fibres

Aramid fibres are widely recognized for their exceptional mechanical properties, positioning them as a critical component in synthetic fibre composites. They are a type of aromatic polyamid, and common examples include Kevlar, Nomex and Twaron. Originally developed for use as insulation in advanced composites, aramid offers a unique combination of tensile strength, toughness, and thermal stability [28]. Compared to steel and glass fibres, aramid provides a superior strength-to-weight ratio, making it highly effective in weight-sensitive applications [29].

Key properties of aramid include resistance to abrasion, cutting, and most chemical solvents. However, it is susceptible to degradation when exposed to specific acids, bases, chlorine, and ultraviolet radiation. Additionally, under high temperatures and humidity, hydrolytic degradation may occur, potentially compromising its structural integrity [30], [31].

A notable variant, para-aramid, demonstrates a tensile strength of approximately 3620 MPa and a density of 1.44 g/cm^3. It effectively absorbs impact energy while maintaining its structure under thermal stress, as it lacks a defined melting point [32]. While aramid refers broadly to aromatic polyamides, para-aramid is distinguished by its molecular structure, where the amide linkages occur in the para position of the aromatic ring. This configuration results in greater chain alignment, leading to superior tensile strength and stiffness compared to generic aramids. Despite its strengths, aramid is more prone to moisture absorption than glass or graphite fibres, necessitating the use of moisture-resistant matrices. Furthermore, its compressive strength is relatively limited, constraining its use in load-bearing applications [33].

Aramid fibres are produced through a solution polycondensation process involving diamines and diacid halides at low temperatures. The resulting polymer is spun from a liquid crystalline solution, typically in concentrated sulfuric acid, forming highly ordered, rod-like polymer chains that align along the fibre axis during extrusion through a spinneret. This alignment imparts the characteristic fibrillar structure and high strength of aramid fibres, such as Kevlar [34].

UHMWPE

UHMWPE is a thermoplastic polymer consisting of exceptionally long, linear molecular chains made up of over 100000 monomer units. These chains are simple and rigid, often described as "rod-like" due to their elongated structure. The production of UHMWPE involves the polymerization of ethylene using a metallocene catalyst, resulting in the formation of a high molecular mass material. During the fibre drawing process, the alignment of these chains induces a high level of crystallinity, typically exceeding 80% [12].

In UHMWPE, interchain interactions rely primarily on dispersion forces, as the nonpolar structure lacks strong bonding mechanisms. However, the extended chain length compensates for this by allowing effective load distribution through shear forces, contributing to the overall strength of the fibres [12].

Since the late 1990s, commercially available UHMWPE fibres such as Dyneema and Spectra have seen substantial advancements. Enhanced processing techniques have enabled the production of finer fibres, resulting in improved tensile strength and elastic modulus, both of which are closely linked to fibre diameter. Despite these improvements, UHMWPE is constrained by a relatively low melting temperature (145–155ºC) and an operational temperature range of 60–80ºC. As a thermoplastic, it will melt and decompose under flame exposure, releasing combustible gases, a crucial limitation in high-temperature environments. Additionally, the rising market demand for UHMWPE fabrics with superior ballistic properties has driven up costs [12].

The production of UHMWPE fibres primarily involves two techniques: melt-spinning and solution (gel)-spinning, each employing distinct mechanisms to align polymer chains for optimal mechanical properties [35].

Melt-spinning begins with the extrusion of polyethylene with a relatively low molecular weight (approximately 100,000 g/mol), followed by hot-drawing to orient the polymer chains. Despite achieving tensile strengths up to 1.5 GPa and moduli of around 70 GPa, the mechanical properties are constrained by limited interchain interactions, predominantly governed by weak Van der Waals forces [35].

A more effective approach is solution (gel)-spinning, utilizing UHMWPE with molecular weights exceeding 3 million g/mol. In this process, the polymer is dissolved at low concentrations in a solvent, forming a viscous gel that can be spun and subsequently drawn under elevated temperatures. During drawing, the solvent acts as a plasticizer, facilitating the alignment of polymer chains. Upon solvent removal, the as-spun fibres retain a state that permits further extension and orientation, allowing for tensile strengths above 3 GPa and elastic moduli surpassing 100 GPa [35].

The superior mechanical performance of UHMWPE fibres is attributed to the extended molecular chain structure and the reduction of entanglements, enabling more effective load transfer and enhancing the overall tensile and compressive properties of the fibres [35].

2.1.2 Matrices

The matrix serves as the continuous phase in a composite material, binding the reinforcing fibres or particles together, distributing loads, and protecting the reinforcement from environmental and mechanical damage [36]. Its selection is governed by factors such as resistance to atmospheric agents, operating environment, mechanical properties, and cost. The matrix not only transfers loads to the reinforcement but also shields it from chemical attack and adverse environmental conditions [19]. Furthermore, it can act as a barrier to crack propagation, thereby improving the structural integrity and durability of the composite [18].

Matrices used in advanced composites can be broadly classified into three main categories: polymeric matrices, metal matrices, and ceramic matrices. Polymeric matrices are the most widely employed, particularly in aerospace and automotive applications, due to their ease of processing, low density, and good mechanical performance [2]. Metal matrices are selected for applications demanding high strength, thermal stability, and durability in aggressive environments [36]. Ceramic matrices are favoured where extreme temperature resistance and corrosion protection are critical [36], [37]. The following subsections describe each category in detail.

2.1.2.1 Polymeric Matrices

Polymeric matrices for advanced composites are broadly categorised into thermosets and thermoplastics, each possessing distinct molecular structures and processing characteristics that influence their behaviour and suitability for structural applications [2].

Thermosetting matrices are initially composed of low-molecular-weight monomers with relatively low viscosity, enabling them to flow easily into moulds or fibre reinforcements. During the curing process, these monomers undergo a sequence of chemical reactions that progressively form a rigid, 3D cross-linked network. As curing advances, the available free volume within the molecular arrangement decreases, leading to reduced molecular mobility and a substantial increase in viscosity. Once the resin gels and transitions into a rubbery solid, it becomes infusible and insoluble, permanently locking the polymer network in place. Subsequent heating after complete curing does not cause remelting but rather results in thermal degradation. Consequently, thermosets generally require longer processing times due to their thermally driven curing process, which involves successive stages of heating, gelation, and post-curing [17], [38].

Thermosetting matrices include polyesters, vinyl esters, epoxies, bismaleimides, cyanate esters, polyimides, and phenolics. These materials are valued for their high thermal stability, dimensional integrity, and mechanical strength, making them particularly suitable for applications requiring sustained structural performance under elevated temperatures and high mechanical loads.

In contrast, thermoplastic matrices consist of high-molecular-weight polymers that do not undergo chemical cross-linking upon heating. Instead, they become liquid or pasty when heated above their glass transition temperature, allowing them to be moulded and consolidated. Upon cooling, they solidify and retain the desired shape. This reversibility not only enables faster processing but also facilitates recycling and reshaping in subsequent manufacturing cycles. However, due to their high viscosity and melting points, thermoplastics generally require higher temperatures and pressures for effective processing compared with thermosets [38], [39].

Typical thermoplastic matrices used in advanced composites include polyether ether ketone (PEEK), polyphenylene sulfide (PPS), and polyether ketone ketone (PEKK). These materials offer excellent toughness and impact resistance, together with the capability to be reheated and reshaped. However, they often exhibit lower thermal stability than thermosetting resins [2], [39].

2.1.2.2 Metal Matrices

Metal matrices are employed in composite materials to provide enhanced mechanical strength, thermal stability, and resistance to harsh environments. Due to their inherent stiffness and higher yield strength, metals are ideal for applications that require high transverse strength and compressive resistance, particularly in sectors such as aerospace and automotive engineering. Additionally, metals can undergo thermal and mechanical treatments to further enhance their structural properties, a flexibility not present in other types of matrix materials [36].

However, the use of metals as matrices presents certain challenges. They are generally denser and have higher melting points, necessitating elevated processing temperatures and complex manufacturing processes. Furthermore, metals are susceptible to corrosion, especially at the fibre-matrix interface, potentially compromising the integrity of the composite over time [17], [36].

Among metal matrices, aluminium and its alloys are the most widely utilized, offering a balance of low density, good corrosion resistance, and reasonable mechanical properties. Pure aluminium is commonly selected for its natural corrosion resistance, while specific alloys are tailored to achieve higher strength and improved thermal performance. Magnesium, although lighter than aluminium, is more prone to atmospheric corrosion, limiting its applications in aggressive environments. Beryllium is the lightest structural metal with a tensile modulus exceeding that of steel, but its extreme brittleness restricts its use in critical structural applications [2], [17].

Nickel and cobalt-based superalloys are also employed as matrix materials, particularly in high-temperature applications. However, their alloying elements can accelerate oxidation at elevated temperatures, leading to potential degradation at the fibre interface. The integration of reinforcements such as silicon carbide can further enhance the mechanical properties, increasing stiffness and wear resistance while reducing thermal expansion [2].

2.1.2.3 Ceramic Matrices

Ceramic matrices are composed of ceramic particulates, fibres, or whiskers embedded within a ceramic matrix material. These materials are characterized by strong ionic or covalent bonding, contributing to their high thermal stability, corrosion resistance, and compressive strength, making them ideal for applications in high-temperature and corrosive environments [36].

Ceramics are known for their high modulus, thermal shock resistance, hardness, and low density. However, they are also brittle and susceptible to crack propagation, resulting in low fracture toughness. To address this limitation, ceramic matrices are engineered to maintain structural integrity under extreme thermal and mechanical stress, ensuring reliable performance in demanding conditions [37].

Ceramic matrices are generally categorized into oxides and non-oxides. Oxide ceramics, such as alumina (Al_2O_3) and mullite ($Al_2O_3 - SiO_2$), are commonly used due to their excellent thermal and chemical stability, offering strong resistance to oxidation and corrosion at high temperatures. In contrast, non-oxide ceramics, including silicon carbide (SiC), silicon nitride (Si_3N_4) and aluminum nitride (AlN), are characterized by high modulus and thermal conductivity, making them suitable for applications that require exceptional thermal management and mechanical strength. Among these, SiC stands out for its thermal stability and compatibility with other ceramic phases, while Si_3N_4 is recognized for its high strength, and AlN is preferred for its superior thermal conductivity [2], [36].

2.1.3 Hybrid Composite Laminates

Polymer matrix composites are often manufactured by stacking multiple laminae to form a laminate. Each ply is typically thin relative to its in-plane dimensions and contains fibres oriented predominantly in one direction, resulting in anisotropic mechanical behavior [34]. To overcome this directional limitation and optimize the structural response under complex loading conditions, it is common practice to arrange plies in different orientations within the laminate. This approach allows for the tailoring of stiffness, strength, and failure characteristics to suit specific performance requirements. As illustrated in Figure 2.2, common stacking configurations include (a) unidirectional, (b) cross-ply, (c) angle-ply, and (d) quasi-isotropic layouts.

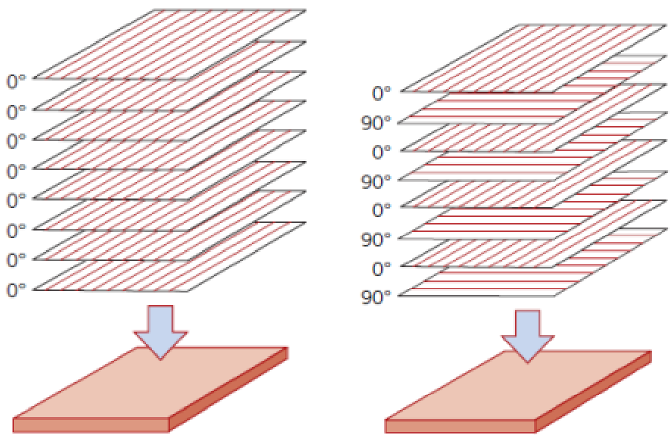

(a) (b)

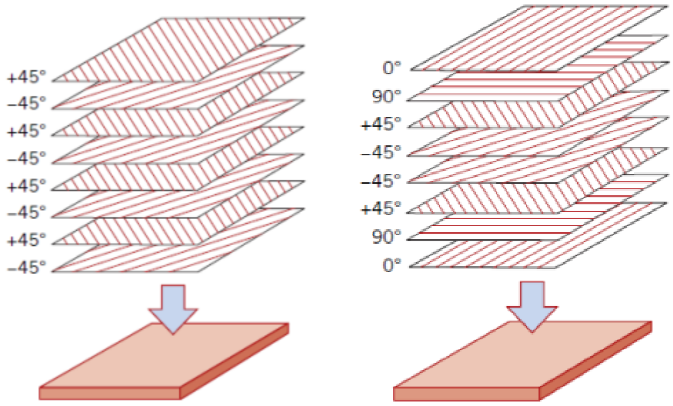

(c) (d)

Figure 2.2: Examples of laminate configurations: (a) Unidirectional, (b) Cross-ply, (c) Angle-ply, and (d) Quasi-isotropic (adapted from [40]).

In the field of ballistic protection, hybrid laminates, composed of two or more distinct fibre or material systems, offer an effective means of combining complementary mechanical characteristics within a single structure. These laminates are typically engineered to harness different mechanisms of energy absorption and failure. One material layer may act as a disrupter, initiating fragmentation or deceleration of the projectile, while a second layer functions primarily to absorb and dissipate the remaining kinetic energy. This sequential response forms the basis for many protective systems, including ceramic/metal and ceramic/composite configurations [41].

A widely adopted and well-studied example is the ceramic/UHMWPE laminate. In this system, the ceramic strike face serves as the initial barrier, fracturing and blunting the projectile while dispersing the impact energy over a larger area. The UHMWPE composite backing then mitigates the residual force through a combination of fibre stretching, interlaminar shear, and out-of-plane bulging. This layered synergy not only prevents complete perforation but also reduces the extent of backface deformation, which is critical in minimizing blunt trauma for the wearer [10].

Beyond their mechanical efficiency, hybrid laminates also present opportunities for cost optimization and improved material utilization. By incorporating more economical fibre systems alongside high-performance materials, it is possible to reduce overall material costs without significantly compromising performance. Additionally, beneficial interactions between constituent materials, such as improved crack deflection or delayed delamination, can enhance damage tolerance and fatigue life, making hybrid laminates well-suited for applications requiring repeated or multi-hit resistance [34].

2.1.4 Composites in Aircraft and Military Applications

The commercial and industrial applications of Fibre-Reinforced Polymer (FRP) composites are remarkably diverse, encompassing sectors such as automotive, construction, marine, and sports equipment. However, given the specific scope of this dissertation, particular emphasis will be placed on their use in aerospace structures and military systems, where the unique combination of high strength-to-weight ratio, durability, and design flexibility makes composite materials especially advantageous [2].

In recent decades, the aerospace sector has undergone a significant evolution in material selection, increasingly favouring FRPs. These advanced materials, as mentioned before, consist of high-strength fibres embedded within a matrix, typically polymeric, though ceramic and metallic matrices are also used depending on the application requirements [42].

A notable milestone in this transition was the implementation of boron fibre-reinforced epoxy skins in the horizontal stabilisers of the F-14 Tomcat in 1969, marking one of the earliest uses of FRPs in structural aircraft components [2]. Since then, the adoption of these materials has grown steadily, with recent trends showing nearly a 50% increase in composite material usage within the aerospace industry, reflecting a fundamental shift in structural design philosophy [42]. This growth is clearly illustrated in Figure 2.3, which highlights the expanding role of composites in modern aircraft structures.

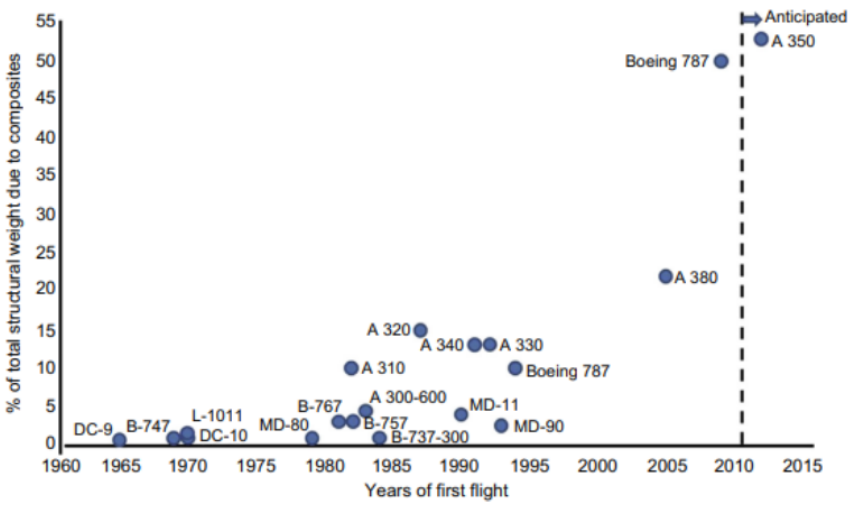

Figure 2.3: Increased growth of composite use in aircraft over the years (Adapted from [42]).

To demonstrate that composite materials are as reliable and effective as the traditional metals used in aircraft applications, a comprehensive certification process is essential. This process involves rigorous testing and adherence to established standards to ensure that composites meet the stringent requirements of the aerospace industry. Regulatory bodies such as the European Union Aviation Safety Agency (EASA) and the Federal Aviation Administration (FAA) have published extensive guidance for the certification of composite structures. EASA's Acceptable Means of Compliance (AMC) 20-29 and FAA's Advisory Circular AC 20-107B provide standardised frameworks for the design, manufacturing, maintenance, and continued airworthiness of composite components [43]. These documents have been instrumental in supporting the safe and systematic integration of composites in modern aircraft, ensuring performance reliability equivalent to, or surpassing, that of conventional metallic structures [44], [45].

A more detailed examination of the certification process for military aircraft will be conducted in the following subchapter (Section 2.2), with the objective of gaining a deeper understanding of the specific requirements and challenges involved.

One of the most prominent examples of composite integration is the Boeing 787 Dreamliner programme, initiated in 2003, which marked a significant leap in the application of CFRP. The 787 utilises approximately 50% CFRP by weight, extensively incorporated into the airframe, wings, and tail structures. This represents a substantial increase compared to earlier models, such as the Boeing 767, where CFRP was limited to around 3% of the structural mass. In parallel, aluminium usage in the 787 decreased from 77% to approximately 20%, leading to an overall weight reduction that contributed to fuel savings of 20–22% relative to the 767 [3]. The aircraft also introduced composite wings with raked wingtips, a design that improves lift-to-drag ratio and enhances both climb performance and take-off efficiency. Such advanced wing geometries, featuring double-curvature profiles and variable camber, are only feasible with composite materials [4].

In response to Boeing's innovation, Airbus launched the A350 XWB programme in 2005, similarly emphasizing the use of CFRPs, which account for around 53% of its structural mass. The extensive use of composites not only improved aerodynamic efficiency but also resulted in a 50% reduction in structural maintenance requirements, with extended airframe check intervals compared to previous generations [6]. Although the initial manufacturing costs of CFRP components are higher than those of metallic counterparts, composites offer significant long-term savings due to their inherent resistance to fatigue [5], [6]. Figure 2.4 illustrate the material composition by weight of the Boeing 787 Dreamliner and the Airbus A350 XWB, respectively, highlighting the significant adoption of composite materials in their structural designs.

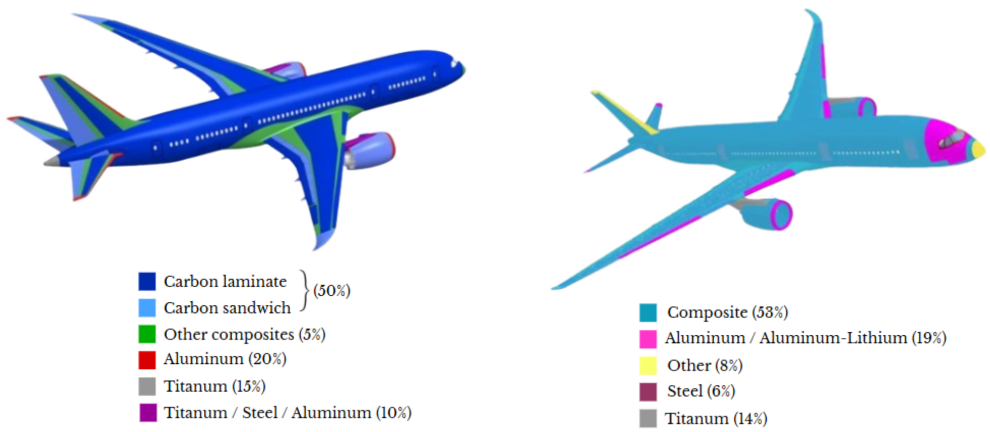

(a) (b)

Figure 2.4: Material distribution by weight: (a) Boeing 787 Dreamliner (Adapted from [46]), and (b) Airbus A350 XWB (Adapted from [47]).

In military aviation, the adoption of composite materials has been driven primarily by the need for enhanced operational performance, stealth capabilities, and increased durability. The Lockheed Martin F-35 Lightning II exemplifies this trend, featuring a composite airframe that contributes to its low observability and maneuverability. Approximately 35% of the F-35's airframe is constructed from composite materials, significantly aiding in radar cross-section reduction and payload optimization [48]. Another prominent example is the Northrop Grumman B-21 Raider, the US Air Force's next-generation stealth bomber, which extensively incorporates composites to achieve superior stealth and long-range performance [49].

2.2 Military Aircraft Certification

Aviation systems, whether civil or military, are designed to fulfil specific operational objectives in a resource-efficient manner. However, their fundamental missions, operational constraints, and performance expectations diverge significantly. Civil aviation is inherently commercial, structured around revenue generation and guided by market-driven investments, with an overarching emphasis on consistent safety, efficiency, and service reliability. In contrast, military aviation serves strategic national interests, executing roles such as search and rescue, reconnaissance, air defence, and logistical support, often within volatile or hostile environments. These operations are state-funded and prioritise mission success over cost-efficiency. As a result, the concept of a mission differs substantially between the two domains. In civil aviation, a mission generally refers to the act of transporting passengers or cargo safely and efficiently from one location to another. In contrast, military aviation defines its missions in terms of accomplishing specific operational goals, which may involve complex, high-risk scenarios that extend beyond transportation, such as surveillance, combat engagement, or logistical support in conflict zones [7], [8].

Furthermore, differences extend to fleet composition and operational scale. Civil fleets tend to be large and homogeneous, optimised for standardised operations across global routes. Military fleets, by contrast, are smaller, diverse in aircraft types, and tailored to specific operational requirements, often produced in limited quantities. These variations also impact safety thresholds. Civil aviation adheres to strict and uniform safety standards, while military aviation may accept elevated operational risks, particularly in wartime scenarios where airworthiness limitations are contextually tolerated. As such, while both sectors regard safety as central to operational integrity, the acceptable level of risk and the regulatory frameworks governing their airworthiness are inherently shaped by their differing purposes and environments [7].

In the following sections, both the European and US military certification frameworks will be examined in detail, focusing on their regulatory structures, certification processes, and key documentation, with particular attention to aspects relevant to aircraft survivability and protection systems.

2.2.1 European Military Certification Framework

Unlike civil aviation, which is governed by a centralised regulatory body, the EASA, military aviation operates without a universally binding international framework. Each nation maintains its own Military Aviation Authority (MAA), tasked with developing and applying national airworthiness requirements. This decentralised model has led to considerable variability in certification approaches, making cross-border collaboration particularly complex [50].

In response to this fragmentation, the European Defence Agency (EDA) was established in 2004 with a mandate to enhance defence cooperation within the European Union (EU). One of its foundational aims was to promote a more integrated and competitive European Defence Equipment Market, while also reinforcing the continent's Defence Technological and Industrial Base. The EDA has actively encouraged joint capability development and greater harmonisation across Member States, particularly in technical domains such as certification. Recognising the maturity and efficiency of civil aviation standards, the EDA identified the EASA framework as a viable foundation for military application, leading to a strategic decision to transpose its principles to the defence sector [50], [51].

In 2008, the EDA launched the Military Airworthiness Authorities (MAWA) Forum, bringing together representatives from national MAAs. The Forum's objective was to establish a harmonised military airworthiness system across Europe through common requirements, procedures, and mutual recognition. A structured roadmap was created, supported by ministerial consensus, to develop a unified regulatory framework, shared certification processes, common design codes and organisational approvals, and long-term mechanisms for joint oversight. This initiative laid the foundation for the European Military Airworthiness Requirements (EMARs) [51].

The EMARs are a family of military airworthiness regulations designed to be implemented by each national MAA, ensuring that each country retains sovereignty while contributing to an interoperable and recognisable certification system. These regulations mirror the EASA regulatory model but are adapted to accommodate military-specific conditions. Among the full body of EMARs, several are particularly relevant to the subject of this dissertation due to their direct application to the design, maintenance, training, and continuing airworthiness of military aircraft and associated organisations [51], [52].

The most relevant EMARs for the context of this work are as follows:

- EMAR 1: Defines the general regulatory framework for military airworthiness, specifying responsibilities for initial certification and continuing airworthiness.

- EMAR 21: Governs the certification of military aircraft, parts, and appliances, and sets out requirements for Design and Production Organisation Approvals.

- EMAR 66: Specifies the requirements for the qualification and licensing of certifying staff responsible for maintenance activities on military aircraft, ensuring competence through knowledge, skills, and experience standards.
- EMAR 145: Establishes standards for military maintenance organisations, particularly in relation to procedures, qualified personnel, and quality management.
- EMAR 147: Regulates training organisations responsible for the certification and qualification of military maintenance personnel.
- EMAR M: Describes the Continuing Airworthiness Management framework, including maintenance scheduling, compliance tracking, and airworthiness reviews.

In parallel with the EMARs, the MAWA Forum has developed a complementary set of documents known as European Military Airworthiness Documents (EMADs). These documents serve to facilitate the implementation, interpretation, and mutual recognition of EMARs-based frameworks across Member States. For the purposes of this thesis, particularly in the context of certification, organisational approval, and test operations, some EMADs are especially pertinent and are briefly outlined below [52]–[54].

- EMAD-R (Recognition): Defines a formal process for mutual recognition of certificates and approvals issued under the EMARs between different MAAs.
- EMAD-A (Arrangements): Outlines the administrative agreements required to implement EMARs in a harmonised and coordinated manner across participating nations.
- EMAD-G (Guidance): Provides technical interpretation and practical guidance to ensure consistent application of EMARs provisions.
- EMAD 1 (Military Airworthiness Policy): Sets out the strategic objectives and guiding principles for a coherent and cooperative European military airworthiness environment.
- EMAD 20 (European Military Design Organisation Approval (EMDOA)): Specifies requirements for the multinational approval and mutual recognition of military design organisations.
- Military Flight Test Permit (MFTP): Establishes the conditions under which experimental or prototype military aircraft may be operated for testing purposes prior to full certification.

The certification of military aircraft within the European context is conducted through a structured and methodical process, drawing from civil aviation principles while being carefully adapted to meet the unique operational and security demands of defence applications [55].

This process begins with the approval of the Design Organisation (DOA), which grants an entity the authority to undertake the design and development of military aircraft and associated products. To receive such approval, the organisation must demonstrate that it possesses the technical capability, internal procedures, and safety assurance systems necessary to support airworthiness. Only organisations with a recognised DOA are permitted to engage in the certification of military aerospace systems, in accordance with established regulatory frameworks [55], [56].

Once design authority is in place, the aircraft must fulfil the criteria for both initial and continuing airworthiness. Initial airworthiness relates to the verification that the design satisfies all applicable military standards, particularly in areas such as structural safety, system reliability, and overall compliance with airworthiness codes. In contrast, continuing airworthiness encompasses the maintenance of that compliance throughout the service life of the aircraft. This includes scheduled inspections, configuration control, defect monitoring, and adherence to maintenance requirements, ensuring the aircraft remains safe and effective in operation [56], [57].

Upon satisfactory demonstration of initial airworthiness, the relevant MAA may issue a Military Type Certificate (MTC). The MTC serves as formal confirmation that the aircraft design meets all mandatory military airworthiness criteria and is suitable for its intended operational role. The issuance of the MTC is a critical milestone, enabling the aircraft to progress towards operational deployment [56], [58].

Following this, the Release to Service (RTS) is issued at the national level by the competent authority. Unlike the MTC, which certifies the design, the RTS takes into account the specific configuration, current maintenance state, and any operational restrictions associated with a particular aircraft or fleet. The RTS is essential to bridge the regulatory oversight with the operational responsibilities of the military command, ensuring that aircraft are both technically certified and operationally fit for mission execution [55].

2.2.2 United States Military Certification Framework

In contrast to civil aviation, which in the US is regulated centrally by the FAA, as mentioned before, military aviation operates under a separate system of governance. US military aircraft are designated as public aircraft within national borders and state aircraft when operating internationally, which exempts them from FAA airworthiness procedures. Instead, the Department of Defense (DoD) serves as the overarching authority for military airworthiness, but delegates implementation responsibilities to the individual service branches. Each service namely, the Air Force, Navy, and Army, functions as an autonomous Military Airworthiness Authority, developing and enforcing its own airworthiness policy under the legal authority of its respective Secretary [59], [60]. This decentralised model allows each branch to tailor certification frameworks to its operational needs, but it also introduces regulatory divergence across the services [61].

To address the resulting fragmentation, the DoD has progressively developed a unifying policy structure intended to improve standardisation and enable mutual recognition across service branches. A key component of this initiative is the issuance of the DoD Joint Airworthiness Policy, which formalises authority derivation and outlines the responsibilities of each airworthiness organisation. The policy permits branches to recognise each other's certifications when the aircraft share the same role, configuration, and environment [59], [60]. This mechanism provides an operational bridge across services and improves the coherence of the certification landscape.

The cornerstone of the US military's harmonisation effort is the adoption of a shared certification standard, embodied in the document MIL-HDBK-516. First published in 2002 and now in its C revision, MIL-HDBK-516C defines a set of comprehensive and performance-based airworthiness certification criteria applicable across all services [59]. The handbook covers essential domains including structural integrity, system safety, crashworthiness, human-machine integration and cybersecurity. It does not mandate specific design solutions, but rather sets out objectives that allow for engineering flexibility while ensuring operational safety and compliance. This adaptability makes it particularly suitable for the diverse operational profiles and technical architectures encountered in military aviation [62].

Each service implements the framework set out in MIL-HDBK-516C according to its organisational structure and mission profile. The United States Air Force (USAF) manages airworthiness certification through the Air Force Life Cycle Management Center (AFLCMC), where the Director of Engineering serves as the Technical Airworthiness Authority (TAA). This authority is responsible for defining certification standards, issuing compliance findings, and authorising flight via MTCs. The USAF codifies its policy in AFPD 62-6 and implements it via Air Force Instructions, although practical disconnects between policy and execution have been noted. Operational and maintenance oversight responsibilities are devolved to the unit level, with compliance enforced internally rather than through independent evaluation, potentially weakening assurance in these areas [61].

Within the US Navy and Marine Corps, the Chief of Naval Operations designates the Commander of Naval Air Systems Command (NAVAIR) as the lead airworthiness authority. This responsibility is operationalised through the Airworthiness Office, which issues flight clearances as the Navy's formal airworthiness approval. The process is structured around a comprehensive systems engineering review and is tightly linked to the documentation outlined in the Naval Aviation Maintenance Program (NAMP). While the Navy's regulatory model blends policy, process, and oversight into a single framework, this integrated approach can obscure the delineation between design, operational, and maintenance responsibilities [61].

The US Army regulates airworthiness through Army Regulation 70-62. The Deputy Chief of Staff establishes policy, while certification authority lies with the Commanding

General of the Army Aviation and Missile Command. The Army's certification methodology consists of three pillars: assessment of design against applicable standards, definition of safe operating limits, and continued compliance through routine inspections and quality-controlled maintenance procedures. The Army's regulatory structure is less centralised, with operational airworthiness and maintenance governed by distinct and independently enforced policy documents. Maintenance assurance is validated through Aviation Resource Management Survey (ARMS) inspections and relies heavily on embedded quality management systems [61].

In all services, the certification of military aircraft is conducted through a structured process that begins with the establishment of design authority. Organisations engaged in aircraft development must demonstrate technical capability, adherence to engineering standards, and internal safety oversight mechanisms in order to be recognised as competent for certification activities. The certification process typically uses MIL-HDBK-516C as a baseline reference, as it defines the comprehensive airworthiness criteria applicable to both manned and unmanned systems across their entire lifecycle. This handbook provides a standardised, tailorable set of criteria that supports consistent evaluation of design safety, structural integrity, and system reliability. Based on this framework, the certification process addresses both initial and continuing airworthiness. Initial airworthiness confirms that a design meets all applicable technical and operational safety requirements, while continuing airworthiness ensures that compliance is maintained throughout the aircraft's service life through proper maintenance, defect tracking, and configuration control [63].

Upon successful verification of the airworthiness requirements, the responsible Military Airworthiness Authority issues a formal type approval. In the USAF, this takes the form of a MTC, while in the Navy and Army, it is a flight clearance or airworthiness qualification. These approvals are necessary prerequisites for entry into service but are not, by themselves, sufficient. An additional step, typically in the form of an operational release or flight readiness review, is required to verify that the specific aircraft or fleet is in an appropriate state of configuration and maintenance, and that it is safe for its intended operational use [64]. This final authorisation serves as the bridge between regulatory certification and mission deployment, ensuring the aircraft is not only technically sound but also tactically ready [61].

2.2.3 Ballistic Testing Standards used by the US Military: The Case of MIL-STD-662F

Beyond airworthiness certification, the survivability of military aircraft in hostile environments necessitates stringent ballistic resistance testing. This is particularly critical for rotorcraft and low-flying fixed-wing platforms that are often exposed to small-arms fire and fragmentation threats during tactical operations. To ensure adequate protection, the US DoD has established a comprehensive suite of ballistic testing standards tailored to assess the performance of protective materials under impact conditions representative of combat scenarios. These standards are material-specific and are designed to evaluate a wide spectrum of solutions, ranging from metallic armors and ceramics to polymer-based composites and transparent materials employed in canopy systems and sensor housings [65], [66].

Each standard outlines a unique methodology, including projectile specifications, test velocities, and failure criteria. For instance, MIL-STD-376 defines test methods for evaluating ceramic armour, while MIL-DTL-12560 and MIL-DTL-46100 are used for homogeneous and high-hardness steel plates respectively. Transparent armour systems, such as ballistic-grade glass and polycarbonate laminates, are assessed under TACOM ATPD 2352R. These procedures enable developers and certifying bodies to characterise and compare materials based on their ability to absorb kinetic energy, resist penetration, and minimise behind-armour effects [66]. Table 2.1 provides an overview of key ballistic testing standards issued by the US military.

Table 2.1: Main ballistic testing standards used by the US military [66].

Standard	**Description**
MIL-STD-662F	V_{50} Ballistic Test for Armor
MIL-STD-376	Ceramic Armor Testing
MIL-STD-3038	Test Methods for Ballistic Defeat Materials
MIL-DTL-45225	Aluminum Alloy Armor, Forged
MIL-DTL-32332 (MR)	Armor Plate, Steel, Wrought, Ultra-High-Hardness
MIL-DTL-12560 (MR)	Armor Plate, Steel, Wrought, Homogeneous
MIL-A-46099C	Armor Plate, Steel, Roll-Bonded, Dual Hardness
MIL-DTL-46100	Armor Plate, Steel, Wrought, High-Hardness
MIL-PRF-46103	Armor: Lightweight, Composite
MIL-DTL-46077	Armor Plate, Titanium Alloy, Weldable
TACOM ATPD 2352R	Purchase Description Transparent Armor
UL 752	Underwriters Laboratory Ballistic Standards (civil-military interface)

Among the standards developed to evaluate the ballistic performance of protective materials, MIL-STD-662F stands out for its rigorous methodology and relevance to modern composite armor systems subjected to high-velocity impacts. This standard defines a procedure for determining the V_{50} ballistic limit, which corresponds to the projectile velocity at which there is a 50% probability of complete penetration through the tested material [65]. Unlike simple pass/fail approaches, this method provides a statistically meaningful threshold that allows for consistent comparisons between different material systems.

To obtain the V_{50} value, a series of controlled tests is performed in which projectiles are launched at varying velocities. The outcome of each shot, classified as either complete or partial penetration, is recorded, and the V_{50} is calculated as the average velocity at which the probability of full perforation is exactly 50% [65]. This approach reduces sensitivity to anomalous results and enhances the reliability of the data.

In addition, the method addresses the inherent variability in material behavior that may arise from factors such as fibre orientation, bonding inconsistencies, or microstructural defects. By focusing on the transitional velocity range where these effects tend to manifest, the V_{50} criterion supports a more refined assessment of impact resistance. It has therefore become an essential tool in the evaluation of emerging protective materials, offering valuable insight for benchmarking, design validation, and early-stage development [65].

The structure of the MIL-STD-662F document reflects its systematic and comprehensive nature. It is organized into six main chapters, each contributing to a unified framework for conducting V_{50} ballistic testing. Table 2.2 provides a concise summary of these chapters, along with an overview of Table I from the standard, which outlines reference velocities for different projectile types.

Table 2.2: Summary of the six main chapters and annexed content of MIL-STD-662F [65].

Chapter / Element	**Description**
1. Scope	States the purpose, application, and limitations of the V_{50} ballistic test method.
2. Applicable Documents	Lists supporting military standards, handbooks, and referenced publications.
3. Definitions	Provides detailed terminology used throughout, including Complete Penetration (CP), Partial Penetration (PP), V_{50}, and related terms.
4. General Requirements	Specifies equipment, projectiles, mounting systems, and velocity measurement tools.
5. Detailed Requirements	Outlines the ballistic test procedure, V_{50} calculation, acceptance criteria, and reporting.
6. Notes	Offers administrative guidance, intended use, and record of document revisions.
Table I	Provides reference projectile velocity values to guide test relevance and consistency.

For the sake of completeness, the first chapter, Scope, defines the standard's purpose, areas of application, and limitations, focusing on the goal of establishing a repeatable statistical method for evaluating armor performance. The second chapter, Applicable Documents, compiles other military specifications, standards, and handbooks that support or complement the procedures outlined. The third chapter, Definitions, is particularly extensive, clarifying all relevant terminology used throughout the text, including key terms such as V_{50} ballistic limit, CP, PP, striking velocity, and witness plate. The fourth chapter, General Requirements, outlines the essential technical specifications for the test setup, including the projectile, firing system, velocity measurement equipment, propellant characteristics, mounting fixtures, and test sample parameters. Chapter five, Detailed Requirements, constitutes the core procedural content of the document. It includes comprehensive instructions on test conditions, equipment setup, execution of ballistic testing, data recording, calculation of the V_{50} value, acceptance criteria, retesting procedures, reporting format, and classification guidelines. Finally, chapter six, Notes, offers administrative information such as keyword indexing, intended application contexts, and a summary of updates from previous revisions. Complementing these chapters, Table I provides standardized reference velocities for various projectile types, ensuring consistency with recognized threat models and impact scenarios [65].

In addition, Figure 2.5 presents a simplified schematic of the experimental setup used in the V_{50} ballistic test. It shows the positioning of the projectile, armor, and witness plate, and illustrates how penetration events are classified. In a PP, the projectile does not reach the witness plate, while in a CP, it fully perforates the armor and impacts the witness plate. This distinction is essential for determining the V_{50} value, which is based on the statistical analysis of multiple CP and PP outcomes.

Although the present work did not aim to determine a formal V_{50} value, the selected impact velocities of 400 m/s and 600 m/s fall within the range prescribed by military standards for such testing (Section 2.2.2). Referring to the PP/CP framework is therefore relevant, as it provides the context within which the ballistic performance of the simulated configurations can be interpreted.

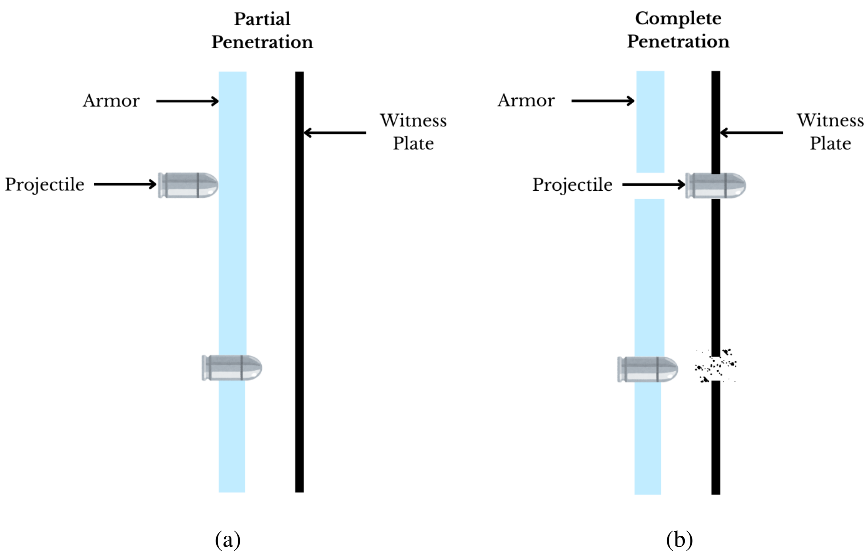

Figure 2.5: Schematic representation of projectile impact outcomes: (a) Partial penetration, and (b) Complete penetration.

2.3 Ballistic Protection

Ballistic protection refers to systems designed to resist or absorb the energy of high-speed projectiles. These systems include personal equipment such as vests, helmets, bomb blankets, as well as rigid structures like vehicle panels and protective shields. Depending on the type of threat, such as knives, handguns, or rifle bullets, materials and configurations are selected to ensure effective protection [67].

Ballistic systems are generally classified as flexible or rigid. Flexible systems are wearable and made from high-performance fibres arranged in woven, knitted, or nonwoven fabrics. Rigid systems often combine ceramic plates, such as boron nitride or tungsten carbide, with fibre-reinforced textiles like Kevlar, Twaron, or UHMWPE materials such as Dyneema and Spectra. These hybrid systems are designed so that the rigid plates spread the impact force, while the textile layers deform the projectile and absorb the remaining energy. In both cases, the goal is to absorb and dissipate kinetic energy. In soft armor, this is achieved through fibre stretching and rupture, while hard armor uses inserts to prevent penetration and blunt the bullet. The choice of material depends largely on projectile speed, which can range from around 400 m/s for handguns to 800 m/s for rifles [68]. In the present work, impact velocities of 400 m/s and 600 m/s were selected, as they fall within this interval and represent two distinct points of the ballistic spectrum: the lower bound associated with handgun-level threats and the intermediate-to-high regime relevant to rifle fire. This ensures that the numerical analyses not only replicate realistic threat conditions but also remain consistent with the certification ranges prescribed in military testing standards as mentioned in Section 2.2.2.

In addition to personal protection, ballistic resistance is essential in the design of military and structural components that are exposed to high-velocity impacts. These include aircraft, land vehicles, and infrastructure. Impacts of this nature can result in penetration or fragmentation, requiring materials capable of withstanding extreme loading conditions [69].

2.3.1 Hybrid Laminates for Ballistic Applications

Hybrid laminates have become a key focus in the development of lightweight, high-performance armour systems. These composites are formed by combining different types of reinforcing fibres to optimise protection, energy absorption, and structural integrity. The motivation behind hybridisation lies in the ability to exploit distinct material properties in a layered configuration, enabling a more effective response to ballistic threats [70].

Early hybrid systems often incorporated aramid fibres, such as Kevlar, due to their toughness and thermal stability. When combined with brittle but hard ceramics or stiff carbon fabrics, aramids improved energy dissipation and reduced damage propagation in multilayer configurations [71]. Glass fibres have also been used in hybrid panels as a cost-effective alternative, although their lower energy absorption compared to aramids and polyethylenes has limited their use in high-threat scenarios [70].

In recent years, attention has shifted toward UHMWPE, a material known for its high strength-to-weight ratio, low density, and superior ballistic resistance. UHMWPE fibres behave viscoelastically and can undergo significant deformation before failure, which makes them particularly effective in absorbing and dispersing kinetic energy from projectiles. Their role in hybrid laminates is often as backing layers, working in tandem with harder strike-face materials like carbon or ceramic to blunt, break, and decelerate the incoming projectile [72].

Recent experimental findings show that the ratio and sequencing of hybrid materials significantly affect performance. A study using carbon/UHMWPE laminates showed that increasing the proportion of UHMWPE leads to improved energy absorption and reduced backface deformation. A configuration with 75% UHMWPE and 25% carbon, for instance, successfully stopped 7.62 mm projectiles while achieving lower bulge height and slower deformation rate compared to pure UHMWPE or carbon laminates [72].

The structure and orientation of UHMWPE layers also have a substantial impact on ballistic performance. A study comparing woven and unidirectional (UD) UHMWPE fabrics in hybrid laminates found that stacking sequence plays a critical role. Panels configured with woven layers at the front and UD layers at the rear demonstrated superior performance by minimizing backface deformation and maximizing energy absorption. Both experimental results and finite element simulations identified an optimal hybrid ratio consisting of 25% woven and 75% UD UHMWPE [73].

The literature indicates that hybrid laminates incorporating UHMWPE have been widely investigated for their performance in ballistic applications. Their modular design, low weight, and energy dissipation characteristics have been studied as key factors for use in military systems, particularly in scenarios where both protection and mobility are important [72], [73].

2.3.2 Ballistic Protection Development and Practical Examples

The earliest approaches to ballistic protection were driven almost entirely by trial-and-error experimentation. Designs were iteratively tested and modified until they achieved the required performance, a process that was both time-consuming and costly due to the expense of advanced materials and full-scale ballistic trials. The introduction of computational modelling, particularly the Finite Element Method (FEM), transformed this process by allowing engineers to simulate impact events using known material properties and defined loading conditions [74]. Modern development strategies now combine virtual simulations with physical testing: simulations are used to refine designs and reduce the number of prototypes, while targeted experiments remain indispensable for validating and calibrating the numerical models. This integrated approach has significantly lowered development costs and accelerated innovation, with widely used FEM platforms including, for example, Abaqus, CATIA V5 and Ansys [75].

In military aviation, the use of complete airframe armour is impractical due to the significant weight penalties and the detrimental effect on aircraft performance. Instead, protection is applied selectively through modular armour systems, designed to safeguard only the most vulnerable or mission-critical areas. Specialist manufacturers supply composite or hybrid panels tailored for installation in locations such as pilot and co-pilot seats, cargo doors, floors, loading ramps, and engine nacelle fairings, as depicted in Figure 2.6. The design of these systems is underpinned by advanced numerical modelling, most notably finite element analysis, supported by standardised ballistic testing to ensure compliance with military protection standards [76], [77].

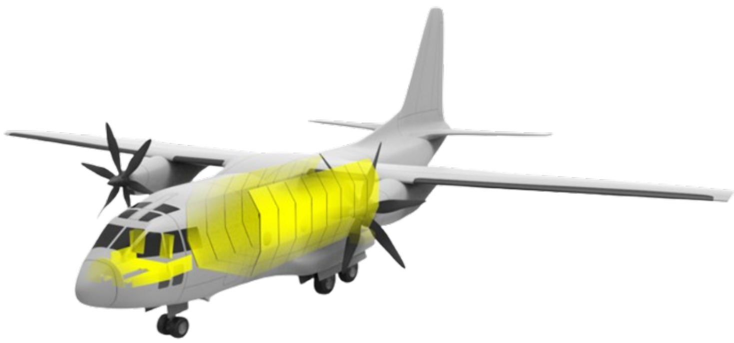

Figure 2.6: Ballistic panels used in military aviation [76].

A prominent operational example of such an approach is found in the A-10C Thunderbolt II, an aircraft conceived for close air support missions in high-threat environments. Introduced into service in 1977 with the aim of assisting ground forces, this aircraft features a ballistic protection box, nicknamed the “bathtub” due to its geometry, intended to shield the pilot as well as certain flight control systems. To this end, the structure was fabricated from 3.8 cm thick titanium plates, with a total weight of approximately 550 kg. Its cockpit enclosure protects the pilot and critical flight controls from ground fire, with the armour capable of withstanding direct hits from 23 mm armour-piercing projectiles and, in some cases, larger calibre rounds [78], [79]. Figure 2.7 presents the A-10C Thunderbolt II together with a close-up view of its titanium “bathtub” armour, highlighting its geometry and the way it encloses the pilot within the cockpit structure.

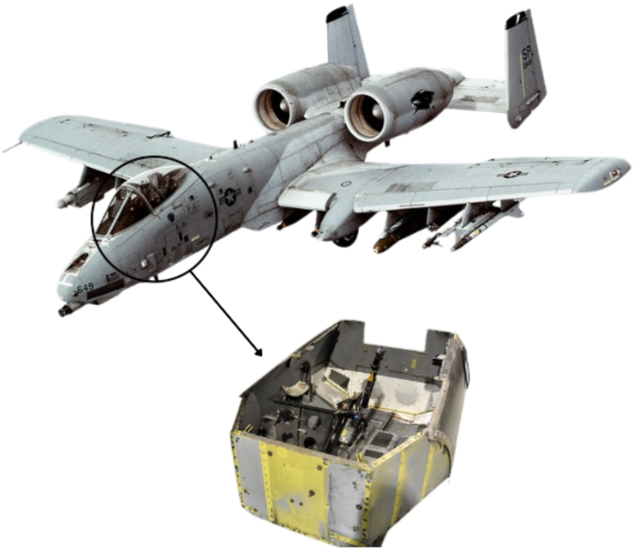

Figure 2.7: The A-10C Thunderbolt II with an inset close-up of the titanium "bathtub" cockpit armour (Adapted from [78]).

The armour's effectiveness has been proven in combat, most notably during Operation Iraqi Freedom, when an A-10 piloted by Captain Kim Campbell returned safely despite severe damage to its hydraulic systems, an outcome attributed to the resilience of the titanium enclosure and the aircraft's manual reversion capability [80]. Figure 2.8 shows the same aircraft after landing, with visible battle damage sustained during the mission. This integration of ballistic protection within the aircraft's structural design demonstrates how survivability requirements drive armour development in aviation.

Figure 2.8: The A-10C Thunderbolt II piloted by Captain Kim Campbell after returning from a mission during Operation Iraqi Freedom [80].

2.4 Impact Velocity Regimes

The classification of impact events into different velocity regimes is based on the manner in which energy is transferred from the projectile to the target, the mechanisms of energy dissipation, and the nature of damage produced in the target. As the projectile velocity changes, these factors can vary significantly, leading to distinct categories: low-velocity, intermediate-velocity, high-velocity (ballistic), and hypervelocity impacts [69].

From a structural dynamics perspective, an impact is considered low-velocity if the contact duration exceeds the fundamental period of vibration of the structure. In contrast, high-velocity or ballistic impacts are characterised by contact durations that are much shorter than the lowest natural period of the target. At the extreme end, hypervelocity impacts occur when the projectile moves at such high speeds that localised material behaviour resembles fluid flow [69]. Ballistic impacts typically involve low-mass projectiles at high velocities, often generated by a propelling device.

For practical engineering and testing purposes, impact velocities are often defined by approximate numerical ranges. Low-velocity impacts are generally below 10 m/s, intermediate-velocity impacts occur between 10 m/s and 50 m/s, high-velocity impacts range from 50 m/s to 1000 m/s, and hypervelocity impacts extend from 2000 m/s to 5000 m/s [81], [82]. The exact boundaries can depend on the stiffness of the target, its material properties, and the mass and stiffness of the projectile [82].

Low-velocity impacts are of particular concern for composite structures in service, as they can occur during operation or maintenance and may produce barely visible damage. Typical effects include matrix cracking, fibre breakage, and interlaminar delamination, particularly at ply interfaces with different fibre orientations, which can significantly reduce residual tensile and compressive strength. Such events are commonly assessed through standardised methods including pendulum devices (Charpy and Izod tests) and instrumented drop-weight towers, the latter allowing for a wider range of geometries and more representative component testing [81], [82].

Intermediate-velocity impacts produce more severe damage than low-velocity events, with greater potential for through-thickness cracking and fibre fracture. These impacts are less frequently addressed in certification standards but remain relevant for certain operational scenarios, such as heavy tool drops or runway debris strikes.

High-velocity or ballistic impacts are capable of causing immediate and catastrophic damage to aerospace and automotive structures. In aviation, examples include bird strikes, foreign object damage to turbine blades, and debris impacts on leading edges, canopies, and radomes. The relative speeds involved can be sufficiently high to cause instantaneous penetration or gross structural failure. Experimental investigation of such events is typically conducted using single-stage launchers, such as powder guns or gas guns, with the latter capable of achieving projectile velocities in the range of 2.0–2.2 km/s [82].

At the extreme, hypervelocity impacts are of primary concern in space applications, where micrometeoroid and orbital debris impacts can induce localised shock loading and cause severe structural erosion. In these conditions, both the projectile and the impacted material can exhibit fluid-like behaviour upon contact [69].

2.5 Dynamic Explicit Finite Element Modelling

As discussed previously in Section 2.3.2, the FEM has become an indispensable tool in the design and optimisation of ballistic protection systems, enabling engineers to replicate complex impact scenarios virtually before proceeding to experimental validation. While that earlier discussion outlined the general role of numerical modelling in reducing development costs and accelerating innovation, the present section focuses on the specific application of explicit dynamic finite element analysis. This approach is particularly suited to short-duration, high-speed events such as ballistic and blast loading, where large deformations, complex contact conditions, and progressive material failure occur. By examining the fundamentals of explicit time integration and its numerical implementation, the modelling strategies relevant to the simulations in this work can be clearly established.

The FEM has become one of the most important tools in engineering for the numerical simulation of complex systems. It allows the resolution of differential equations that govern physical phenomena through the discretisation of the geometry into finite elements. Within this framework, nodal values are approximated using shape functions, and the global behaviour is captured by assembling the contributions of all individual elements. This methodology is especially useful for solving problems involving complex geometries, heterogeneous materials, and non-trivial boundary conditions [83], [84].

In structural dynamics, FEM enables the simulation of time-dependent events, such as vibrations, impacts, and explosions. These simulations are driven by the governing equation of motion,

$$M\ddot{u} + C\dot{u} + Ku = f, \tag{2.1}$$

where M is the mass matrix, $\ddot{u}$ is the acceleration vector, C is the damping matrix, $\dot{u}$ is the velocity vector, K is the stiffness matrix, u is the displacement vector, and f is the external force vector, containing the nodal loads applied to the system [85].

To compute the response of the system over time, two distinct numerical strategies are commonly used: implicit and explicit time integration. While both approaches solve the same governing equation, they differ in how the unknown variables are estimated at each time step [85].

This distinction can be better understood through a simplified example. Consider a generic function $f(t)$, where the value at a known time t_1 is given and the goal is to estimate the value at a future time $t_1 + 1$. The explicit method calculates the derivative at the known point t_1, leading to the following expression,

$$f(t_1+1) = f(t_1) + \Delta t \cdot \left.\frac{df(t)}{dt}\right|_{t=t_1}, \tag{2.2}$$

conversely, the implicit method evaluates the derivative at the unknown point t_1+1,

$$f(t_1+1) = f(t_1) + \Delta t \cdot \left.\frac{df(t)}{dt}\right|_{t=t_1+1}, \tag{2.3}$$

in these equations, $f(t)$ represents a time-dependent variable, Δt is the time increment between time steps, and $\frac{df(t)}{dt}$ is the slope of the function. Because the implicit method depends on values not yet known, it requires iterative numerical procedures to converge on a solution. The explicit method avoids iteration by using only known values, resulting in a faster, direct computation [85]. This distinction is visually represented in Figure 2.9.

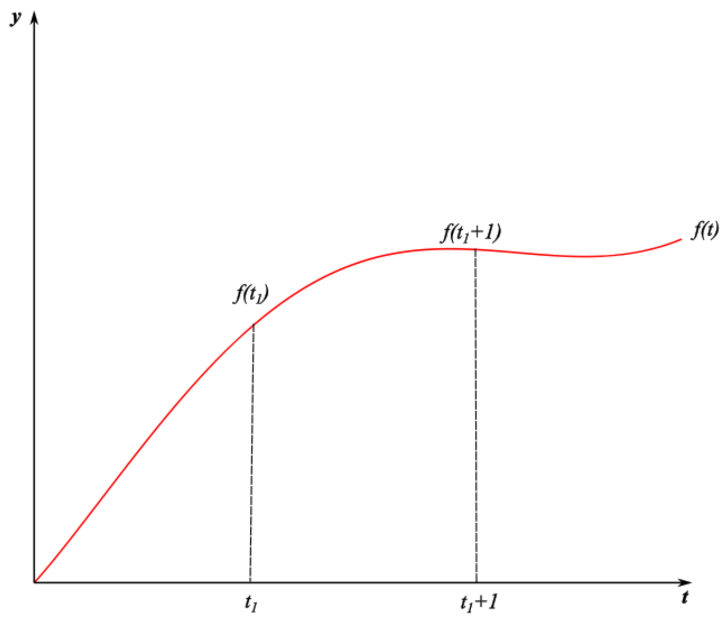

Figure 2.9: Visual representation of the function $f(t)$, highlighting its values at t_1 and t_1+1.

These characteristics influence the suitability of each method. Implicit solvers are generally preferred for slowly evolving problems, such as static analyses, creep, or thermal expansion, where longer time steps and unconditional stability are beneficial. However, this comes at the cost of higher computational effort due to matrix inversion and convergence checks. Explicit solvers, on the other hand, are more appropriate for problems involving short-duration, high-speed phenomena where large deformations, contact, and material failure are expected [86].

The explicit method relies on the central difference integration scheme, which advances the solution through time using a leap-frog approach. The acceleration at time t_i is calculated by,

$$\ddot{u}_i = M^{-1}(f_i^{\text{ext}} - f_i^{\text{int}}), \tag{2.4}$$

in this expression, $\ddot{u}_i$ is the acceleration vector at time increment i, f_i^{ext} is the external nodal force vector at time t_i, f_i^{int} is the internal force vector developed within the elements, and M is the lumped mass matrix, which is diagonal to enable fast inversion [85].

Once the acceleration is known, the velocity and displacement are updated with the following equations,

$$\dot{u}_{i+\frac{1}{2}} = \dot{u}_{i-\frac{1}{2}} + \Delta t \cdot \ddot{u}_i, \tag{2.5}$$

$$u_{i+1} = u_i + \Delta t \cdot \dot{u}_{i+\frac{1}{2}}, \tag{2.6}$$

here, $\dot{u}_{i\pm\frac{1}{2}}$ are the velocities at staggered time steps (midpoints), u_{i+1} is the displacement at the next full time step, and Δt is the explicit time increment. Because the procedure uses only known quantities and avoids stiffness matrix assembly, it is highly efficient and suitable for large, nonlinear models.

Despite its efficiency, the explicit method is conditionally stable. The time increment must satisfy a stability condition based on the maximum natural frequency $\omega_{\max}$ of the system,

$$\Delta t \leq \frac{2}{\omega_{\max}}, \tag{2.7}$$

in this condition, $\omega_{\max}$ is the highest frequency in the model, which depends on the stiffness, density, and element size. As the mesh is refined or the stiffness increases, $\omega_{\max}$ rises, leading to smaller stable increments Δt and consequently a higher number of time steps required to simulate the same physical duration. This effect was particularly evident in the ballistic impact analyses conducted in this work, where highly refined meshes were necessary to accurately capture stress wave propagation and localised damage. While this refinement ensured the physical fidelity of the simulations, it also significantly reduced the stable time increment, increasing computational cost. Nevertheless, the explicit method remains a powerful and reliable approach for simulating dynamic problems involving complex contact interactions, progressive damage, and fragmentation [85].

2.5.1 Element Size Requirements for Resolving Stress Waves

The frequency-based stability condition introduced previously (Equation 2.7) can also be expressed in terms of stress wave propagation and the size of the finite elements [85]. This alternative formulation is particularly relevant for explicit simulations, as it provides a more intuitive and practical criterion for mesh design [87].

In explicit analysis, the stable time increment must be sufficiently small to ensure that a dilatational (longitudinal) wave can traverse each element within a single time step. If this condition is not met, the numerical integration scheme may become unstable, and the wave may bypass elements without adequately interacting with them, resulting in a loss of accuracy [87].

The general stability condition, accounting for potential damping effects, is given by:

$$\Delta t_{\text{stable}} \leq \frac{L}{c_d} \cdot \frac{1}{\sqrt{1+\xi}}, \tag{2.8}$$

where Δt_{stable} is the maximum allowable time increment, L is the characteristic element length, c_d is the dilatational wave speed of the material, and ξ is a damping-related term [87]. In this work, no additional damping mechanisms such as Rayleigh damping or viscoelastic behaviour were applied, thus $\xi = 0$, which is very important for the stability condition adopted.

The wave speed c_d represents the velocity at which compressive disturbances propagate through an elastic medium. It can be defined in terms of the Lamé parameters as:

$$c_d = \sqrt{\frac{\hat{\lambda} + 2\hat{\mu}}{\rho}}, \tag{2.9}$$

where $\hat{\lambda}$ and $\hat{\mu}$ are the first and second Lamé parameters, respectively, and ρ is the material density. These parameters are functions of more commonly used engineering constants, namely Young's modulus, E, and Poisson's ratio, ν, and can be expressed as:

$$\hat{\lambda} = \frac{E\nu}{(1+\nu)(1-2\nu)}, \tag{2.10}$$

$$\hat{\mu} = \frac{E}{2(1+\nu)}. \tag{2.11}$$

Substituting into the previous equation yields the wave speed in terms of E, ν, and ρ:

$$c_d = \sqrt{\frac{E(1-\nu)}{\rho(1+\nu)(1-2\nu)}}. \tag{2.12}$$

In order to resolve wave propagation with sufficient accuracy, the element length L_e must be smaller than the wavelength of the highest frequency of interest in the problem [87]. Otherwise, numerical dispersion may occur, and the stress wave may not be captured correctly. This requirement is defined by the following criterion:

$$L_e \leq \frac{\lambda_{\min}}{n}, \tag{2.13}$$

where $\lambda_{\min}$ is the shortest wavelength that needs to be resolved and n is a safety factor typically taken as 10. The wavelength is related to the wave speed by:

$$\lambda_{\min} = \frac{c_d}{f_{\max}}. \tag{2.14}$$

where $f_{\max}$ is the corresponding maximum frequency. This relationship ensures that the mesh resolution is fine enough to capture the physics of wave propagation in dynamic events such as impacts or high-speed deformations [87]. These calculations were explicitly carried out in Section 4.1.7.1, for the CFRP laminates, and in Section 5.1.1, for the UHMWPE material, ensuring that the chosen element sizes were adequate to resolve stress wave propagation in both cases.

Chapter 3

Failure Models: Theoretical Description

The previous discussion in Section 2.1.3 addressed the structural concept and protective mechanisms of hybrid laminates, such as the sequential energy absorption of ceramic/UHMWPE systems. To replicate these behaviours in numerical simulations, material models are required that define both the onset of failure and the subsequent damage evolution.

Failure criteria in the literature vary from empirical formulations that do not distinguish between fibre and matrix modes (e.g., Tsai–Wu, Tsai–Hill, Hoffman) to more detailed models, such as the Hashin, Puck, and Chang–Chang criteria, that treat these modes separately.

In this work, the selected models are:

- Hashin criterion in 2D and 3D formulations,
- Cohesive zone model for interlaminar damage,
- JH-2 model for ceramic materials.

This chapter presents the theoretical basis and damage evolution laws for each model, providing the foundation for their implementation in the developed finite element framework. Its structure and development were guided by the foundational work of André Rocha, whose thesis served as both a structural and conceptual reference [88]. While the content has been independently developed and adapted to the specific scope of the present study, his methodological organisation and theoretical depth provided valuable inspiration for how failure models are analysed and presented herein. In addition, the work of Pedro Ponces

Camanho was consulted during the development of this chapter, offering a valuable theoretical foundation on the formulation and interpretation of composite failure criteria and supporting the contextualisation of the models implemented in this study [89].

3.1 Hashin Failure Criterion

The failure criterion commonly referred to as the Hashin model was first introduced in 1973 by Z. Hashin and A. Rotem, known then as the Hashin–Rotem criterion [90]. In 1980, Hashin presented a refined formulation that has since become widely adopted in both 2D and 3D settings [91].

The criterion defines four distinct intralaminar failure modes: fibre tension, fibre compression, matrix tension, and matrix compression. Each mode is evaluated independently via a quadratic failure function. Damage is assumed to initiate when the respective function reaches or exceeds unity.

It is important to highlight that both the 2D and 3D versions of this criterion account exclusively for intralaminar failure mechanisms. Interlaminar damage modes, such as delamination, are not included in the formulation. However, as discussed in the literature review (Section 2.1.3), delaminations are commonly observed in impact events and their exclusion can lead to discrepancies between numerical predictions and experimental data.

In all expressions presented bellow, the stress components σ_{11}, σ_{22}, and σ_{33} refer to normal stresses acting along the fibre direction, transverse (matrix) direction, and thickness direction of the lamina, respectively. The terms σ_{12}, σ_{13}, and σ_{23} represent the corresponding shear stresses within the principal material planes. The parameters X_T and X_C define the lamina's tensile and compressive strengths along the fibre direction, whereas Y_T and Y_C represent the same quantities in the transverse direction. Finally, the shear strengths associated with each plane are denoted by S_{12}, S_{13}, and S_{23}.

3.1.1 Hashin 2D Formulation

The 2D version is applicable under plane stress conditions (i.e., $\sigma_{33} = \sigma_{13} = \sigma_{23} = 0$) and is typically used in shell or continuum shell elements.

Fibre tension failure ($\sigma_{11} \geq 0$):

$$\left(\frac{\sigma_{11}}{X_T}\right)^2 + \left(\frac{\sigma_{12}}{S_{12}}\right)^2 \geq 1. \tag{3.1}$$

Fibre compression failure ($\sigma_{11} < 0$):

$$\left(\frac{\sigma_{11}}{X_C}\right) \geq 1. \tag{3.2}$$

Matrix tension failure ($\sigma_{22} \geq 0$):

$$\left(\frac{\sigma_{22}}{Y_T}\right)^2 + \left(\frac{\sigma_{12}}{S_{12}}\right)^2 \geq 1. \tag{3.3}$$

Matrix compression failure ($\sigma_{22} < 0$):

$$\left(\frac{\sigma_{22}}{2S_{23}}\right)^2 + \left[\left(\frac{Y_C}{2S_{23}}\right)^2 - 1\right] \cdot \frac{\sigma_{22}}{Y_C} + \left(\frac{\sigma_{12}}{S_{12}}\right)^2 \geq 1. \tag{3.4}$$

In some formulations, a weighting factor α is used to adjust the contribution of shear stress to fibre tension failure ($\sigma_{11} \geq 0$):

$$\left(\frac{\sigma_{11}}{X_T}\right)^2 + \alpha\left(\frac{\sigma_{12}}{S_{12}}\right)^2 \geq 1. \tag{3.5}$$

3.1.2 Hashin 3D Formulation

The 3D version of the criterion is suited for solid elements and considers all components of the stress tensor.

Fibre tension failure ($\sigma_{11} \geq 0$):

$$\left(\frac{\sigma_{11}}{X_T}\right)^2 + \left(\frac{\sigma_{12}}{S_{12}}\right)^2 + \left(\frac{\sigma_{13}}{S_{13}}\right)^2 \geq 1. \tag{3.6}$$

Fibre compression failure ($\sigma_{11} < 0$):

$$\left(\frac{\sigma_{11}}{X_C}\right) \geq 1. \tag{3.7}$$

Matrix tension failure ($\sigma_{22} + \sigma_{33} \geq 0$):

$$\left(\frac{\sigma_{22}+\sigma_{33}}{Y_T}\right)^2 + \frac{1}{S_{23}^2}(\sigma_{23}^2 - \sigma_{22}\sigma_{33})\left(\frac{\sigma_{12}}{S_{12}}\right)^2 + \left(\frac{\sigma_{13}}{S_{13}}\right)^2 \geq 1. \tag{3.8}$$

Matrix compression failure ($\sigma_{22} + \sigma_{33} < 0$):

$$\left(\frac{\sigma_{22}+\sigma_{33}}{2S_{23}}\right)^2 + \left[\left(\frac{Y_C}{2S_{23}}\right)^2 - 1\right] \cdot \frac{\sigma_{22}+\sigma_{33}}{Y_C} + \frac{1}{S_{23}^2}(\sigma_{23}^2 + \sigma_{22}\sigma_{33}) + \left(\frac{\sigma_{12}}{S_{12}}\right)^2 + \left(\frac{\sigma_{13}}{S_{13}}\right)^2 \geq 1. \tag{3.9}$$

If desired, and, as mentioned before, the shear terms can also be scaled using an α parameter ($\sigma_{11} \geq 0$):

$$\left(\frac{\sigma_{11}}{X_T}\right)^2 + \alpha\left(\frac{\sigma_{12}}{S_{12}}\right)^2 + \alpha\left(\frac{\sigma_{13}}{S_{13}}\right)^2 \geq 1. \tag{3.10}$$

For a better understanding of the differences between the two formulations, a summary is provided in Table 3.1.

Table 3.1: Comparison between the 2D and 3D formulations of the Hashin failure criterion.

Feature	**Hashin 2D**	**Hashin 3D**
Stress state	$\sigma_{11}, \sigma_{22}, \sigma_{12}$	Full stress tensor σ_{ij}
Through-thickness terms	Not considered	Includes $\sigma_{13}, \sigma_{23}, \sigma_{33}$
Matrix failure condition	Based on σ_{22} only	Based on $\sigma_{22} + \sigma_{33}$
Compression nonlinearity	Present in σ_{22} term	Coupled $\sigma_{22}\sigma_{33}$ interaction terms
Element applicability	Shell or continuum shell elements	Solid elements
α parameter support	Optional for σ_{12}	Optional for σ_{12} and σ_{13}

Once damage is initiated according to the Hashin failure criterion, a damage evolution law is required to describe the progressive degradation of material stiffness and the associated dissipation of fracture energy. In composite materials, this behaviour is commonly modelled using continuum damage mechanics, in which the material response is governed by internal scalar variables that represent the level of degradation. Each failure mechanism such as fibre tension, fibre compression, matrix tension, and matrix compression, is associated with a damage variable d, which evolves from 0 (undamaged state) to 1 (fully failed).

The degradation of stiffness is controlled by an equivalent displacement variable, denoted $\delta_{I,\mathrm{eq}}$, which evolves as a function of the applied stress and the nature of the active failure mode I. Damage begins to evolve when this equivalent displacement exceeds a threshold value $\delta^0_{I,\mathrm{eq}}$ corresponding to the onset of failure. Complete material failure is assumed when the equivalent displacement reaches a critical value $\delta^f_{I,\mathrm{eq}}$. For each failure mode, the damage variable evolves according to the following law:

$$d_I = \frac{\delta^f_{I,\mathrm{eq}}(\delta_{I,\mathrm{eq}} - \delta^0_{I,\mathrm{eq}})}{\delta_{I,\mathrm{eq}}(\delta^f_{I,\mathrm{eq}} - \delta^0_{I,\mathrm{eq}})}, \tag{3.11}$$

in this expression, d_I denotes the damage variable associated with the failure mode I, which may correspond to fibre tension (ft), fibre compression (fc), matrix tension (mt), or matrix compression (mc). The parameter $\delta_{I,\mathrm{eq}}$ represents the current equivalent displacement, $\delta^0_{I,\mathrm{eq}}$ is the value at which damage initiates, and $\delta^f_{I,\mathrm{eq}}$ is the value at which the material is fully degraded in that mode. This formulation ensures that the damage variable begins at zero and increases smoothly to one as failure progresses.

The equivalent displacement is calculated from the same stress components used in the corresponding Hashin failure function. For instance, in the case of fibre tension, the equivalent displacement is computed as:

$$\delta^f_{ft,\mathrm{eq}} = \sqrt{\left(\frac{\sigma_{11}}{X_T}\right)^2 + \left(\frac{\sigma_{12}}{S_{12}}\right)^2 + \left(\frac{\sigma_{13}}{S_{13}}\right)^2}. \tag{3.12}$$

In matrix-dominated failure modes, additional transverse and out-of-plane stresses contribute. For matrix tension, the equivalent displacement is given by:

$$\delta^f_{mt,\mathrm{eq}} = \sqrt{\left(\frac{\sigma_{22}+\sigma_{33}}{Y_T}\right)^2 + \left(\frac{\sigma_{12}}{S_{12}}\right)^2 + \left(\frac{\sigma_{13}}{S_{13}}\right)^2 + \left(\frac{\sigma_{23}}{S_{23}}\right)^2}. \tag{3.13}$$

To ensure physical consistency, the energy dissipated during softening must match the fracture energy G_c of the material. Assuming a linear softening law, the area under the traction–displacement curve is equivalent to the fracture energy, and can be expressed as:

$$G_c = \int_{\delta_0}^{\delta_f} \sigma(\delta)\, d\delta = \frac{1}{2} t_0(\delta_f - \delta_0), \tag{3.14}$$

solving for the final displacement gives:

$$\delta_f = \frac{2G_c}{t_0} + \delta_0. \tag{3.15}$$

This expression provides a direct link between the experimentally measured fracture energy, the stress at damage initiation t_0, and the softening length required to complete material degradation.

The evolution of the damage variable d as a function of the equivalent displacement $\delta_{I,\mathrm{eq}}$ is illustrated in Figure 3.1. As shown, the damage remains zero until the onset of failure at $\delta^0_{I,\mathrm{eq}}$, after which it increases progressively following the softening law, reaching $d = 1$ when the equivalent displacement attains its final value $\delta^f_{I,\mathrm{eq}}$.

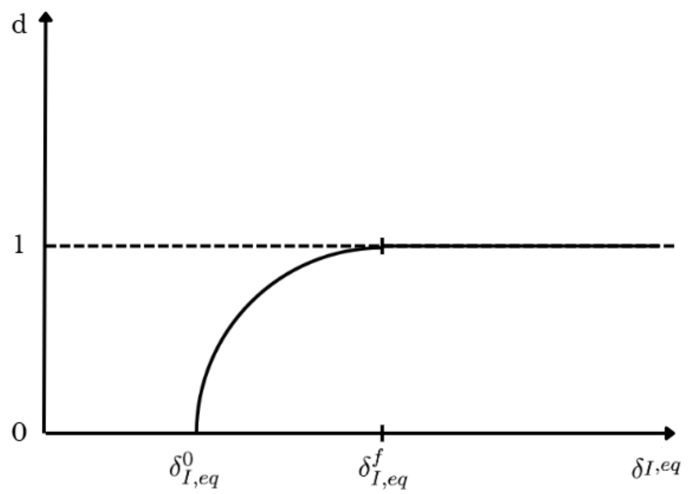

Figure 3.1: Evolution of the damage variable d as a function of the equivalent displacement $\delta_{I,\mathrm{eq}}$. The curve follows a linear softening law, beginning at $d = 0$ and progressing to $d = 1$ at complete failure.

The presence of damage alters the stress–strain relation, which is commonly rewritten as:

$$\sigma = (1-d)\,\mathbf{C}_0 : \varepsilon, \tag{3.16}$$

here, σ is the stress tensor, ε the strain tensor, and $\mathbf{C}_0$ the undamaged stiffness tensor of the material. While this scalar formulation is sufficient in simple cases, more refined models implement directional stiffness degradation to capture the anisotropic nature of failure in laminated composites. In such cases, the degraded stiffness tensor is expressed in tensorial form as:

$$\mathbf{C}_d = \mathbf{T}^T (1-\mathbf{D})\,\mathbf{T}\,\mathbf{C}_0, \tag{3.17}$$

in this expression, $\mathbf{C}_d$ is the damaged stiffness tensor, $\mathbf{T}$ is a transformation matrix from local to global coordinates, and $\mathbf{D}$ is a diagonal matrix containing the individual damage variables associated with each direction. This formulation allows independent degradation of stiffness terms such as E_1, E_2, G_{12}, and G_{23} based on the specific failure mechanism.

Finally, in explicit finite element simulations, elements are typically removed from the analysis once they are fully damaged. This is commonly implemented using the following condition:

$$\max(d_I) \geq 1.0. \tag{3.18}$$

This criterion ensures that once any of the damage variables reaches full degradation, the element is deleted from the model and no longer contributes to stiffness or load transfer. This approach maintains numerical stability and reflects the complete loss of structural integrity in the failed region.

An essential aspect in impact simulations is the effect of strain rate, as the mechanical properties of composites are strongly rate-dependent. To account for this, the methodology proposed by Millen et al. [92] was adopted, in which a strain-rate-dependent scaling factor β modifies selected material properties such as stiffness and strength. This factor is defined through a piecewise relation, distinguishing between quasi-static, high-rate, and intermediate regimes:

$$\beta = \begin{cases} 1.0 & \text{if } \dot{\varepsilon}_2 \leq \dot{\varepsilon}_{\text{low}} \\ \frac{(\dot{\varepsilon}_2 - \dot{\varepsilon}_{\text{low}})(\beta_{\max}-1)}{\dot{\varepsilon}_{\text{high}} - \dot{\varepsilon}_{\text{low}}} + 1 & \text{if } \dot{\varepsilon}_{\text{low}} < \dot{\varepsilon}_2 < \dot{\varepsilon}_{\text{high}} \\ \beta_{\max} & \text{if } \dot{\varepsilon}_2 \geq \dot{\varepsilon}_{\text{high}} \end{cases} \tag{3.19}$$

where $\dot{\varepsilon}_2$ denotes the transverse strain rate, $\dot{\varepsilon}_{\text{low}}$ and $\dot{\varepsilon}_{\text{high}}$ are the lower and upper reference strain rates, respectively, and $\beta_{\max}$ is the maximum scaling factor.

The scaling factor is then applied to the material properties of interest. For instance, the effective transverse stiffness can be written as:

$$E_{2f} = \beta E_2, \tag{3.20}$$

and for strength values:

$$X_{Tf} = \beta X_T, \tag{3.21}$$

$$Y_{Tf} = \beta Y_T, \tag{3.22}$$

$$G_{Cf}^{mt} = \beta G_C^{mt}. \tag{3.23}$$

At each time increment, the instantaneous strain rate is computed as:

$$\dot{\varepsilon}^t = \frac{\varepsilon^t - \varepsilon^{t-\Delta t}}{\Delta t}, \tag{3.24}$$

ensuring that β evolves dynamically during the simulation. While the framework follows Millen et al. [92], the specific reference strain rates and scaling factors must be defined according to the experimental data of the material under study. This ensures that the stiffening and strengthening effects observed at high strain rates are accurately captured in ballistic impact simulations.

3.2 Johnson–Holmquist II Model

The implementation and description of the JH-2 model presented in this chapter were developed based on the methodology and formulations outlined in the work of Goda and Girardot [93].

The JH-2 model is a constitutive formulation developed to characterise the mechanical behaviour of brittle materials subjected to extreme dynamic loading conditions, including high strain rates, elevated pressures, and large deformations. It is widely applied in the simulation of ceramic materials, such as alumina, under ballistic impact. The model comprises three core components: a pressure-dependent strength model for both intact and fractured states, a damage evolution law based on plastic strain accumulation, and an equation of state (EOS) that describes the volumetric response under compression and tension, including bulking effects.

The strength of the material is defined in terms of the equivalent von Mises stress, normalised with respect to the Hugoniot Elastic Limit (HEL). The normalised stress, σ^*, is expressed as:

$$\sigma^* = \sigma_i^* - D(\sigma_i^* - \sigma_f^*), \tag{3.25}$$

here, σ_i^* and σ_f^* are the intact and fractured normalised strengths, and D is a scalar internal damage variable ranging from 0 (intact) to 1 (fully damaged). These quantities are all normalised by σ_{HEL}, the equivalent stress at the HEL. The actual von Mises equivalent stress is computed as:

$$\sigma = \sqrt{\frac{1}{2}\left[(\sigma_x-\sigma_y)^2+(\sigma_y-\sigma_z)^2+(\sigma_z-\sigma_x)^2+6(\tau_{xy}^2+\tau_{yz}^2+\tau_{zx}^2)\right]}. \tag{3.26}$$

The intact strength is defined as:

$$\sigma_i^* = \left(A+(P^*+T^*)^N\right)(1+C\ln\dot{\varepsilon}^*), \tag{3.27}$$

while the fractured strength is given by:

$$\sigma_f^* = B(P^*)^M(1+C\ln\dot{\varepsilon}^*), \quad \sigma_f^* \le \sigma_{\max}^*. \tag{3.28}$$

In these equations, $P^* = P/P_{\text{HEL}}$ is the normalised pressure, $T^* = T/P_{\text{HEL}}$ is the normalised maximum tensile pressure, and $\dot{\varepsilon}^* = \dot{\varepsilon}/\dot{\varepsilon}_0$ is the strain rate normalised by a reference value (typically $\dot{\varepsilon}_0 = 1\,\text{s}^{-1}$). The parameters A, B, C, N, and M are determined from experimental calibration. The fractured strength is also capped by a maximum value $\sigma_{\max}^*$ to ensure numerical stability.

Damage accumulates incrementally as a function of the plastic deformation. The evolution of the damage variable D is given by the summation:

$$D = \sum \frac{\Delta\varepsilon^p}{\varepsilon_f^p}, \tag{3.29}$$

here, $\Delta\varepsilon^p$ is the increment in equivalent plastic strain during an integration step, and ε_f^p is the equivalent plastic strain required to cause fracture at the current pressure. The fracture strain is pressure-dependent and is defined as:

$$\varepsilon_f^p = D_1(P^*+T^*)^{D_2}, \tag{3.30}$$

where, D_1 and D_2 are material-specific damage parameters. This formulation ensures a smooth and pressure-sensitive accumulation of damage under dynamic loading.

The JH-2 model also defines the pressure-volume response through a piecewise polynomial EOS. For compressive states ($\mu > 0$), where μ is the volumetric strain, the pressure is given by:

$$P = K_1\mu + K_2\mu^2 + K_3\mu^3. \tag{3.31}$$

For tensile states ($\mu < 0$), a linear response is assumed:

$$P = K_1\mu. \tag{3.32}$$

The volumetric strain is defined as $\mu = \rho/\rho_0 - 1 = V_0/V - 1$, where ρ and ρ_0 (or V and V_0) are the current and reference density, respectively. The coefficients K_1, K_2, and K_3 are material bulk modulus terms. This polynomial EOS enables the representation of nonlinear compressibility in ceramics under impact.

As damage increases ($D > 0$), the model incorporates the effect of bulking by modifying the compressive EOS. An additional pressure term, ΔP, is introduced to simulate dilation effects observed in fractured ceramics:

$$P = K_1\mu + K_2\mu^2 + K_3\mu^3 + \Delta P \quad \text{for} \quad 0 < D \leq 1,\ \mu > 0. \tag{3.33}$$

The bulking-induced pressure increment, ΔP, is derived from energy balance principles and evolves from $\Delta P = 0$ at $D = 0$ to a maximum value $\Delta P_{\max}$ when $D = 1$. The loss of deviatoric elastic energy ΔU associated with material softening is converted into additional volumetric energy, leading to the following increment:

$$\Delta P_{t+\Delta t} = -K_1\mu_{t+\Delta t} + \sqrt{(K_1\mu_{t+\Delta t} + \Delta P_t)^2 + 2\beta K_1 \Delta U}, \tag{3.34}$$

here, ΔP_t is the bulking pressure at the previous increment, and β is a material parameter governing the conversion efficiency of elastic energy to volumetric pressure. This bulking mechanism plays a key role in capturing the post-failure volumetric expansion observed in ceramic materials subjected to high-energy impacts.

Initiation: Quadratic nominal stress criterion

3.3 Interlaminar Failure Model

To describe the behaviour of this failure mode, the approach proposed by Camanho and Dávila was adopted, as their formulation has become widely recognised for accurately capturing the initiation and propagation of delamination under mixed-mode loading [94]. Additionally, the experimental insights and theoretical background provided in *Experimental Characterization of Advanced Composite Materials* by Adams, Carlsson, and Pipes offered valuable support in contextualising the mechanical response of laminated composites and validating the assumptions behind the cohesive zone approach [95].

Delamination, or interlaminar failure, is a dominant failure mode in laminated composites, arising from the loss of adhesion between plies. This failure mechanism plays a critical role in the structural degradation of composite structures subjected to transverse and impact loading. It originates from the concentration of out-of-plane stresses at ply interfaces, particularly near geometric discontinuities or free edges, and propagates when the energy release rate exceeds the material's interfacial toughness.

The onset of damage is governed by a mixed-mode quadratic stress criterion, which accounts for the interaction between normal and shear tractions acting across the interface. The condition for initiation is given by:

$$\left(\frac{\langle t_n \rangle}{t_{n,\max}}\right)^2 + \left(\frac{t_s}{t_{s,\max}}\right)^2 + \left(\frac{t_t}{t_{t,\max}}\right)^2 \geq 1. \tag{3.35}$$

Here, t_n, t_s, and t_t denote the normal and shear traction components, while $t_{n,\max}$, $t_{s,\max}$, and $t_{t,\max}$ represent their corresponding critical values. The Macauley brackets ensure that compressive normal tractions do not contribute to the damage onset, as delamination typically initiates under tensile loading. This criterion reflects a combination of Mode I (opening), Mode II (sliding), and Mode III (tearing) failure modes. The following figure provides a visual illustration of these interlaminar failure mechanisms.

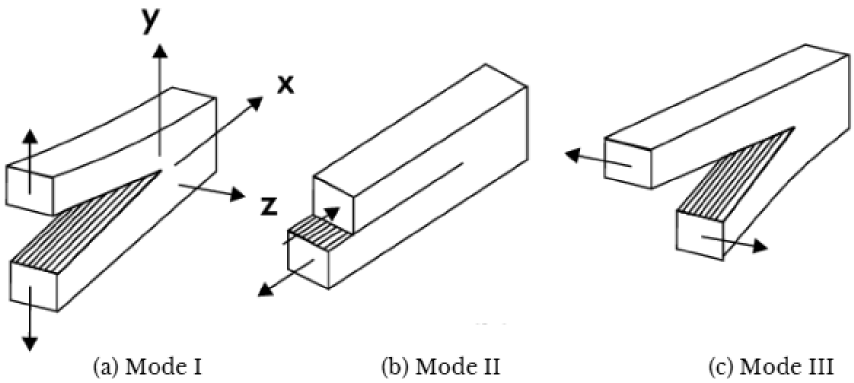

Figure 3.2: Modes of crack surface displacement (Adapted from [95]).

The tractions before damage initiation are linked to the separation displacements through a linear elastic relationship:

$$\begin{bmatrix} t_n \\ t_s \\ t_t \end{bmatrix} = \begin{bmatrix} K_n & 0 & 0 \\ 0 & K_s & 0 \\ 0 & 0 & K_t \end{bmatrix} \begin{bmatrix} \delta_n \\ \delta_s \\ \delta_t \end{bmatrix}, \tag{3.36}$$

where K_n, K_s, and K_t are the penalty stiffnesses in each direction, and δ_n, δ_s, δ_t denote the relative displacements across the interface.

Once damage is initiated, it evolves according to a linear softening law governed by the work of separation. The evolution of the damage variable d is defined as:

$$d = \frac{\delta_{\text{eff}}^f \left(\delta_{\text{eff}}^{\max} - \delta_{\text{eff}}^0\right)}{\delta_{\text{eff}}^{\max} \left(\delta_{\text{eff}}^f - \delta_{\text{eff}}^0\right)}. \tag{3.37}$$

The variable δ_{eff}^0 denotes the effective displacement at the onset of damage, $\delta_{\text{eff}}^{\max}$ is the peak value reached throughout the loading history, and δ_{eff}^f corresponds to the displacement at complete failure. The effective displacement is given by:

$$\delta_{\text{eff}} = \sqrt{\langle \delta_n \rangle^2 + \delta_s^2 + \delta_t^2}. \tag{3.38}$$

The initial effective traction is defined as:

$$T_{\text{eff}}^0 = K_0 \delta_{\text{eff}}^0. \tag{3.39}$$

The final failure threshold is obtained from the fracture energy G_c as:

$$\delta_{\text{eff}}^f = \frac{2G_c}{T_{\text{eff}}^0}. \tag{3.40}$$

To incorporate mixed-mode effects in the fracture process, a mode-dependent energy interaction law is applied. Two widely used approaches are the power law criterion and the Benzeggagh–Kenane (B-K) criterion.

The power law criterion expresses the interaction between Mode I and Mode II fracture energies as:

$$\left(\frac{G_I}{G_{IC}}\right)^{\alpha} + \left(\frac{G_{II}}{G_{IIC}}\right)^{\alpha} = 1. \tag{3.41}$$

Alternatively, the B-K criterion offers a more accurate representation for composites, especially when all three fracture modes are involved. It is defined as:

$$G_c = G_{IC} + (G_T - G_{IC}) \left(\frac{G_{\text{shear}}}{G_T}\right)^{\eta}, \tag{3.42}$$

where $G_T = G_I + G_{II} + G_{III}$ and $G_{\text{shear}} = G_{II} + G_{III}$. The exponent η is obtained experimentally.

To determine when full decohesion occurs, the critical relative displacement δ_m' is calculated by equating the energy release rate to G_c. For the B-K criterion:

$$\delta_m' = \begin{cases} \sqrt{\frac{2}{K\delta_m'}} \left[G_{IC} + (G_T - G_{IC}) \left(\frac{\beta^2}{1+\beta^2}\right)^{\eta}\right] & \text{if } \delta_3 > 0 \\ \sqrt{(\delta_1')^2 + (\delta_2')^2} & \text{if } \delta_3 \leq 0 \end{cases}. \tag{3.43}$$

For the power law criterion:

$$\delta_m' = \begin{cases} \sqrt{\frac{2(1+\beta^2)}{K\delta_m'} \left(\left(\frac{1}{G_{IC}}\right)^{\alpha} + \left(\frac{\beta^2}{G_{IIC}}\right)^{\alpha}\right)^{-1/\alpha}} & \text{if } \delta_3 > 0 \\ \sqrt{(\delta_1')^2 + (\delta_2')^2} & \text{if } \delta_3 \leq 0 \end{cases}. \tag{3.44}$$

The mode mixity ratio β is defined as:

$$\beta = \frac{\delta_{\text{shear}}}{\delta_3} = \frac{\sqrt{\delta_1^2 + \delta_2^2}}{\delta_3}. \tag{3.45}$$

Regardless of the criterion adopted, pure mode loading is recovered as a special case, with $\beta = 0$ corresponding to Mode I and $\beta \to \infty$ to shear-dominated delamination.

By combining a rigorous initiation criterion with an energy-based evolution law, the cohesive zone model used here provides a physically consistent framework for simulating delamination under both quasi-static and dynamic loading conditions.

3.4 Implementation of Failure Criteria in Numerical Modelling

The purpose of this subsection is to describe the implementation of the failure models previously presented within the finite element framework developed in this thesis. Numerical simulations were performed using Abaqus/Explicit, with the aim of reproducing the progressive damage mechanisms observed under dynamic loading conditions [96]. The different models were applied to represent the failure behaviour of ceramic and composite domains, including both intralaminar and interlaminar failure modes. Their incorporation was achieved either through native material definitions provided by the software or by means of user-defined subroutines when more advanced formulations were required.

The 2D Hashin criterion, as well as the interlaminar failure model based on cohesive zone elements, are both available by default in the Abaqus/Explicit material library. These models were activated through the Graphical User Interface (GUI), without the need for custom coding, and configured according to the formulations detailed in the Abaqus documentation [96]. Their use allowed the direct simulation of fibre and matrix failure in plane stress conditions, as well as delamination initiation and propagation at ply interfaces.

The 3D version of the Hashin criterion, necessary to capture out-of-plane stress effects in thick composite domains, is not natively available in Abaqus. To address this limitation, a user-defined material model was implemented via the VUMAT subroutine interface. The subroutine used in this work is based on the model developed by Miranda [97], which incorporates orthotropic elasticity, Hashin-based intralaminar failure, strain rate effects, and progressive stiffness degradation. This implementation was integrated directly into the simulation framework without requiring further modification, ensuring compatibility with the explicit dynamic environment of Abaqus.

In addition, the JH-2 model, suitable for capturing the brittle response of ceramic materials under high strain rates and pressures, was used to simulate the projectile–target interaction. Although this model is included in the Abaqus/Explicit kernel, it is not accessible through the GUI. Instead, it must be invoked by defining a specific material name in the input file (`.inp`) and assigning the appropriate parameters. The procedure adopted to activate and integrate this model, including its coupling with the composite domain, is described in Appendix A.

To summarise the different implementation routes used for each failure model, Table 3.2 provides an overview of their availability in Abaqus/Explicit and the corresponding method of access or integration. This distinction highlights the use of both built-in capabilities and user-defined routines in order to incorporate all the necessary material behaviour in the numerical framework developed.

Table 3.2: Implementation route and availability of the failure models adopted in this dissertation.

Failure Model	**Availability in Abaqus**	**Implementation Method**
Hashin 2D	Available	GUI
Hashin 3D	Not available	VUMAT
Interlaminar damage	Available	GUI
JH-2	Available	INP keyword input

Chapter 4

Case Study on High-Velocity Ballistic Impacts

4.1 Model Construction and Setup

The numerical model in Abaqus was developed following a structured approach to ensure accuracy and reproducibility. This section outlines the process from geometry definition to the setup of analysis steps, interactions, and boundary conditions, with modelling choices guided by finite element best practices and literature on high-velocity ballistic impacts [93].

4.1.1 Part Definition and Model Geometry

The finite element model developed in Abaqus/CAE represents a ballistic impact on a hybrid target composed of a ceramic front layer and a composite laminate backing, impacted by a rigid projectile. All parts were modelled as 3D solids using extruded sketches, with appropriate partitioning to enable mesh control and subsequent assignment of material orientations.

4.1.1.1 Target Plate

The target plate was modelled as a 3D deformable solid with a rectangular base of 150 mm × 100 mm, matching the geometry of the experimental specimens. The part was extruded to a total thickness of 14.8 mm, consisting of: 4.8 mm of ceramic strike face and 10 mm of composite laminate.

The composite section was intended to be made up of 16 individual plies. However, to optimise the modelling process and avoid repetitive partitioning, the initial approach involved creating only one composite ply. This single ply was carefully partitioned (see next subsection), and subsequently duplicated 15 times using the Create Part from Instance tool in Abaqus/CAE. This ensured that the entire laminate stack comprised 16 identical ply parts, each inheriting the original partitions, while still allowing independent assignment of orientation and material properties.

4.1.1.2 In-Plane Partitioning

In-plane partitioning was applied to allow local mesh refinement and better control of element quality around the impact region. This involved:

- Creating a 20 mm × 20 mm square at the centre of the plate to define the impact zone and,
- A larger 60 mm × 60 mm square centred around it as a transition region.

Diagonal partitions were added to connect opposite corners, improving mesh regularity and reducing element distortion during impact.

These partitions were first applied to the ceramic layer and then to the initial composite ply. By creating the full set of in-plane partitions before duplication, the entire laminate could be assembled with consistent meshing and geometry, while significantly reducing modelling time. This approach avoids the need to manually apply the same partitioning operations to each of the 16 ply parts, as mentioned before.

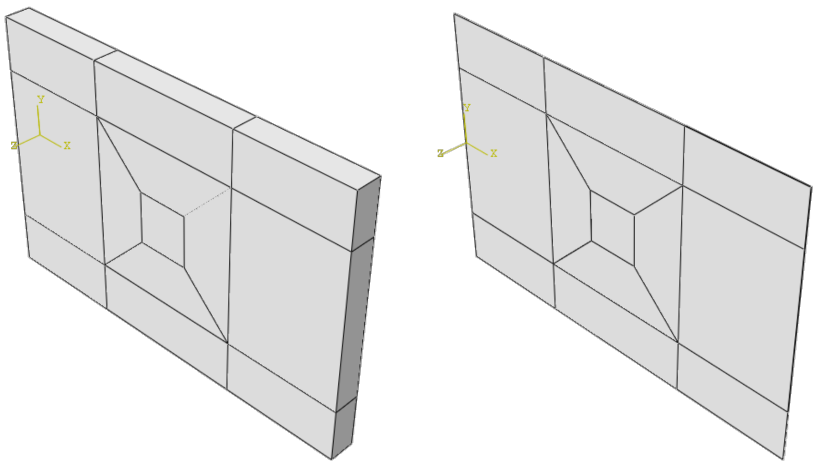

(a) (b)

Figure 4.1: Parts: (a) Ceramic, and (b) Ply-1 of composite.

4.1.1.3 Projectile

The projectile was created as a 3D analytical rigid solid in Abaqus/CAE. Since an analytical rigid part cannot be constructed by extruding a circular profile, the geometry was instead defined by sketching a rectangle measuring 8.25 mm × 32 mm (corresponding to the projectile radius and length, respectively) and performing a revolve operation around the longitudinal axis. This method allowed the generation of a full cylindrical geometry despite the limitations of the analytical rigid body tool.

The analytical rigid formulation simplifies the simulation by neglecting any deformation of the projectile, thereby focusing computational effort on the response of the target plate.

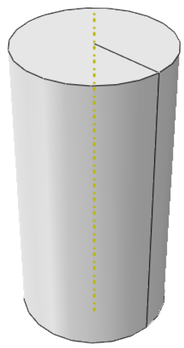

Figure 4.2: Part: Projectil.

4.1.2 Material Definition and Section Assignment

The model included distinct materials corresponding to each physical region of the ballistic system: ceramic strike face, composite plies, and projectile. These were defined in the Property module of Abaqus/CAE and assigned to the respective parts using solid sections. In the case of the composite region, individual ply orientations were defined during section assignment to accurately represent the stacking sequence of the hybrid laminate. Throughout this stage, a single, consistent unit system was enforced across Abaqus/CAE and the `.inp` file for all quantities (geometry, material parameters, contact data, loads, boundary conditions, kinematic values, and output requests). Inconsistencies in units are a frequent source of nonphysical behaviour, so unit consistency was verified at every step.

4.1.2.1 Ceramic Layer (Alumina)

The strike face was modelled as alumina ceramic. The parameters used for the constitutive description are listed in Table 4.1. The alumina response under high-velocity impact was represented with the JH-2 formulation.

The exact procedure used to enter the JH-2 material directly in the `.inp` file is provided step by step in Appendix A (parameter blocks, required options, and Abaqus/Explicit activation details). It is important to note that the worked example in the appendix uses silicon carbide. To run the present simulations with alumina, one simply replaces the SiC parameters in that template with the alumina values from Table 4.1.

Table 4.1: Properties of 99.5% purity alumina [93], [98], [99].

Property	Unit	Value	Property	Unit	Value
ρ	kg/m^3	3800	HEL	GPa	5.90
G	GPa	152	P_{Hel}	GPa	2.20
A	-	0.99	β	-	1.00
B	-	0.77	D_1	-	0.01
C	-	0	D_2	-	1.00
n	-	0.64	ε_{fmax}	-	2.00
m	-	0.60	ε_{fmin}	-	0
$\dot{\varepsilon}_0$	s^{-1}	1.00	K_1	GPa	200
T	MPa	275	K_2	GPa	0
σ_{Imax}	GPa	∞	K_3	GPa	0
σ_{fmax}	GPa	0.50	F_s	-	0.20

4.1.2.2 Composite Region (CFRP)

The laminate followed a symmetric stacking sequence of $[45/-45/0/90/45/-45/0/90]_s$, corresponding to a total of 16 plies. In the finite element model, these 16 plies were explicitly represented, with each ply defined as an individual solid part within the assembly. While all plies share identical geometry, they were assigned distinct material orientations and section properties to replicate the laminate stacking sequence.

Material behaviour of the composite plies was defined through a user-defined constitutive model implemented via the VUMAT subroutine. This subroutine governs both the elastic orthotropic response and the progressive damage mechanisms associated with carbon fibre composites. In particular, it handles the onset and evolution of fibre and matrix failure modes, including strain-rate effects.

To define the composite material in Abaqus, the following steps were followed:

1. Density: Specified using the "Density" option in the Property module, based on experimental data (Figure 4.3).

2. Variables (Depvar): The number of solution-dependent state variables was defined using "Depvar", as required by the VUMAT implementation (Figure 4.4).

3. Mechanical Constants: A total of 16 constants were inserted under the "Mechanical Constants" field. These correspond to elastic properties, strength values, and other parameters used internally by the subroutine (Figure 4.5).

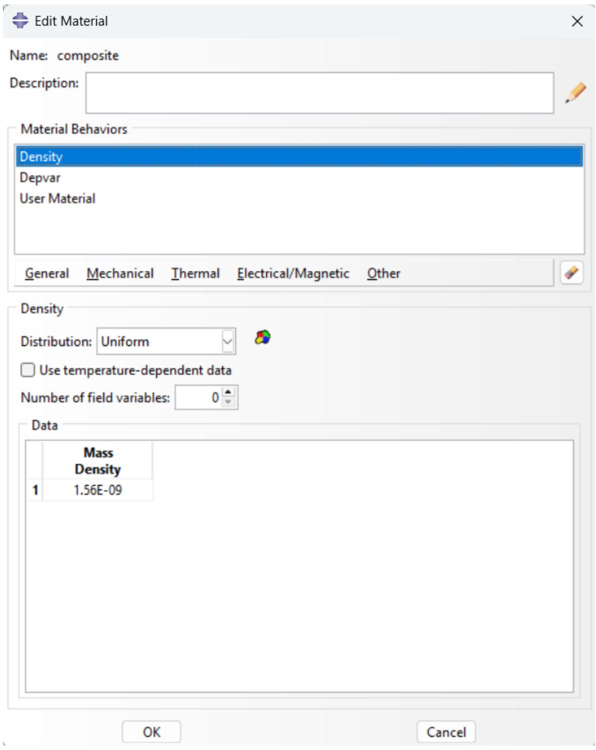

Figure 4.3: Density definition.

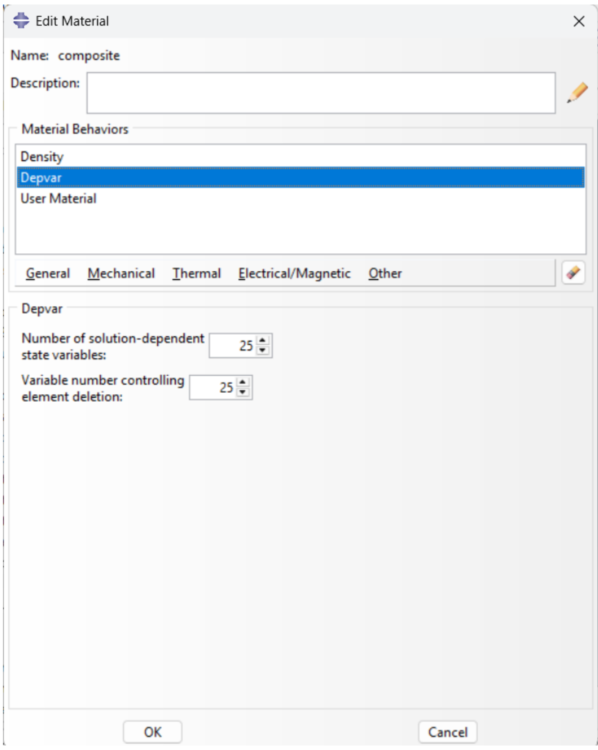

Figure 4.4: Depvar definition.

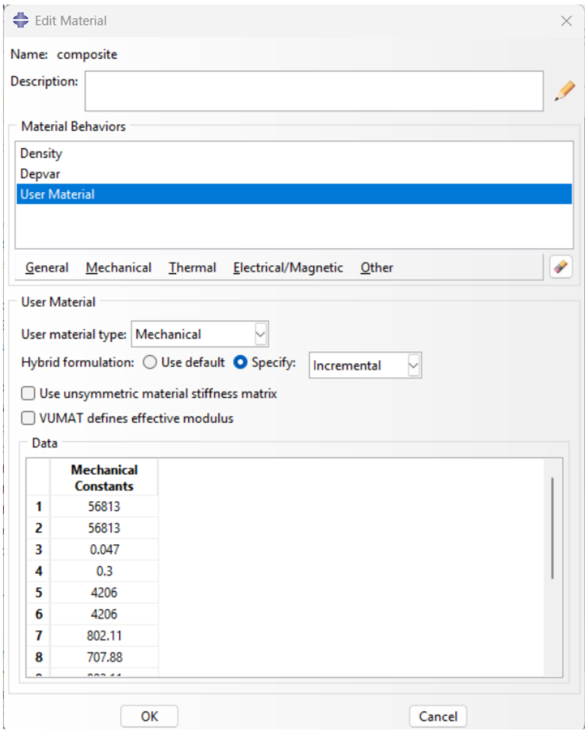

(a)

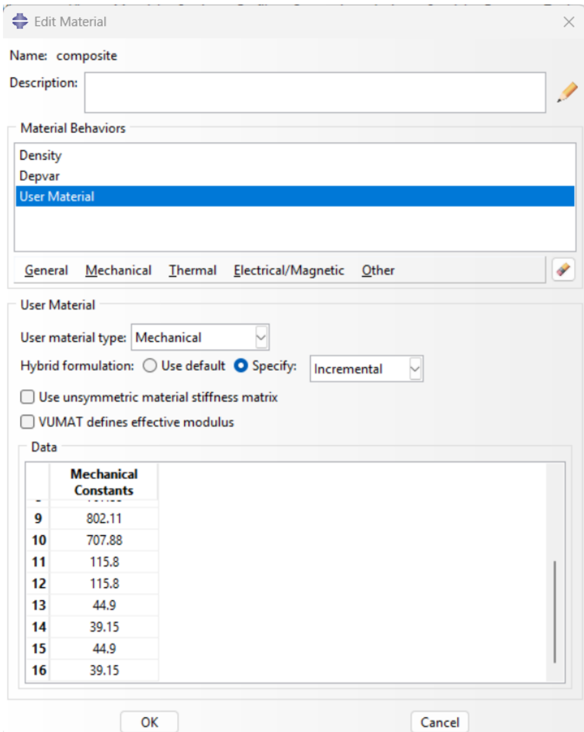

(b)

Figure 4.5: Mechanical constants input.

It is crucial that the 16 mechanical constants are entered in the exact order expected by the VUMAT subroutine. The full list of input values, along with their physical meaning and units, is provided in Table 4.2. This information was also used to populate the "Mechanical Constants" field in Abaqus.

Table 4.2: Mechanical properties of carbon fabric reinforced epoxy plies [93].

Property	**Unit**	**Value**	**Property**	**Unit**	**Value**
E_1	MPa	56813	E_2	MPa	56813
$\nu_{12} = \nu_{13}$	–	0.047	ν_{23}	–	0.3
G_{12}	MPa	4206	G_{23}	MPa	4206
X_t	MPa	802.11	X_c	MPa	707.88
Y_t	MPa	802.11	Y_c	MPa	707.88
S_{12}	MPa	115.8	S_{23}	MPa	115.8
G_{ft}	N/mm	44.9	G_{fc}	N/mm	39.15
G_{mt}	N/mm	44.9	G_{mc}	N/mm	39.15
ρ	kg/m^3	1560			

An excerpt of the VUMAT subroutine code showing the read-in order of these properties is included below for clarity, while the complete subroutine is provided in Appendix B.

```
C User defined material properties
C props(1) Young's Modulus E1
C props(2) Young's Modulus E2
C props(3) Poisson's ratio nu12
C props(4) Poisson's ratio nu23
C props(5) Shear modulus G12
C props(6) Shear modulus G23
C props(7) Fibre tensile stress Xt
C props(8) Fibre compressesive stress Xc
C props(9) Tranverse tensile stress mt
C propos(10) Tranverse compressive stress
C props(11) Matrix shear stress 12 S12
C props(12) Matrix shear sress 23 S23
C props(13) Fracture toughness E fibre tension Gft
C props(14) Fracture toughness E fibre compression Gfc
C props(15) Fracture toughness E matrix tension Gmt
C props(16) Fracture toughness E matrix compression GmcC User defined material properties
C props(1) Young's Modulus E1
C props(2) Young's Modulus E2
C props(3) Poisson's ratio nu12
C props(4) Poisson's ratio nu23
```

```
C props(5) Shear modulus G12
C props(6) Shear modulus G23
C props(7) Fibre tensile stress Xt
C props(8) Fibre compressesive stress Xc
C props(9) Tranverse tensile stress mt
C propos(10) Tranverse compressive stress
C props(11) Matrix shear stress 12 S12
C props(12) Matrix shear sress 23 S23
C props(13) Fracture toughness E fibre tension Gft
C props(14) Fracture toughness E fibre compression Gfc
C props(15) Fracture toughness E matrix tension Gmt
C props(16) Fracture toughness E matrix compression Gmc
```

Listing 4.1: Input order of the 16 mechanical constants in the VUMAT.

This ensures that all inputs in the Abaqus interface correspond exactly to the expectations within the code logic. Any mismatch in order may result in incorrect material behaviour or premature numerical divergence.

Each CFRP ply was assigned a solid section with appropriate material properties and local fibre orientation. Orientations were defined using the "Orientation" keyword with two vectors to establish the 1–2–3 coordinate system of each ply. These were then referenced in the "Solid Section" definitions, which linked each element set (Ply-1 to Ply-16) to the corresponding orientation and thickness.

As mentioned in the beginning of this section, the laminate lay-up followed a symmetric stacking sequence of $[45/-45/0/90/45/-45/0/90]_s$, resulting in a total of 16 plies. This was implemented by assigning each ply a unique orientation definition to match the in-plane fibre direction associated with its nominal angle. The stacking sequence and orientation assignments ensure that the model accurately captures the anisotropic and directional nature of the composite material under impact loading.

To simulate delamination between composite plies, a cohesive interface was defined using a traction–separation model. The corresponding material behaviour represents the epoxy adhesive bonding the plies and governs both stiffness and progressive damage across the interface. The properties used, summarised in Table 4.3, were implemented later in the Interaction module (Section 4.1.5) through surface-based cohesive contact definitions.

Table 4.3: Mechanical properties governing stiffness and progressive damage at the carbon fabric/epoxy interface (interlaminar failure) [93].

Property	**Unit**	**Mode I**	**Mode II**	**Mode III**
K_i	N/mm^3	10^6	10^6	10^6
$t_i^{\max}$	MPa	60	79.289	79.289
G_i^C	N/mm	0.9	2.0	2.0

In addition to the CFRP plies, a thin epoxy interface was considered between the ceramic strike face and the first ply of the composite laminate to account for interfacial adhesion. This interface was modelled using surface-based cohesive contact, with mechanical properties defined separately from those of the CFRP–CFRP interfaces. The stiffness, peak traction, and fracture energy values adopted for this region are summarised in Table 4.4, and were based on literature data for CFRP–ceramic bonding with structural epoxy adhesives. It should be noted that these parameters can strongly influence the predicted response, as variations in interfacial strength and toughness directly affect the onset and progression of delamination, as well as the overall ballistic performance of the hybrid system. This was also implemented later in the Interaction module (Section 4.1.5).

Table 4.4: Mechanical properties governing stiffness and progressive damage for the epoxy (interlaminar failure) [93].

Property	**Unit**	**Mode I**	**Mode II**	**Mode III**
K_i	N/mm^3	10^6	10^6	10^6
$t_i^{\max}$	MPa	30	80	80
G_i^C	N/mm	0.52	0.97	0.97

4.1.2.3 Projectile

As an analytical rigid part, the projectile does not require a material definition in Abaqus. Its mechanical behaviour is fully governed by its kinematic constraints, meaning that no elastic or inertial properties need to be assigned within the Property module.

4.1.3 Assembly

The assembly was constructed by positioning all individual parts in their correct spatial configuration. This included the 16 CFRP plies, the ceramic strike face, and the projectile. Each ply was treated as a separate part to allow the assignment of unique material orientations and interface definitions. All parts were assembled without interference, ensuring proper contact between adjacent plies and between the ceramic and composite regions.

The projectile was placed at a standoff distance of 1 mm in front of the target, aligned with the centre of the impact zone. This spacing ensured that the initial contact occurred dynamically during the simulation, allowing proper development of contact forces and stress wave propagation upon impact.

Particular care was taken in the order in which the composite plies were inserted in the assembly, as this sequence directly influences the fibre orientation and the resulting stacking direction of the laminate. Maintaining the correct stacking sequence is essential to ensure the model accurately reflects the intended laminate architecture. An overview of the full assembly configuration is shown in Figure 4.6.

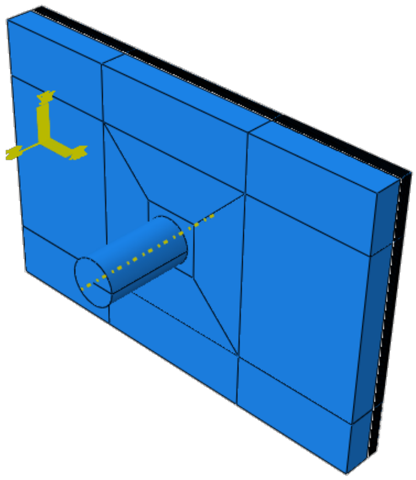

Figure 4.6: Complete assembly of the target and projectile.

4.1.4 Step Definition

The analysis was performed using an explicit dynamic procedure to simulate the high strain-rate response of the target under ballistic impact. A single analysis step, named Step-1, was created using the Dynamic, Explicit procedure in Abaqus. The total step time was set to 0.0001 seconds, ensuring the simulation captured all relevant phases of the impact event, from initial contact to potential perforation or arrest of the projectile.

Time incrementation was defined as automatic, with the stable increment estimator set to "Global" and the "Improved time integration" option enabled. No upper bound was imposed on the maximum time increment, and the time scaling factor remained at 1, ensuring that the physical time evolution was preserved.

Bulk viscosity was applied to stabilise the solution and reduce spurious oscillations during high-frequency wave propagation. The linear and quadratic bulk viscosity coefficients were set to 0.06 and 1.2, respectively. These standard values are commonly used in impact simulations [96].

Field output was requested at regular intervals throughout the analysis, with a frequency of every 50 increments. The output variables included stress, strain, displacement, velocity, reaction forces, and selected state variables such as damage and failure indicators. These were recorded at integration points to ensure sufficient spatial and temporal resolution for post-processing and interpretation of failure mechanisms.

4.1.5 Contact and Interaction Definition

All interactions between components were defined using the "General Contact (Explicit)" algorithm, which is suitable for models involving large deformations, evolving contact, and element deletion. Interaction 1 (`Int-1`) handled all physical contact interfaces between the projectile, ceramic, and composite plies.

The `Int-1` interaction was defined using the General Contact formulation with explicit time integration. This method automatically detects contact between all surfaces in the model, and allows detailed contact behaviour to be specified through individual contact property assignments. The contact behaviour for `Int-1` was defined as follows:

- Normal behaviour: Hard contact, allowing separation after contact and preventing penetration.
- Tangential behaviour: Penalty formulation with isotropic Coulomb friction.

Multiple contact property assignments were applied to capture the different frictional behaviours between interfaces. These were implemented through surface pairings defined using local sets (e.g., Ply1-top, Ply2-bottom, etc.) and manually assigned to specific interaction properties:

- comp-comp: Assigned between each pair of adjacent CFRP plies, from Ply1-top and Ply2-bottom through to Ply15-top and Ply16-bottom. This represents the interlaminar contact between composite plies and includes cohesive behaviour.
- ceramic-comp: Assigned between Ply16-top and ceramic-bottom to define the interface between the ceramic strike face and the composite backing.
- projectil-ceramic: Assigned between ceramic-top and proj-impact-surf (projectile surface set), to govern contact during initial impact.

These contact properties included distinct friction coefficients to realistically simulate the interaction between different materials [93]:

- $\mu = 0.30$ for composite–composite interfaces.
- $\mu = 0.28$ for ceramic–composite interface.
- $\mu = 0.20$ for projectile–ceramic interface.

The use of explicit contact property assignment allows each contact interface to reflect the correct mechanical behaviour during impact, delamination, and sliding.

This interaction was created in the "Initial" step and propagated to the analysis step (Step-1), ensuring it remained active throughout the simulation. The specific contact interactions between each pair of surfaces were defined manually using individual contact property assignments, as illustrated in Figure 4.7.

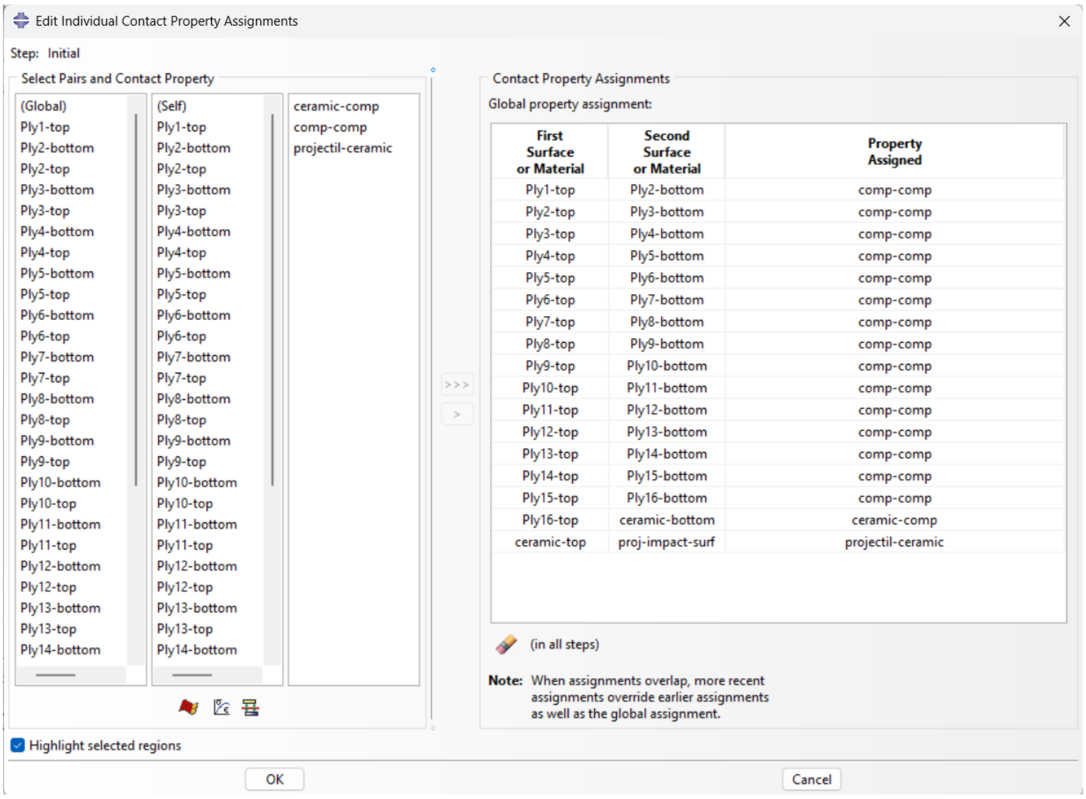

Figure 4.7: Contact property assignments for the projectile, ceramic, and CFRP ply interfaces.

Cohesive behaviour was implemented directly within the contact properties comp-comp and ceramic-comp, both assigned in the general contact interaction `Int-1`. These properties incorporated the cohesive stiffness, traction limits, and fracture energy values defined earlier in Table 4.3 and in Table 4.4.

The contact property comp-comp was assigned to all interfaces between adjacent CFRP plies and included the cohesive parameters governing delamination between composite layers. Likewise, the ceramic-comp property was applied to the interface between the ceramic strike face and the first composite ply, using distinct cohesive values to reflect the ceramic–composite bonding behaviour.

The theoretical background for the interlaminar failure model, including the damage initiation criterion, energy-based evolution law, and mixed-mode interaction, is provided in Section 3.3. All cohesive interactions were active from the start of the analysis and remained valid throughout the simulation. As an example, the configuration of the comp-comp contact property is shown to illustrate how the cohesive behaviour was defined in Abaqus (Figure 4.8). This includes the specification of elastic stiffness, damage initiation using a quadratic nominal stress criterion, and energy-based damage evolution under mixed-mode loading. Although the ceramic-comp property follows the same structure, only the comp-comp interface is presented here for visual clarity, as the parameter assignment process is identical apart from the numerical values.

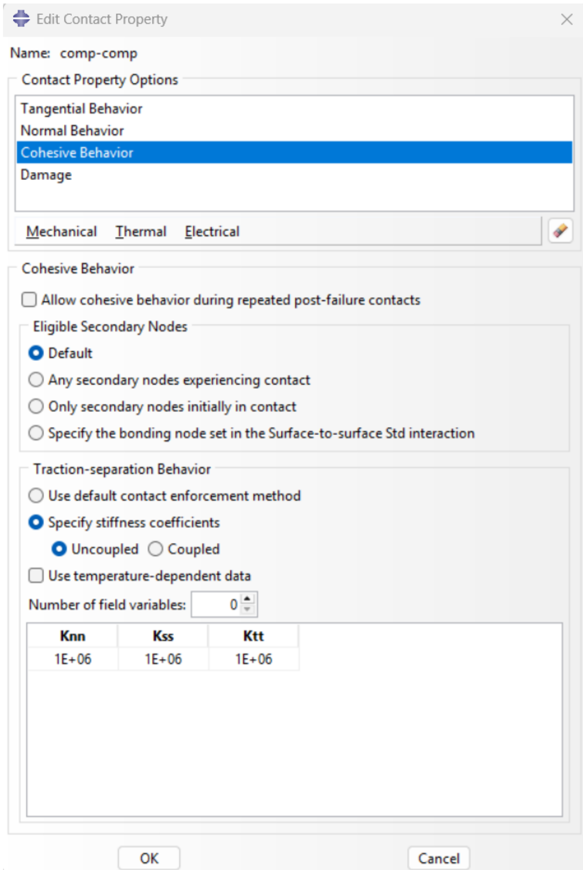

(a)

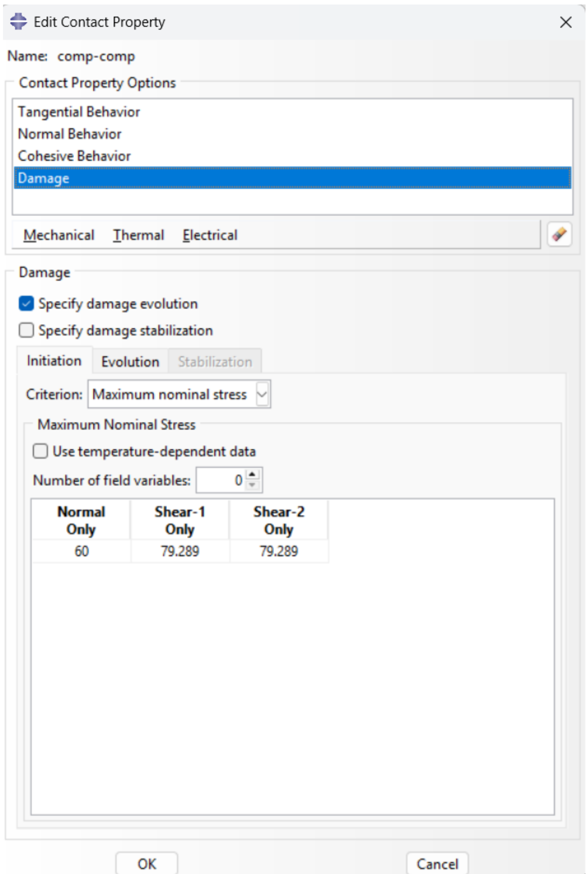

(b)

Figure 4.8: Definition of the comp-comp contact property in Abaqus.

In addition to defining contact interactions, it was necessary to properly constrain the rigid projectile and assign its mass properties. This was accomplished using the "Constraint Manager" within the Interaction module. A new "Rigid Body" constraint was created, with the "Region Type" set as "Analytical Surface", corresponding to the projectile geometry. A dedicated reference point was created to serve as the rigid body's control node, which governs both translational and rotational motion.

To assign inertia, the "Special" menu was used to define a point mass. Specifically, the "Create Inertia" tool was applied with the "Point Mass/Inertia" option selected. The previously defined reference point of the projectile was chosen, and a mass of 11 grams was assigned as an isotropic point mass. This ensures the projectile exhibits realistic inertial response during the impact, despite being defined as an analytical rigid body.

4.1.6 Boundary and Initial Conditions

All load and boundary conditions were defined in the Initial step to ensure they were applied before the dynamic response began. These included velocity input for the projectile and fixed constraints for the target boundaries.

The initial condition was applied as a predefined velocity to the rigid projectile's reference point. The velocity vector was aligned normal to the target plate surface, in the direction of impact. Two separate simulations were performed, each corresponding to different projectile velocities: one with 400 m/s and another with 600 m/s. These values were selected to replicate distinct experimental test conditions and to evaluate the velocity-dependent response of the target structure. Furthermore, it is worth noting that military certification standards typically prescribe ballistic qualification tests within a velocity range of approximately 400 m/s to 800 m/s, as mentioned in Section 2.2.2. The values adopted in this work therefore fall within the required interval, ensuring consistency with established defence testing protocols.

Since the projectile was modelled as a rigid body, assigning velocity at its reference point ensured that the entire geometry moved as a single unit without deformation. This method also preserved kinematic consistency during contact interactions with the target. To constrain the projectile motion, the reference point was fixed in all translational and rotational degrees of freedom except along the impact direction, allowing purely axial movement toward the target.

To replicate the experimental fixture, the back and lateral edges of the target plate were constrained using "Encastre" boundary conditions. These were applied to sets corresponding to the rear face and side edges of the composite laminate and ceramic layer. The constraints prevented displacement and rotation in all directions, effectively simulating clamped support and ensuring stability during impact.

These constraints were carefully chosen to avoid over-constraining the model while sufficiently replicating the support conditions observed in the physical test setup. A visual representation of the applied boundary conditions will be included below to facilitate understanding.

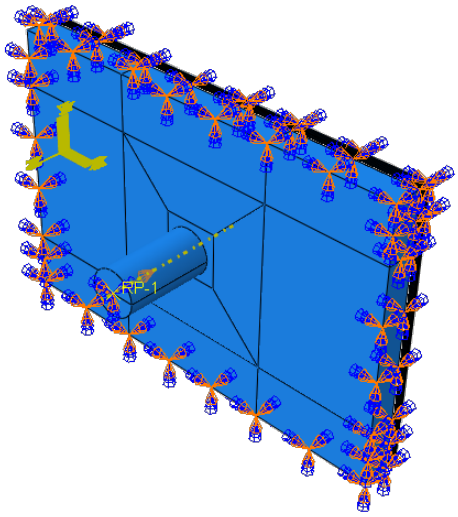

Figure 4.9: Boundary conditions applied to the target and projectile..

4.1.7 Mesh Definition

Accurate mesh definition is critical in high-velocity impact simulations, especially when modelling composite structures subject to stress wave propagation and complex failure modes. In such scenarios, the element size must be carefully chosen to ensure that the numerical model captures the high-frequency content generated during the projectile–target interaction. Additionally, proper mesh refinement is essential near the impact zone, where strong gradients in stress, strain, and damage are expected to develop.

The target was meshed using linear 8-node brick elements with reduced integration (C3D8R). This element type was deliberately selected to follow the modelling strategy proposed by Goda et al. [93]. Its use provides a balance between computational efficiency and accuracy, particularly in explicit analyses involving large deformations, progressive damage, and element deletion. Reduced integration helps mitigate artificial stiffening and decreases numerical cost, while the explicit solver manages hourglass control internally.

To further optimise mesh quality, structured hexahedral meshing was applied throughout. In the direction of projectile travel, mesh biasing was employed to increase refinement towards the impact zone. This improves the accuracy of contact detection and stress transmission during initial impact and through-thickness wave propagation. The transition between fine and coarse regions was smoothed to avoid abrupt changes in element size, which could otherwise induce numerical instabilities.

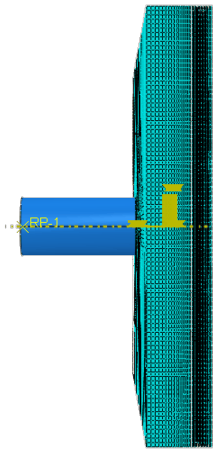

Figure 4.10: Mesh showing local refinement along the impact axis.

The final mesh consisted of:

- Total number of nodes: 1098550.
- Total number of elements: 716760.
- Element type: C3D8R (linear hexahedral elements with reduced integration).

The selection of the element size was guided by wave propagation theory, as detailed in the following subsection.

4.1.7.1 Mesh Size Selection for Stress Wave Resolution

The finite element mesh must be sufficiently refined to resolve stress wave propagation phenomena resulting from high-velocity impact. In explicit dynamic analysis, numerical stability and solution accuracy depend directly on the relationship between element size and the characteristic wavelength of the highest frequency content in the simulation. The theoretical background and governing expressions for the stable time increment and wave-based mesh refinement were presented in Section 2.5.1.

To ensure that the mesh can accurately capture the passage of dilatational waves, the maximum allowable element size was determined using the criterion:

$$L_e \leq \frac{\lambda_{\text{min}}}{n}, \tag{4.1}$$

where $\lambda_{\text{min}} = c_d / f_{\text{max}}$ and n is a safety factor typically set to 10.

Since the analysed target is a hybrid system composed of a 10 mm ceramic strike face bonded to a 4.8 mm CFRP backing, an effective set of properties was calculated to represent the overall laminate in terms of wave propagation. The density was determined as a thickness-weighted average:

$$\rho_{\text{eff}} = \frac{\rho_{\text{cer}} \cdot t_{\text{cer}} + \rho_{\text{CFRP}} \cdot t_{\text{CFRP}}}{t_{\text{cer}} + t_{\text{CFRP}}}, \tag{4.2}$$

where $\rho_{\text{cer}} = 3800\ \text{kg/m}^3$ and $\rho_{\text{CFRP}} = 1560\ \text{kg/m}^3$ are the respective material densities, and $t_{\text{cer}} = 10$ mm and $t_{\text{CFRP}} = 4.8$ mm are their thicknesses. Substituting these values yields:

$$\rho_{\text{eff}} = \frac{3800 \times 10 + 1560 \times 4.8}{10 + 4.8} \approx 3100\ \text{kg/m}^3. \tag{4.3}$$

For consistency, the elastic properties used in the wave speed calculation were taken as those of the CFRP laminate, since it dominates the in-plane stiffness response, while the ceramic primarily governs the strike face resistance. Using Young's modulus $E = 56813$ MPa and Poisson's ratio $\nu = 0.047$ from Table 4.2, together with the effective density, the dilatational wave speed was computed as:

$$c_d = \sqrt{\frac{E(1-\nu)}{\rho_{\text{eff}}(1+\nu)(1-2\nu)}} \approx 4800\ \text{m/s}. \tag{4.4}$$

The selection of the highest frequency f_{max} was based on the expected temporal characteristics of the ballistic impact event. Given the very short rise times associated with the contact between the projectile and the target, the loading profile contains significant high-frequency components. In the absence of a precise loading history (such as force-time or acceleration data), a conservative estimate of $f_{\text{max}} = 250000$ Hz was adopted, consistent with values reported in the literature for similar high-strain-rate applications [100].

From these values, the minimum wavelength is:

$$\lambda_{\text{min}} = \frac{c_d}{f_{\text{max}}} = \frac{4800}{250\,000} \approx 19.2\ \text{mm}. \tag{4.5}$$

Applying a safety factor of $n = 10$ gives the maximum permissible element size:

$$L_e \leq \frac{19.2\ \text{mm}}{10} = 1.92\ \text{mm}. \tag{4.6}$$

Accordingly, the mesh in the impacted region was generated with elements smaller than 1.92 mm to satisfy both stability and wave resolution requirements. A local mesh refinement strategy was adopted: elements with a characteristic length of approximately 1 mm were used in the surrounding impact zone, while even finer elements (smaller than 1 mm) were employed directly within the projectile contact region. Outside these zones, a gradual coarsening of the mesh was implemented to reduce computational cost, while ensuring that all element sizes remained below the calculated threshold. An overview of the final mesh distribution and refinement zones is shown in Figure 4.11.

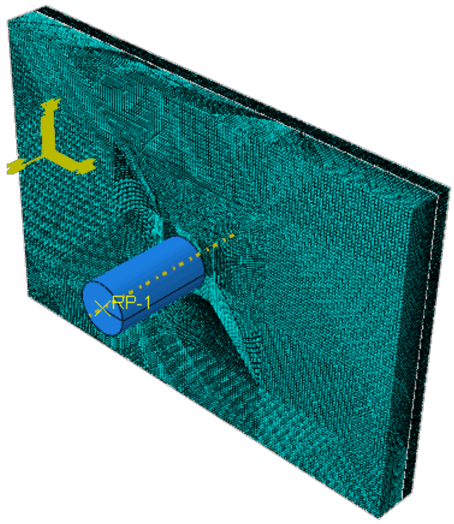

Figure 4.11: Mesh configuration of the full model.

4.2 Results and Discussion

In the study of high-velocity impact on layered targets, the velocity–time history of the projectile is a key indicator of how and when different layers contribute to energy absorption. Differences in the curve shape, duration, and fine-scale features often reveal differences in both the underlying mechanics and the modelling strategy. In the present work, velocity–time data have been obtained for an alumina–CFRP hybrid and are compared against the results reported in the literature [93].

A first striking observation is that the literature curves are plotted only over the very early portion of the event, spanning just a few microseconds, and exhibit a smooth, continuous decay in velocity. Such monotonic, exponential-like behaviour is atypical for a layered ceramic–composite target, where the transition between the ceramic strike face and the CFRP backing usually produces an observable change in the deceleration rate. The absence of any inflection or plateau raises questions as to whether the smoothness is physical or the result of numerical or post-processing effects. The short plotting window also prevents any assessment of later-stage mechanisms such as progressive delamination, fibre pull-in, or secondary wave reflections within the CFRP.

In contrast, the present results span the full interaction time, up to approximately 200 microseconds for the 400 m/s case. Both models predict complete projectile arrest for this velocity, with the histories ending at zero velocity. For the 600 m/s case, both predict residual velocity after perforation, although the rate of deceleration is markedly different. The present results show a sharper initial drop and more fluctuation thereafter, while the literature curve remains smooth throughout.

Several modelling choices contribute to these disparities. A critical factor is mesh density and its interaction with the element formulation. Both studies use first-order solid elements, which do not capture transverse shear accurately unless the mesh is sufficiently fine through the thickness. This is important because transverse shear dominates in the CFRP backing after the ceramic has failed. In the present model, the outer regions of the target are meshed at 1 mm, the intermediate regions are further refined, and the impact zone uses elements smaller than 1 mm. According to the wavelength criterion in Equation 4.1.7.1, this configuration resolves around two wavelengths of the highest frequency of interest. The literature model employs a uniform element length of 1.25 mm across the entire target, resolving only about one wavelength. Under-resolving stress waves not only smooths high-frequency oscillations but also delays or averages abrupt stiffness losses, yielding a more gradual deceleration curve. The absence of any local refinement in their model amplifies this effect.

Another difference lies in the representation of the CFRP backing. In the present work, the CFRP was modelled with explicit ply-level orthotropy, capturing differences between $0°$ and $90°$ plies in stiffness, strength, and failure strain. The literature states only that an 8H satin weave carbon fabric was used in manufacturing, without specifying how it was modelled numerically. It is therefore unclear whether ply-level orthotropy was represented or whether a homogenised or quasi-isotropic equivalent was assumed. Without this information, it is not possible to determine if directional effects were preserved, which could explain the smoother and more uniform deceleration observed in their results.

It must also be acknowledged that the present model is not identical to that in the literature, even where nominally similar parameters were used. The authors of the literature study did not provide all the modelling details, which leaves scope for differences in the implementation of contact enforcement, cohesive damage damping, through-thickness integration points, element deletion criteria, and projectile modelling. Other potential contributors include variations in mass-scaling strategy, bulk-viscosity settings, and damage-stabilisation viscosity, any of which can influence the shape and duration of the deceleration.

Overall, the differences between the two sets of results can be attributed to a combination of variations in mesh resolution, element formulation, material representation, and post-processing approach. These factors have a significant impact on the fidelity with which layer transitions, shear-dominated deformation, and localised failure events are captured, and they naturally lead to differences in the form of the velocity–time histories obtained for layered ceramic–composite systems.

These observations and considerations are illustrated in Figure 4.12 and Figure 4.13, which present the projectile velocity–time histories from the literature and from the present work, respectively, for impact velocities of 400 m/s and 600 m/s.

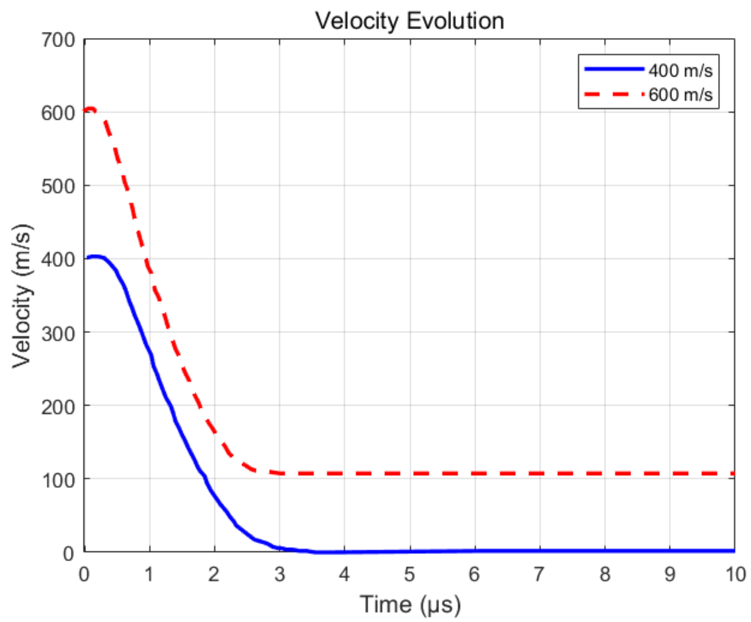

Figure 4.12: Projectile velocity–time histories for 400 m/s and 600 m/s impact velocities (Adapted from [93]).

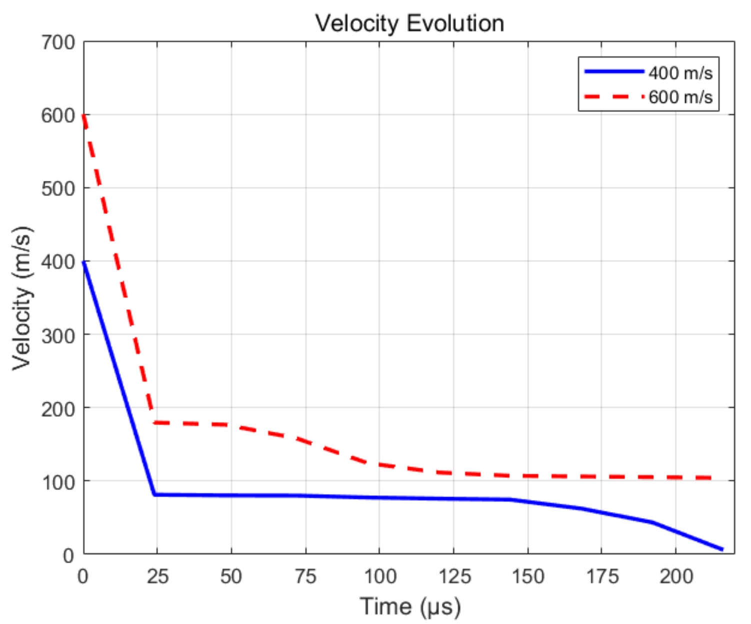

Figure 4.13: Projectile velocity–time histories for 400 m/s and 600 m/s impact velocities, present study.

Goda et al. [93] do not report absorbed energy histories at 400 m/s and 600 m/s for directly comparable targets, which prevents a like for like quantitative comparison with published data.

The absorbed energy in Figure 4.14 was obtained from the projectile velocity records using the loss of kinetic energy:

$$E_{\text{abs}}(t) = \tfrac{1}{2}m_p\left(v_i^2 - v(t)^2\right),$$

where m_p is the projectile mass, v_i is the impact velocity, and $v(t)$ is the instantaneous projectile velocity.

For 400 m/s, the curve increases rapidly during the first 20 to 30 μs and then approaches a stable plateau of approximately 900 J. This behaviour indicates complete arrest of the projectile and therefore full transfer of its initial kinetic energy to the target.

For 600 m/s, the absorbed energy rises more steeply, reaching about 1800 J by roughly 25 μs, and continues to increase without settling on a clear plateau within the simulated time window. This is consistent with perforation, since the projectile exits the target with a residual velocity and not all of the initial kinetic energy is absorbed.

These results reflect the velocity dependence of the ceramic and CFRP system. At 400 m/s, the incident energy is dissipated through fragmentation of the ceramic strike face, matrix dominated mechanisms and fibre failure in the CFRP plies, together with frictional and contact work as debris is arrested. Once the projectile stops, only secondary damage processes continue, hence the near constant plateau. At 600 m/s, higher strain rate loading accelerates damage evolution and favours brittle fracture and fibre pull out, but the interaction time is insufficient for the target to dissipate the full kinetic energy before exit. The continued rise of the absorbed energy curve and the absence of a plateau therefore capture the incomplete energy transfer associated with the residual projectile velocity.

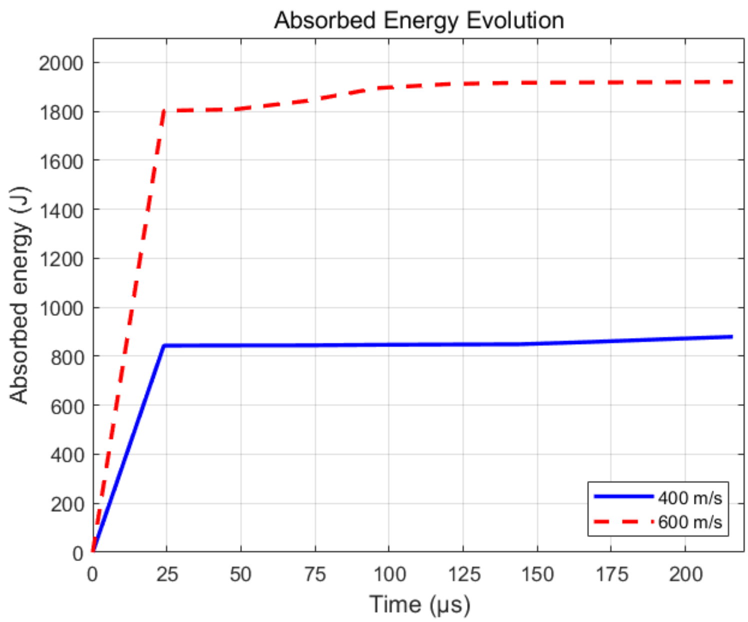

Figure 4.14: Absorbed energy–time histories for CFRP laminates impacted at 400 m/s and 600 m/s.

To complement the velocity–time histories and provide a clearer visual interpretation of the events described above, selected frames from the Abaqus simulation are presented for both the 400 m/s and 600 m/s impact cases. These snapshots illustrate the projectile–target interaction and the progressive damage in the alumina-CFRP hybrid over time. For each velocity, four time instants were chosen:

- $t = 0$ μs, corresponding to the first recorded snapshot, where the projectile is located approximately 1 mm away from the target surface, just prior to impact,
- $t = 72$ μs, showing the onset of fracture in the alumina strike face,
- $t = 168$ μs, showing the stage where the response is dominated by the CFRP backing, with significant delamination,
- $t = 216$ μs, which in the 400 m/s case corresponds to complete projectile arrest, and in the 600 m/s case corresponds to the moment where perforation occurs and the projectile exits with a residual velocity.

These images allow the correlation of specific features in the velocity-time curves, such as sharp drops in velocity or oscillations, with the underlying physical mechanisms, including ceramic fracture, energy absorption by the CFRP backing, delamination, and, in the higher velocity case, perforation.

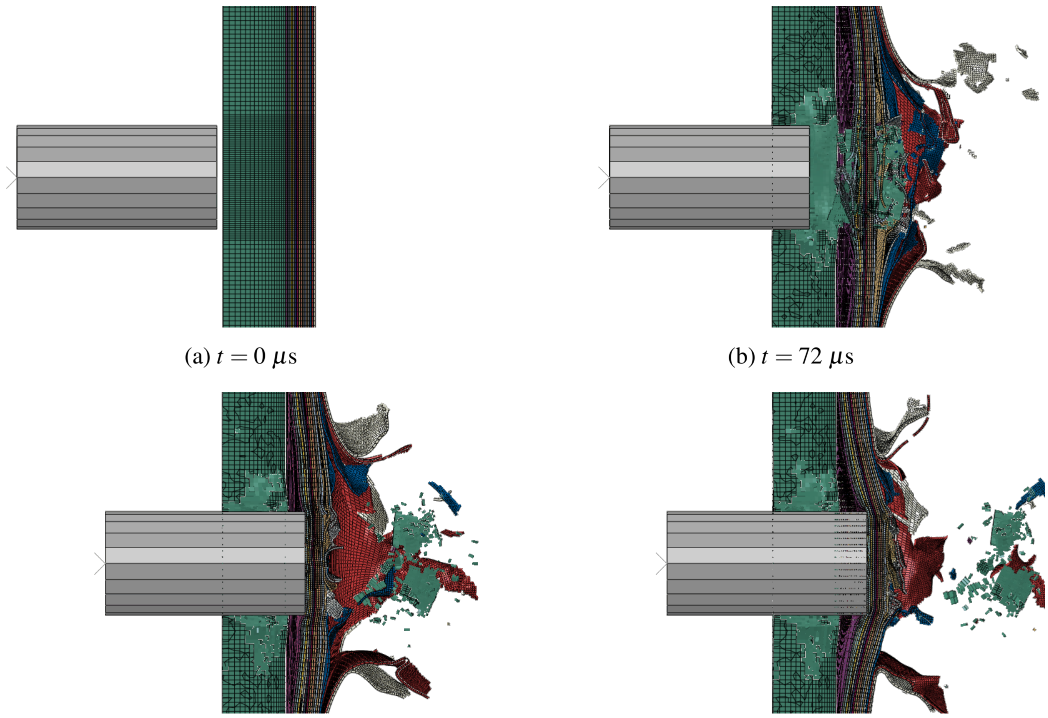

(a) $t = 0$ μs (b) $t = 72$ μs

(c) $t = 168$ μs (d) $t = 216$ μs

Figure 4.15: Evolution of damage/displacement in the alumina–CFRP hybrid target for an impact velocity of 400 m/s.

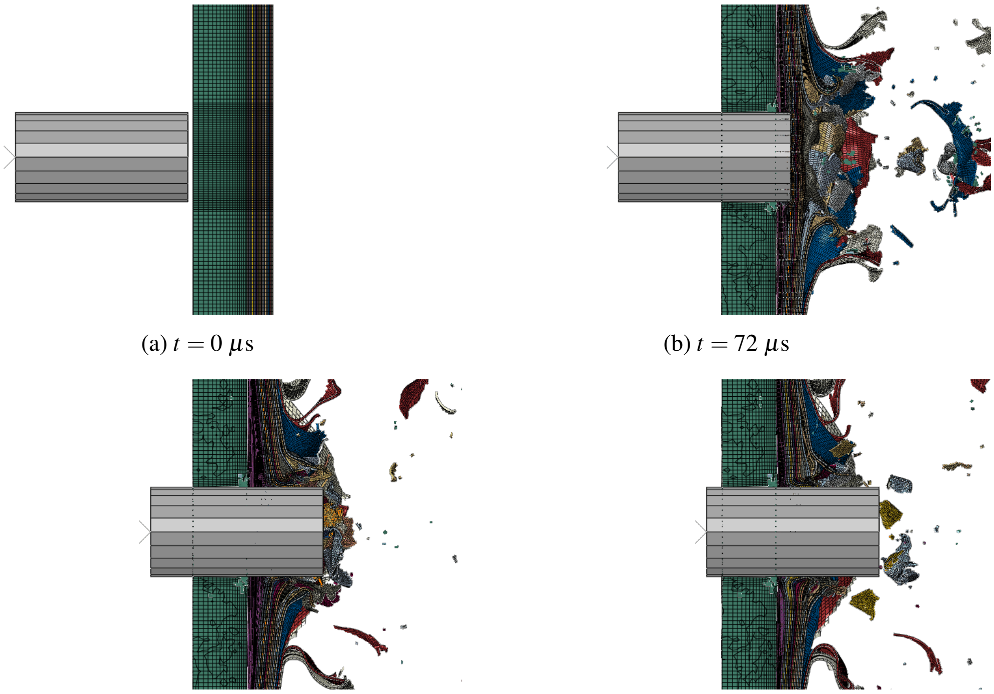

(a) $t = 0$ μs (b) $t = 72$ μs

(c) $t = 168$ μs (d) $t = 216$ μs

Figure 4.16: Evolution of damage/displacement in the alumina–CFRP hybrid target for an impact velocity of 600 m/s.

4.2.1 Computational Resources

All numerical simulations presented in this work were performed on a dedicated workstation kindly provided by Professor Marco Parente. This system was specifically configured for high-performance numerical computations and served as the primary platform for executing the Abaqus/Explicit simulations of ballistic impact.

The workstation is designed to handle computationally demanding finite element models, offering a balance of processing power, memory capacity, and graphical acceleration that ensures efficient solution of large-scale problems. In the context of this dissertation, it was employed to simulate highly nonlinear events involving complex material behaviour, progressive damage, and extensive contact interactions, all of which impose considerable requirements on hardware performance.

The system specifications are summarised in Table 4.5. The combination of dual AMD EPYC processors, large-capacity ECC memory, and a high-performance professional GPU enables efficient execution of explicit dynamic simulations, while the inclusion of a secondary GPU and multiple storage devices provides additional flexibility for data handling and visualisation.

Table 4.5: Technical specifications of the workstation used for Abaqus simulations.

Component	Specification
Processor (CPU)	2 × AMD EPYC Milan 7513, 32 cores / 64 threads, 2.6 GHz
Threads	128 threads
Memory (RAM)	128 GB DDR4 3200 MHz ECC
Primary GPU	NVIDIA PNY Quadro RTX A6000, 48 GB GDDR6
Secondary GPU	ASUS TUF RTX 3060, 12 GB GDDR6
Storage	1 TB NVMe SSD + 12 TB HDD (Seagate Exos, Toshiba)
Operating System	Linux-based / Windows (depending on Abaqus configuration)

This workstation enabled the execution of all case studies with acceptable computational times, thereby ensuring the feasibility of the parametric studies conducted throughout this work. A detailed analysis of the processing times for the different simulations is presented in the following subsection.

4.2.1.1 Simulation Processing Times for the CFRP Case Studies

To complement the hardware description, the computational effort required by the Abaqus/ Explicit models was assessed. Both CFRP simulations (400 m/s and 600 m/s) used the same discretisation (about 7.17×10^5 elements and 1.10×10^6 nodes as depicted in Section 4.1.7) and were executed on the workstation described in Section 4.2.1. The explicit analyses required on the order of 17 hours per run, as summarised in Table 4.6.

Table 4.6: Measured processing times for the CFRP ballistic impact simulations.

Configuration	CPU Time (s)	Wallclock Time (h)
CFRP, 400 m/s	63 478	17.63
CFRP, 600 m/s	61 601	17.11

The runtimes confirm that even with a high-performance workstation, the ballistic impact models demanded several hours to complete. This behaviour is expected because explicit dynamic solvers advance the solution with extremely small stable time increments, which scale with the smallest characteristic element length and the dilatational wave speed of the material. In the present meshes, elements of 1 mm or less were employed around the impact zone, leading to stable increments on the order of 10^{-9} to 10^{-8} s, requiring millions of increments to cover the simulated physical duration of 1.2 ms.

Interestingly, the total runtime was nearly identical between the 400 m/s and 600 m/s cases. This was anticipated, since computational cost is governed primarily by mesh density and total simulated time rather than by the initial impact velocity. Small differences (about 3%) reflect variations in damage initiation, contact activity, and element deletion patterns, which slightly alter the cost per increment but do not affect the number of increments required.

In practical terms, the runtimes obtained demonstrate that the workstation was adequate for the present CFRP case studies, as each simulation could be completed within a single day. More complex configurations would naturally increase computational demands, potentially requiring HPC resources.

Chapter 5

Case Study on High-Velocity Ballistic Impacts with UHMWPE Laminates

As discussed previously in Section 2.3.1, UHMWPE has gained prominence in ballistic protection due to its exceptional strength-to-weight ratio, viscoelastic deformation capacity, and superior ability to absorb and dissipate impact energy. In hybrid systems, UHMWPE layers are typically employed as backing materials to complement harder strike faces, providing enhanced energy absorption and mitigating backface deformation. Building on these insights, the present chapter extends the investigation from the CFRP-based case study (Chapter 4) to a configuration where the composite backing was replaced entirely by UHMWPE laminates, allowing direct assessment of their performance under identical ballistic loading conditions.

The transition from CFRP to UHMWPE required several modifications to the numerical model in Abaqus/Explicit, particularly in terms of material definition, interlaminar interactions, and contact treatment. These adjustments were implemented to accurately reflect the manufacturing characteristics of UHMWPE laminates and their distinctive deformation and failure mechanisms.

5.1 Model Adaptations for UHMWPE Laminates

The most fundamental change concerned the redefinition of the composite material properties while retaining the same VUMAT framework used in the CFRP configuration. In the CFRP case, the plies were governed by a user-defined constitutive model that handled orthotropic elasticity, mode-specific strength limits, and progressive damage. For the UHMWPE configuration, this framework was preserved to maintain a consistent failure-tracking and output pipeline, only the numerical values of the mechanical constants were replaced with those of UHMWPE. Concretely, in the Abaqus "Material Manager" the entries under "Density", "Depvar", and "Mechanical Constants" were updated to the UHMWPE set reported in Table 5.1, keeping the exact properties order required by the subroutine (Appendix B). In this way, the VUMAT continues to drive the elastic response and progressive damage, now parameterised for UHMWPE's orthotropy and strength/toughness levels.

Table 5.1: Mechanical properties of UHMWPE plies [101], [102].

Property	**Unit**	**Value**	**Property**	**Unit**	**Value**
E_1	MPa	25000	E_2	MPa	25000
ν_{12}	–	0.006	ν_{23}	–	0.06
G_{12}	MPa	3000	G_{23}	MPa	15
X_t	MPa	3000	X_c	MPa	2000
Y_t	MPa	3000	Y_c	MPa	2000
S_{12}	MPa	700	S_{23}	MPa	900
G_{ft}	N/mm	0.79	G_{fc}	N/mm	0.03
G_{mt}	N/mm	0.00146	G_{mc}	N/mm	0.00146
ρ	kg/m^3	970			

A second major adaptation related to the treatment of interlaminar interfaces. In the CFRP model, each ply was separated by a thin epoxy layer, represented numerically by cohesive contact formulations. This was essential to simulate delamination, a dominant failure mode in brittle carbon–epoxy laminates. However, UHMWPE laminates are typically produced by hot pressing, during which plies consolidate under elevated temperature and pressure without requiring adhesive bonding [72]. The interfacial adhesion is therefore intrinsic to the manufacturing process rather than provided by a separate epoxy matrix. To reflect this, all cohesive definitions between adjacent plies were removed from the model. Instead, tie constraints were introduced to directly bond successive ply surfaces, effectively enforcing full kinematic compatibility between layers. This adjustment ensures that the laminate behaves as a consolidated UHMWPE block, without artificial weakening due to delamination, thereby more accurately representing the physical characteristics of hot-pressed UHMWPE panels.

The replacement of cohesive definitions with tie constraints also had implications for the frictional interactions in the model. In the CFRP case study, friction coefficients were defined between neighbouring plies to allow relative sliding once cohesive damage initiated, as well as to represent shear interactions at the ceramic–composite interface. With

UHMWPE laminates, however, the tied interfaces removed the need for intralaminar friction, since no ply separation or sliding is expected in practice. Accordingly, all ply-to-ply friction coefficients were omitted. Nevertheless, the frictional contact between the projectile and the laminate surface was retained, since sliding and shear interactions at the point of impact remain physically relevant. This ensures that the projectile–target interaction captures both normal penetration resistance and tangential energy dissipation, while the interior of the laminate is treated as a fully bonded monolithic structure.

5.1.1 Mesh Size Selection for Stress Wave Resolution

The approach adopted to determine the mesh size for the ceramic–UHMWPE configuration followed the same procedure as described previously for the ceramic–CFRP case (Section 4.1.7.1). In explicit dynamic analysis, numerical stability and solution accuracy depend directly on the relationship between element size and the characteristic wavelength of the highest frequency content in the simulation.

For the ceramic–UHMWPE target, an effective density was calculated as a thickness-weighted average of the constituent layers, namely 10 mm of ceramic ($\rho_{\text{cer}} = 3800$ kg/m^3) and 4.8 mm of UHMWPE ($\rho_{\text{UHMWPE}} = 970$ kg/m^3):

$$\rho_{\text{eff}} = \frac{\rho_{\text{cer}} t_{\text{cer}} + \rho_{\text{UHMWPE}} t_{\text{UHMWPE}}}{t_{\text{cer}} + t_{\text{UHMWPE}}} = \frac{3800 \times 10 + 970 \times 4.8}{10 + 4.8} \approx 2882 \text{ kg/m}^3. \tag{5.1}$$

The in-plane elastic properties were taken from the UHMWPE laminate (Table 5.1), with $E = 25000$ MPa and $\nu = 0.06$. Using these values, the dilatational wave speed is:

$$c_d = \sqrt{\frac{E(1-\nu)}{\rho_{\text{eff}}(1+\nu)(1-2\nu)}} \approx 2957 \text{ m/s}. \tag{5.2}$$

As in the CFRP analysis, a conservative highest frequency of $f_{\max} = 250000$ Hz was adopted [100], giving:

$$\lambda_{\min} = \frac{c_d}{f_{\max}} = \frac{2957}{250000} \approx 11.8 \text{ mm}. \tag{5.3}$$

Applying the safety factor $n = 10$ yields a maximum allowable element size of:

$$L_e \leq \frac{11.8 \text{ mm}}{10} = 1.18 \text{ mm}. \tag{5.4}$$

This requirement is of the same order of magnitude as the one obtained previously for the ceramic–CFRP configuration ($L_e \leq 1.92$ mm, see Section 4.1.7.1). Since the CFRP case study already employed a refined mesh with characteristic element sizes of approximately 1 mm in the impact zone and even smaller values at the contact surface, the same mesh strategy was retained for the UHMWPE configuration. The existing refinement was sufficient to satisfy the more stringent UHMWPE-based limit, ensuring both stability and accuracy.

By keeping the mesh unchanged, the two case studies remain directly comparable, and the results can be attributed solely to the change in material behaviour rather than numerical artefacts introduced by mesh differences.

5.2 Results and Discussion

Figure 5.1 presents the projectile velocity–time histories for UHMWPE at 400 m/s and 600 m/s. The curves are shown at two different temporal scales. Firstly, the full simulation up to 220 μs (Figure 5.1a) and, secondly, a zoom into the first 25 μs (Figure 5.1b).

In the full-time plot (Figure 5.1a), both cases display a sharp reduction in velocity immediately after impact, confirming the efficient transfer of kinetic energy into the laminate. Importantly, in both simulations the projectile was ultimately arrested inside the target.

For the 400 m/s case, the projectile decelerates rapidly in the first microseconds and then continues to slow more gradually until full arrest at approximately 216 μs. The velocity curve remains relatively smooth after the initial drop, reflecting progressive energy absorption through fibre stretching, delamination, and matrix cracking. This behaviour is consistent with the development of back coning, where tensile stresses at the rear surface promote a cone-shaped bulge. The longer interaction time allows stresses to redistribute, resulting in a more pronounced back cone.

At 600 m/s, the curve exhibits a steeper initial drop followed by oscillations. The higher energy and shorter interaction time trigger a more abrupt penetration process, governed by shear plugging and localised fragmentation rather than gradual deformation. As a result, back coning is less pronounced and the deformation concentrates along the projectile path. The projectile comes to rest earlier, around 120–130 μs, but due to elastic recovery and inertial rebound it briefly acquires a small backward velocity before settling inside the target. Because Abaqus output used the velocity magnitude, this rebound appears in the graph as the curve reaching zero and then rising again. In reality, it corresponds to a small negative velocity in the impact direction, not a second forward acceleration.

The short-time plot (Figure 5.1b) isolates the first 25 μs, highlighting the immediate response after impact with the ceramic strike face. In this window, neither projectile is fully arrested. Both experience an abrupt velocity drop as the ceramic fractures. After this, the 600 m/s case flattens at a plateau just above 200 m/s, showing that despite significant energy transfer, the projectile still retains substantial forward speed. The 400 m/s case also drops sharply, but because of its lower initial momentum it stabilises at a much lower level (around 70–80 m/s) within the same time frame.

Taken together, Figures 5.1a and 5.1b highlight the influence of material behaviour on ballistic response. The CFRP laminates studied previously showed shorter interaction times and brittle fracture. In contrast, UHMWPE provides extended interaction times, smoother deceleration at 400 m/s, and rebound at 600 m/s, reflecting its ductility and ability to absorb energy progressively. While CFRP relies on stiffness and strength but fails suddenly, UHMWPE dissipates energy through large deformations, ensuring projectile arrest but at the expense of increased back-face deflection.

Overall, the comparison demonstrates that switching from CFRP to UHMWPE fundamentally changes both the constitutive response and the interaction mechanisms under ballistic impact. These results reinforce experimental evidence that UHMWPE-based systems, although less stiff, are highly effective in dissipating kinetic energy and preventing perforation.

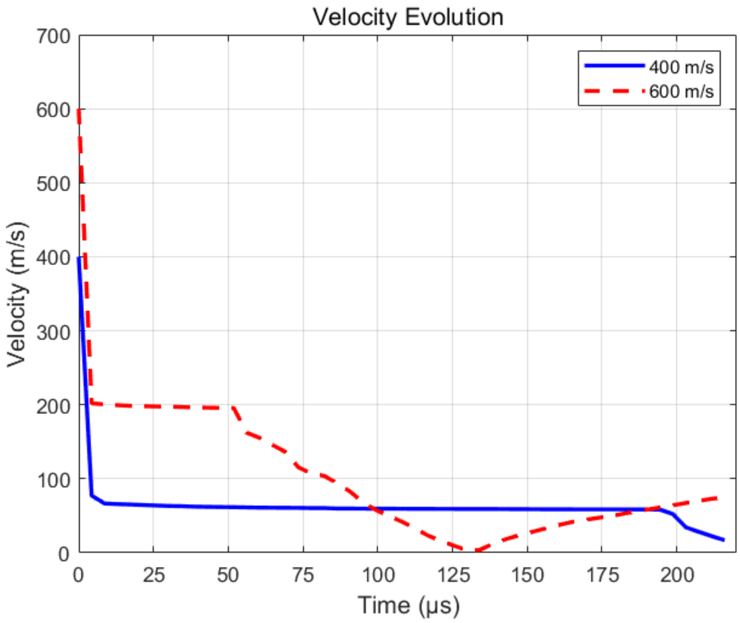

(a) Velocity–time curve up to 220 μs.

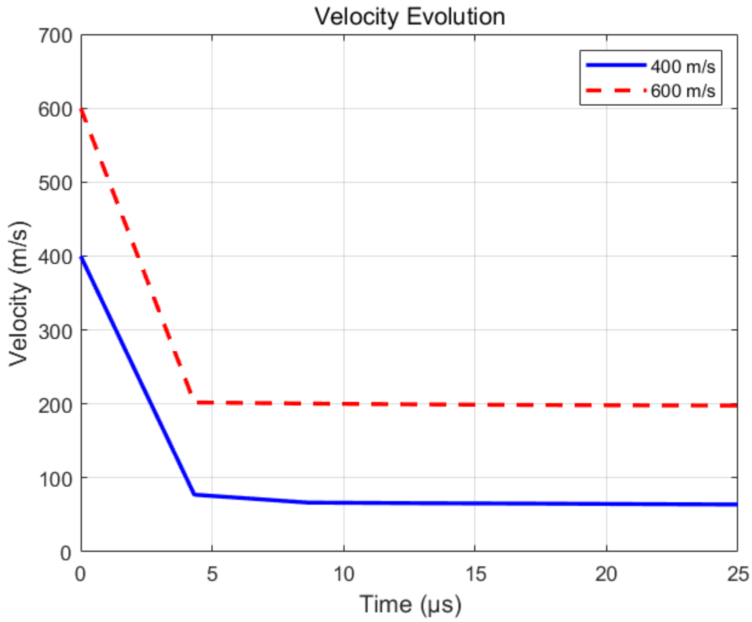

(b) Velocity–time curve up to 25 μs.

Figure 5.1: Projectile velocity–time histories for 400 m/s and 600 m/s impact velocities for UHMWPE.

The absorbed energy histories for UHMWPE at 400 and 600 m/s, shown in Figure 5.2, were computed from the projectile velocity records using the kinetic energy expression introduced earlier in Section 4.2 (Equation 4.2). This is the relation used to generate the updated plot.

For 400 m/s, the curve increases rapidly during the first microseconds and then approaches a stable plateau close to 900 J. The attainment of a plateau indicates full arrest of the projectile, with the incident kinetic energy fully transferred to the target. The small residual growth after the knee is consistent with continuing local damage in the ceramic and progressive deformation of the UHMWPE plies.

For 600 m/s, the absorbed energy rises more steeply and reaches about 1900 to 2000 J by approximately 100 to 150 μs, where it settles on a clear plateau. The presence of this plateau again indicates projectile arrest. The higher terminal level reflects the quadratic dependence of the initial kinetic energy on impact velocity, while the faster early rise is consistent with more intense deformation mechanisms in UHMWPE, including fibre stretching and fibrillation, matrix shear, inter-yarn friction, and pronounced back-face deformation.

Taken together, these results show that the UHMWPE laminate successfully arrests the projectile at both velocities and efficiently dissipates the incident energy. At 400 m/s the energy is absorbed more progressively over a longer duration, whereas at 600 m/s the absorption is faster and larger in magnitude, but still culminates in complete stoppage.

In comparison with the CFRP results of Figure 4.14 and Section 4.2, both targets absorb close to 900 J at 400 m/s since the projectile is arrested in each case. At 600 m/s the behaviours diverge. The UHMWPE target reaches a stable plateau near 1900 to 2000 J, confirming full dissipation of the incident kinetic energy. The CFRP target, by contrast, does not reach a plateau within the simulation window and the projectile exits the target with residual velocity, which indicates incomplete energy transfer. This contrast highlights the superior high-rate energy dissipation capacity of UHMWPE under the conditions studied.

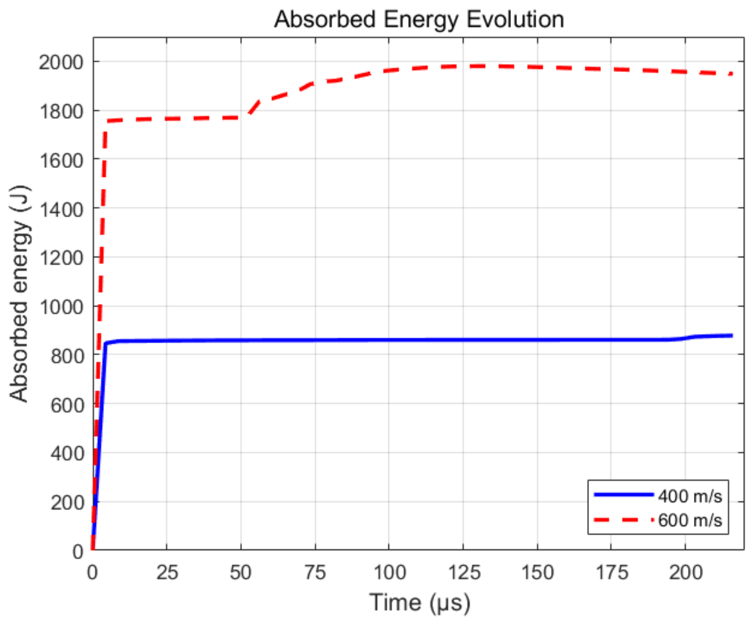

Figure 5.2: Absorbed energy–time histories for UHMWPE laminates impacted at 400 m/s and 600 m/s.

To complement the velocity–time histories and provide a clearer visual interpretation of the events described above, selected frames from the Abaqus simulation are presented for both the 400 m/s and 600 m/s impact cases. These snapshots illustrate the projectile–target interaction and the progressive deformation in the alumina–UHMWPE hybrid over time. For each velocity, four time instants were chosen:

- $t = 0\ \mu$s, corresponding to the first recorded snapshot, where the projectile is located approximately 1 mm away from the target surface, just prior to impact,
- $t = 72\ \mu$s, showing the onset of fracture in the alumina strike face and the first stages of UHMWPE deformation,
- $t = 168\ \mu$s, highlighting the progressive stretching and back-face bulging in the UHMWPE layers,
- $t = 216\ \mu$s, which in the 400 m/s case corresponds to complete projectile arrest and stabilisation of the laminate, and in the 600 m/s case corresponds to the point where the projectile is fully arrested but undergoes a short-lived rebound, gaining a small negative velocity before settling inside the target.

These images allow the correlation of specific features in the velocity–time curves, such as the smooth deceleration in the 400 m/s case or the oscillatory fluctuations in the 600 m/s case, with the underlying physical mechanisms. In particular, they highlight the role of progressive UHMWPE fibre stretching and back coning in the lower velocity regime, and the more abrupt shear-dominated deformation and rebound behaviour at the higher velocity.

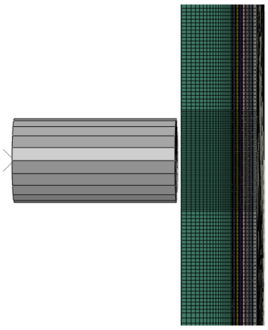

(a) $t = 0\ \mu$s

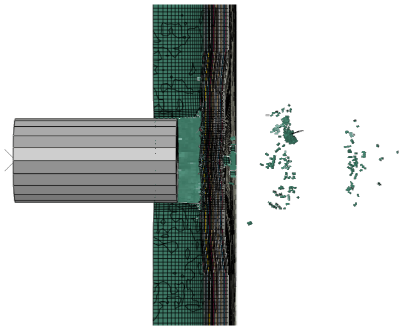

(b) $t = 72\ \mu$s

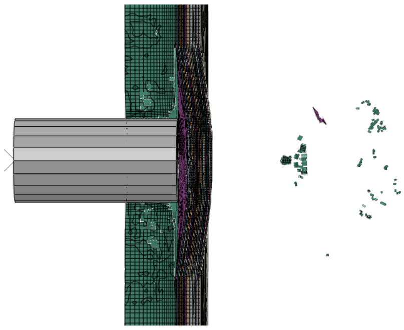

(c) $t = 168\ \mu$s

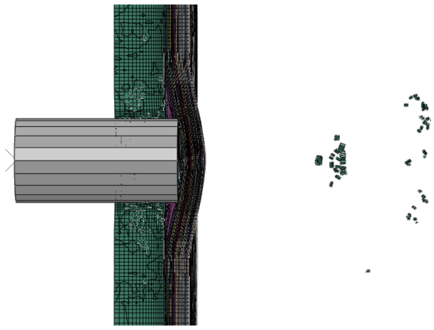

(d) $t = 216\ \mu$s

Figure 5.3: Evolution of damage/displacement in the alumina–UHMWPE hybrid target for an impact velocity of 400 m/s.

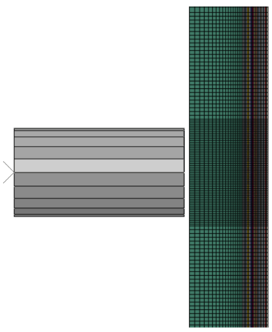

(a) $t = 0\ \mu s$

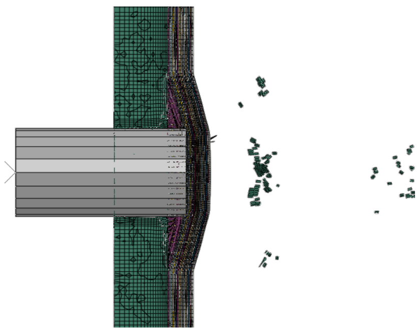

(b) $t = 72\ \mu s$

(c) $t = 168\ \mu s$ (d) $t = 216\ \mu s$

Figure 5.4: Evolution of damage and displacement in the alumina–UHMWPE hybrid target for an impact velocity of 600 m/s: (a) 0–μs, (b) 72–μs, (c) 168–μs, and (d) 216–μs.

5.2.1 Simulation Processing Times for the UHMWPE Case Studies

The ballistic simulations for the UHMWPE configurations were executed on the same workstation described in Section 4.2.1. As with the CFRP models, both impact velocities shared an identical discretisation (approximately 7.17×10^5 elements and 1.10×10^6 nodes as depicted in Section 4.1.7). The processing times are summarised in Table 5.2.

Table 5.2: Measured processing times for the UHMWPE ballistic impact simulations.

Configuration	**CPU Time (s)**	**Wallclock Time (h)**
UHMWPE, 400 m/s	26 500	10.3
UHMWPE, 600 m/s	27 800	10.7

The runtimes obtained for the UHMWPE cases were of similar magnitude, with 400 m/s requiring approximately 10.3 h and 600 m/s about 10.7 h. This small increase at the higher velocity reflects the slightly greater computational cost per increment associated with more severe contact activity, damage initiation, and element deletion. Nevertheless, the similarity of runtimes confirms that explicit simulation cost is dictated primarily by mesh resolution and simulated time rather than by the initial impact velocity itself.

When compared to the CFRP analyses, which required about 17h per run, the UHMWPE simulations finished in roughly 10–11h. This shorter wall clock time does not solely reflect the material system. The UHMWPE cases were run with a higher core count and they also used a shorter simulated step, which reduced the number of increments. Both the increased parallel resources and the problem physics therefore contributed to the faster runs. These figures should be read as wall clock times under different hardware allocations. A normalised measure such as total core hours would provide a fairer basis for comparing computational cost.

Chapter 6

Conclusions

This dissertation investigated the ballistic response of hybrid alumina/composite targets through explicit finite element simulations in Abaqus/Explicit. The ceramic strike face was described using the JH-2 model, while the composite backings were modelled with a 3D Hashin formulation implemented in a VUMAT, combined with cohesive interfaces for CFRP and tied interfaces for the UHMWPE laminate. The methodology successfully reproduced the main features of ceramic fragmentation, composite damage progression, and projectile deceleration, providing a reliable framework for comparing candidate materials.

The results confirmed the distinct impact responses of CFRP and UHMWPE backings. In the case of CFRP, the projectile was arrested at 400 m/s, with the absorbed energy reaching a plateau of approximately 900 J after an interaction time of about 150 µs. At 600 m/s, however, the laminate was perforated, and the absorbed energy exceeded 1800 J without stabilising, reflecting the residual velocity of the projectile. This behaviour highlights the limited failure strain of carbon fibres and the susceptibility of CFRP to unstable damage growth under high-energy impacts.

For the UHMWPE backing, the projectile was stopped at both 400 m/s and 600 m/s. The absorbed energy reached approximately 900 J at 400 m/s and close to 1900 J at 600 m/s, with clear plateaus in both cases, indicating complete energy dissipation. The arrest mechanism was governed by extensive fibre stretching and progressive deformation, which enhanced the laminate's tolerance to impact. Nevertheless, this came at the expense of significantly larger rear face deflections, particularly at 600 m/s, which may be critical for behind-armour safety and integration in structural applications.

Overall, the study demonstrated that CFRP offers effective performance against lower velocity threats with more controlled back-face deformation, whereas UHMWPE provides superior energy absorption and stopping capability at higher velocities, albeit with increased deformation. The developed modelling framework proved capable of capturing these trade-offs and can serve as a valuable tool for the preliminary sizing and optimisation of hybrid ceramic–composite armour systems in aeronautical applications.

In addition, the methodology establishes a sound basis for further development. Future work should expand on this framework by incorporating additional experimental validation, refining interfacial models, and extending the simulations to alternative hybrid configurations and more complex loading conditions. This will provide deeper insight into the governing mechanisms and support the design of next-generation lightweight ballistic protection systems.

6.1 Future Work

The modelling framework is sound and can now be extended in focused ways that raise predictive fidelity and support practical sizing for aircraft use. The items below are short and actionable:

- UHMWPE architecture and layering: Literature reports gains when UHMWPE backings mix woven and unidirectional plies, with about 25% woven and 75% unidirectional performing well. Also benchmark 75% UHMWPE with 25% carbon, which has been reported to stop 7.62 mm threats with lower bulge height and slower deformation [72]. In parallel, assess graded stacks that alternate thin ceramic layers with UHMWPE to promote staged energy dissipation.

- Epoxy and interfaces: Model the epoxy as a 3D solid in a user subroutine that includes strain rate and temperature effects. After failure, allow contact and sliding between layers. Choose a softening law so that the energy dissipated during crack growth matches measured values in opening and in shear. Re run the ballistic cases and compare absorbed energy, residual velocity, delamination, rear face deflection and computational cost.

- Temperature effects and thickness constraints: Include thermal fields so properties evolve during impact, which is important for UHMWPE. Map the influence of ply and ceramic thickness at fixed areal mass and extract simple scaling rules for arrest time, ballistic limit and deformation.

- Experimental validation: Perform controlled ballistic tests that mirror the CFRP and UHMWPE setups. Measure velocity histories, absorbed energy, residual velocity and rear face deflection and document ceramic fragmentation and laminate damage for model refinement.

- Post impact structural integrity and damage tolerance: Assess residual stiffness and strength of non perforated panels under representative service loads. Use numerical follow on loading and compression after impact tests to define acceptance limits aligned with military airworthiness expectations.

- Oblique impact, multiple hits and variability: Evaluate oblique angles and closely spaced hits, which can alter failure paths and increase deformation. Quantify sensitivity to material scatter, interface quality and geometric tolerances and propose safety factors and inspection checkpoints for design and certification.

Bibliography

[1] United Nations, *The 17 goals | sustainable development*, https://sdgs.un.org/goals, Accessed: 2025-08-18, 2015.

[2] P. K. Mallick, *Fiber-Reinforced Composites: Materials, Manufacturing, and Design*, 3rd. Boca Raton, FL: CRC Press, 2007.

[3] V. Giurgiutiu, “Introduction,” in *Stress, Vibration, and Wave Analysis in Aerospace Composites*, Section 1.5.1 discusses the Boeing 787 Dreamliner, Elsevier, 2022, ch. 1, pp. 1–26, ISBN: 9780128133088. [Online]. Available: https://www.sciencedirect.com/science/article/pii/B9780128133088000016.

[4] V. Giurgiutiu, *Structural Health Monitoring of Aerospace Composites*, 1st. Elsevier, 2022, ISBN: 9780323902223.

[5] Airbus, *Fast special edition: A350 xwb*, Accessed March 26, 2025, 2022. [Online]. Available: https://aircraft.airbus.com/sites/g/files/jlcbta126/files/2022-04/FAST_specialA350.pdf.

[6] X. Zhou, Z. Lin, X. Zhang, J. Wei, and G. Li, “Environmental analysis of innovative sustainable composites with potential use in aviation sector—a life cycle assessment review,” *Science China Technological Sciences*, vol. 60, no. 9, pp. 1363–1377, 2017. DOI: 10.1007/s11431-016-9094-y.

[7] M. Pittini and K. I. Kourousis, “Harmonising and standardising military airworthiness in europe: A review of key aspects and achievements,” *The Aeronautical Journal*, vol. 128, no. 1323, pp. 911–927, May 2024. DOI: 10.1017/aer.2023.88. [Online]. Available: https://doi.org/10.1017/aer.2023.88.

[8] M. B. Şenol, “Evaluation and prioritization of technical and operational airworthiness factors for flight safety,” *Aircraft Engineering and Aerospace Technology*, vol. 92, no. 7, pp. 1049–1061, 2020. DOI: 10.1108/AEAT-02-2020-0029.

[9] Horseen. “Benefits of carbon fiber structural reinforcement.” (2025), [Online]. Available: https://www.horseen.com/solution/benefits-carbon-fiber-structural-reinforcement.

[10] V. Madhu, A. Satapathy, M. Krishna, and N. S. Saxena, “Deformation evolution of the ceramic/uhmwpe laminate under ballistic impact,” *International Journal of Impact Engineering*, vol. 178, p. 104 572, 2023. DOI: 10.1016/j.ijimpeng.2023.104572.

[11] V. Šerifi, M. Tarić, D. Jevtić, A. Ristovski, and M. Š. Isović, “Historical development of composite materials,” *Annals of the University of Oradea: Fascicle of Management and Technological Engineering*, vol. XXVII (XVII), no. 3, 2018, Accessed March 20, 2025, ISSN: 1583-0691. DOI: 10.15660/AUOFMTE.2018-3.3392. [Online]. Available: https://www.researchgate.net/publication/338634560_HISTORICAL_DEVELOPMENT_OF_COMPOSITE_MATERIALS.

[12] I. G. Crouch, J. Sandlin, and S. Thomas, “Polymers and fibre-reinforced plastics,” in *The Science of Armour Materials*, I. G. Crouch, Ed., Cambridge: Woodhead Publishing, 2019, ch. 5, pp. 202–268, ISBN: 9780081027165.

[13] A. A. J. M. Peijs, P. Catsman, L. E. Govaert, and P. J. Lemstra, “Hybrid composites based on polyethylene and carbon fibres. part 2: Influence of composition and adhesion level of polyethylene fibres on mechanical properties,” *Composites*, vol. 21, no. 6, pp. 513–521, 1990. DOI: 10.1016/0010-4361(90)90100-Z.

[14] H. van der Werff and U. Heisserer, “High-performance ballistic fibers: Ultra-high molecular weight polyethylene (uhmwpe),” in *Advanced Fibrous Composite Materials for Ballistic Protection*, X. Chen, Ed., Cambridge: Woodhead Publishing, 2016, ch. 3, pp. 71–107, ISBN: 9780081004067.

[15] Y. Zhao, M. Cao, W. P. Lum, V. B. C. Tan, and T. E. Tay, “Interlaminar fracture toughness of hybrid woven carbon-dyneema composites,” *Composites Part A: Applied Science and Manufacturing*, vol. 114, pp. 377–387, 2018. DOI: 10.1016/j.compositesa.2018.09.011.

[16] M. Cao, Y. Zhao, B. H. Gu, B. Z. Sun, and T. E. Tay, “Progressive failure of interwoven carbon-dyneema fabric reinforced hybrid composites,” *Composites Structures*, vol. 211, pp. 175–186, 2019. DOI: 10.1016/j.compstruct.2018.12.035.

[17] S. Taj, M. A. Munawar, and S. Khan, “Natural fiber-reinforced polymer composites,” *Proceedings of the Pakistan Academy of Sciences*, pp. 129–144, 2007.

[18] N. Bouhfid, M. Raji, R. Boujmal, *et al.*, “Modelling of damage processes in biocomposites, fibre-reinforced composites and hybrid composites,” in *Woodhead Publishing Series in Composites Science and Engineering*, Woodhead Publishing, 2019, pp. 57–101. DOI: 10.1016/B978-0-08-102292-4.00004-8.

[19] R. Hsissou, R. Seghiri, Z. Benzekri, M. Hilali, M. Rafik, and A. Elharfi, “Polymer composite materials: A comprehensive review,” *Materials Today: Proceedings*, vol. 27, pp. 2578–2587, 2020. DOI: 10.1016/j.matpr.2020.02.004.

[20] P. M. Cunniff and M. A. Auerbach, “High performance fibrous composites for personal and vehicle armour,” in *Proceedings of the 19th International Symposium on Ballistics*, vol. 2, 1995, pp. 779–788.

[21] H. Khayyam, R. N. Jazar, S. Nunna, *et al.*, "Pan precursor fabrication, applications and thermal stabilization process in carbon fiber production: Experimental and mathematical modelling," *Progress in Materials Science*, vol. 138, p. 101 031, 2023. DOI: 10.1016/j.pmatsci.2023.101031.

[22] S. A. Mirdehghan, *Fibrous Polymeric Composites*. Tehran, Iran: Amirkabir University of Technology (Tehran Polytechnic), 2024.

[23] P. V. Gulgunje, B. A. Newcomb, K. Gupta, H. G. Chae, T. K. Tsotsis, and S. Kumar, "Low-density and high-modulus carbon fibers from polyacrylonitrile with honeycomb structure," *Carbon*, vol. 203, pp. 345–358, 2024. DOI: 10.1016/j.carbon.2024.01.012.

[24] D. Hull and T. W. Clyne, *An Introduction to Composite Materials* (Cambridge Solid State Science Series). Cambridge, UK: Cambridge University Press, 1996, ISBN: 9780521388559.

[25] R. D. S. G. Campilho, *Natural Fiber Composites*. Boca Raton, FL, USA: CRC Press, 2015, ISBN: 9781482239005.

[26] A. K. Rana, A. Mandal, and S. Bandyopadhyay, "Short jute fiber reinforced polypropylene composites: Effect of compatibiliser, impact modifier and fiber loading," *Composites Science and Technology*, vol. 63, no. 6, pp. 801–806, 2003. DOI: 10.1016/S0266-3538(02)00256-2.

[27] T. Gurunathan, S. Mohanty, and S. K. Nayak, "A review of the recent developments in biocomposites based on natural fibres and their application perspectives," *Composites Part A: Applied Science and Manufacturing*, vol. 77, pp. 1–25, 2015. DOI: 10.1016/j.compositesa.2015.06.007.

[28] A. Abbadi, Z. Azari, S. Belouettar, J. Gilgert, and P. Freres, "Modelling the fatigue behaviour of composites honeycomb materials (aluminium/aramide fibre core) using four-point bending tests," *International Journal of Fatigue*, vol. 32, no. 11, pp. 1739–1747, 2010. DOI: 10.1016/j.ijfatigue.2010.04.002.

[29] A. Abbadi, C. Tixier, J. Gilgert, and Z. Azari, "Experimental study on the fatigue behaviour of honeycomb sandwich panels with artificial defects," *Composite Structures*, vol. 120, pp. 394–405, 2015. DOI: 10.1016/j.compstruct.2014.10.020.

[30] S. Bourbigot and X. Flambard, "Heat resistance and flammability of high performance fibres: A review," *Fire and Materials*, vol. 26, no. 4–5, pp. 155–168, 2002. DOI: 10.1002/fam.799.

[31] C. Y. Yue, G. X. Sui, and H. C. Looi, "Effects of heat treatment on the mechanical properties of kevlar-29 fibre," *Composites Science and Technology*, vol. 60, no. 3, pp. 421–427, 2000. DOI: 10.1016/S0266-3538(99)00160-2.

[32] B. L. Deopura and N. V. Padaki, "Synthetic textile fibres: Polyamide, polyester and aramid fibres," in *Textiles and Fashion*, W. Publishing, Ed., Cambridge, UK: Woodhead Publishing, 2015, pp. 97–114.

[33] P. Dharmavarapu and S. R. M.B.S, "Aramid fibre as potential reinforcement for polymer matrix composites: A review," *Emergent Materials*, 2021, Received: 15 May 2021, Accepted: 4 June 2021. DOI: 10.1007/s42247-021-00246-x.

[34] K. K. Chawla, *Composite Materials: Science and Engineering*, 4th. New York, NY, USA: Springer, 2021, ISBN: 9783030515924. DOI: 10.1007/978-3-030-51593-1. [Online]. Available: https://link.springer.com/book/10.1007/978-3-030-51593-1.

[35] P. J. Lemstra and B. J. Lommerts, "Polyethylene vs. para-aramid fibers," *Journal of Advanced Materials*, 2025.

[36] A. K. Sharma, R. Bhandari, A. Aherwar, and R. Rimašauskiene, "Matrix materials used in composites: A comprehensive study," *Materials Today: Proceedings*, vol. 19, pp. 1087–1091, 2019. DOI: 10.1016/j.matpr.2019.11.086.

[37] D. Verma, P. C. Gope, A. Shandilya, A. Gupta, and M. K. Maheshwari, "Coir fibre reinforcement and application in polymer composites: A review," *Journal of Polymer Materials*, vol. 29, no. 4, pp. 567–586, 2012, Received 13 Sept 2012, Revised 15 Oct 2012, Accepted 15 Oct 2012.

[38] F. C. Campbell, "Thermoset resins: The glue that holds the strings together," in *Manufacturing Processes for Advanced Composites*, Elsevier, 2004, pp. 63–101. DOI: 10.1016/b978-185617415-2/50004-6.

[39] H. Madhav, N. Singh, and G. Jaiswar, "Thermoset, bioactive, metal–polymer composites for medical applications," in *Materials for Biomedical Engineering: Thermoset and Thermoplastic Polymers*, Elsevier, Ed., Elsevier, 2019, ch. 4, pp. 105–143. DOI: 10.1016/B978-0-12-816874-5.00004-9.

[40] S. P., "Composites," in *Collection of Engineering Reviews*, ResearchGate, Nov. 2020. [Online]. Available: https://www.researchgate.net/publication/345921909_Composites.

[41] I. G. Crouch, Ed., *The Science of Armour Materials* (Woodhead Publishing in Materials). Amsterdam, Boston, Cambridge, Heidelberg, London, New York, Oxford, Paris, San Diego, San Francisco, Singapore, Sydney, Tokyo: Woodhead Publishing, an imprint of Elsevier, 2016, ISBN: 9780081004067.

[42] G. Brown. "The use of composites in aircraft construction." Accessed March 23, 2025. (2014), [Online]. Available: https://vandaair.com/2014/04/14/the-use-of-composites-in-aircraft-construction/.

[43] P. Lage, *Aeronautic certification*, Personal collection, Lecture slides, Aeronautic Certification, Faculdade de Engenharia da Universidade do Porto, 2024.

[44] E. U. A. S. Agency, *Amc 20-29: Composite aircraft structure*, Accessed March 25, 2025, 2009. [Online]. Available: https://www.easa.europa.eu/en.

[45] Federal Aviation Administration (FAA). "Federal Aviation Administration Official Website." Accessed March 25, 2025. (2024), [Online]. Available: https://www.faa.gov/.

[46] M. S. Loukil, "Experimental and numerical studies of intralaminar cracking in high performance composites," PhD Thesis, Oct. 2013.

[47] X. Zhou, Z. Lin, X. Zhang, J. Wei, and G. Li, "Environmental analysis of innovative sustainable composites with potential use in aviation sector—a life cycle assessment review," *Science China Technological Sciences*, vol. 60, no. 9, pp. 1363–1377, 2017. DOI: 10.1007/s11431-016-9094-y.

[48] SAT Plating. "Composite materials in modern aircraft: Beyond the boeing 787." Accessed March 26, 2025. (n.d.), [Online]. Available: https://www.satplating.com/education/composite-materials-in-modern-aircraft-beyond-the-boeing-787/.

[49] Time. "Exclusive: The making of the u.s. military's new stealth bomber." Accessed March 26, 2025. (2022), [Online]. Available: https://time.com/6238168/b-21-raider-bomber-us-military-exclusive/.

[50] K. Biswas, "Military airworthiness and certification procedures: Global scenario," in *Proceedings of the International Conference on Modern Research in Aerospace Engineering*, S. Singh, P. Raj, and S. Tambe, Eds., Singapore: Springer Singapore, 2018, pp. 315–331.

[51] L. Purton and K. Kourousis, "Military airworthiness management frameworks: A critical review," in *3rd International Symposium on Aircraft Airworthiness, ISAA 2013*, vol. 80, Elsevier, 2014, pp. 545–564. DOI: 10.1016/j.proeng.2014.09.111. [Online]. Available: http://www.sciencedirect.com/science/article/pii/S1877705814014563.

[52] European Defence Agency, MAWA Forum, *European military airworthiness requirement emar m - continuing airworthiness management*, Available at: https://eda.europa.eu/what-we-do/activities/activities-search/military-airworthiness, 2018.

[53] European Defence Agency, *European military airworthiness*, Accessed from official EDA publications, 2013.

[54] European Defence Agency, *European military airworthiness document – recognition (emadr)*, Official publication, 2013.

[55] European Defence Agency, *Introduction to the military airworthiness framework*, Official publication, 2017.

[56] European Defence Agency, *Emar 21 – certification of military aircraft and related products, parts and appliances, and design and production organisation approval*, EMAR Series, 2018a, 2018.

[57] European Defence Agency, *Emar m – continuing airworthiness*, EMAR Series, 2018b, 2018.

[58] UK Ministry of Defence, *Ra 1010 – certification of military aircraft*, Regulatory Article, Defence Safety Authority, 2020.

[59] J. Guo, K. Bai, and L. Jia, "Research on airworthiness management system about military aircraft development," in *The 2nd International Symposium on Aircraft Airworthiness (ISAA 2011)*, vol. 17, Elsevier, 2011, pp. 375–381. DOI: `10.1016/j.proeng.2011.10.043`. [Online]. Available: `https://www.sciencedirect.com/science/article/pii/S1877705811038183`.

[60] U.S. Department of Defense, *Dod instruction 5030.61: Dod airworthiness policy*, A. by William A. LaPlante, Ed., `https://www.esd.whs.mil/DD/`, Effective December 3, 2024. Reissues and cancels DoD Directive 5030.61 (May 24, 2013), 2024.

[61] L. Purton and K. Kourousis, "Military airworthiness management frameworks: A critical review," in *Proceedings of the 3rd International Symposium on Aircraft Airworthiness (ISAA 2013)*, Sir Lawrence Wackett Aerospace Research Centre, RMIT University, Airworthiness Technologies Research Center, Beihang University/N-LAA, Melbourne, Australia, 2013.

[62] J. C. King, "Using model based system engineering to identify safety critical functions in airworthiness certifications," Distribution Statement A: Approved for public release; distribution unlimited, Master's thesis, Air Force Institute of Technology, Air University, Department of Systems Engineering, Management, Graduate School of Engineering, and Management, 2021.

[63] Federal Aviation Administration, *Order 8130.2g: Airworthiness certification of aircraft and related products*, `https://www.faa.gov/documentlibrary/media/order/8130.2g.pdf`, 2017.

[64] Department of the Air Force, *Department of the air force guidance memorandum to department of the air force instruction (dafi) 62-601, "airworthiness"*, By Order of the Secretary of the Air Force. Compliance with this Memorandum is mandatory., 1060 Air Force Pentagon, Washington, DC 20330-1060, Apr. 2025.

[65] U.S. Department of Defense, "Mil-std-662f: V50 ballistic test for armor," Department of Defense, Washington, DC, Test Method Standard MIL-STD-662F, 1997, Superseding MIL-STD-662E, dated 22 January 1987. Issued 18 December 1997.

[66] University of Dayton Research Institute, *Commonly used ballistic testing standards*, `https://udri.udayton.edu`, 2025.

[67] L. Wang, S. Kanesalingam, R. Nayak, and R. Padhye, "Recent trends in ballistic protection," *Textiles and Light Industrial Science and Technology*, vol. 3, pp. 37–47, 2014. [Online]. Available: https://www.researchgate.net/publication/304506225_Recent_Trends_in_Ballistic_Protection.

[68] O. E. İşmal and R. Paul, "Composite textiles in high-performance apparel," in *High-Performance Apparel: Materials, Development, and Applications*, Affiliations: Dokuz Eylül University, İzmir, Turkey; University of Beira Interior, Covilhã, Portugal, Cambridge, UK: Woodhead Publishing, 2020, pp. 145–165.

[69] N. K. Naik, "Ballistic impact behaviour of composites: Analytical formulation," *Composites Part B: Engineering*, vol. 31, no. 8, pp. 763–771, 2000. DOI: 10.1016/S1359-8368(00)00046-7.

[70] M. J. N. Jacobs and J. L. J. van Dingenen, "Ballistic protection mechanisms in personal armour," *Journal of Materials Science*, vol. 36, no. 13, pp. 3137–3142, 2001. DOI: 10.1023/A:1017984402547.

[71] A. K. Bandaru, R. M. O'Higgins, D. K. Kothandan, H. Chouhan, and H. Ma, "Ballistic impact performance of kevlar®/uhmwpe hybrid composite panels with a liquid thermoplastic resin, elium®," *Composites Part B: Engineering*, 2023, Bernal Institute, University of Limerick; Ahmedabad University; Technical University of Denmark. DOI: 10.1016/j.compositesb.2023.110920.

[72] T. S. Reddy, P. R. S. Reddy, and V. Madhu, "Dynamic behaviour of carbon/ultra high molecular weight polyethylene (uhmwpe) hybrid composite laminates under ballistic impact," *Journal of Dynamic Behavior of Materials*, vol. 6, no. 4, pp. 478–492, 2020. DOI: 10.1007/s40870-020-00275-3.

[73] X. Chen, Y. Huang, Z. Chen, and Y. Xu, "Numerical and experimental investigations into ballistic performance of hybrid fabric panels," *International Journal of Impact Engineering*, vol. 70, pp. 22–35, 2014. DOI: 10.1016/j.ijimpeng.2014.02.007.

[74] F. Klocke, T. Beck, S. Hoppe, *et al.*, "Examples of fem application in manufacturing technology," *Journal of Materials Processing Technology*, vol. 120, no. 1-3, pp. 450–457, 2001. DOI: 10.1016/S0924-0136(01)01115-8.

[75] K. Bilisik, M. Syduzzaman, G. Erdogan, and M. Korkmaz, "Advances in ballistic protection," in *Functional and Technical Textiles*, ser. The Textile Institute Book Series, S. Maity, K. Singha, and P. Pandit, Eds., Woodhead Publishing, 2023, pp. 71–139, ISBN: 978-0-323-91593-9. DOI: 10.1016/B978-0-323-91593-9.00023-7. [Online]. Available: https://www.sciencedirect.com/science/article/pii/B9780323915939000237.

[76] Martec. "Ballistic protection for aircraft and helicopters." (2024), [Online]. Available: https://www.martec.it/?page_id=618.

[77] A. SAS. “Armor solutions.” (2024), [Online]. Available: https://amefo.fr/en/defense-en/aircrafts-en/#.

[78] United States Air Force, *A-10c thunderbolt ii*, https://www.af.mil/About-Us/Fact-Sheets/Display/Article/104490/a-10c-thunderbolt-ii/, Accessed: 2025-08-10, 2024.

[79] K. Mizokami, “The warthog’s titanium bathtub cockpit is a heavily armored cocoon,” *The National Interest*, Jul. 2024, Accessed: 2025-08-10. [Online]. Available: https://nationalinterest.org/blog/buzz/10-warthogs-titanium-bathtub-cockpit-heavily-armored-cocoon-211790.

[80] D. Axe. “A-10 pilot’s diary entry from the day she was nearly shot down.” (Feb. 2021), [Online]. Available: https://www.twz.com/a-10-pilots-diary-entry-from-the-day-she-was-nearly-shot-down.

[81] M. F. Ismail, M. T. H. Sultan, A. Hamdan, A. U. M. Shah, and M. Jawaid, “Low velocity impact behaviour and post-impact characteristics of kenaf/glass hybrid composites with various weight ratios,” *Composite Structures*, vol. 214, pp. 406–417, 2019. DOI: 10.1016/j.compstruct.2019.02.019.

[82] S. N. A. Safri, M. T. H. Sultan, N. Yidris, and F. Mustapha, “Low velocity and high velocity impact test on composite materials – a review,” *The International Journal of Engineering and Science (IJES)*, vol. 3, no. 9, pp. 50–60, 2014, ISSN: 2319-1813. [Online]. Available: https://www.researchgate.net/publication/309457007_Low_velocity_and_high_velocity_impact_test_on_composite_materials_-_A_review.

[83] S. Wu and L. Gu, *Introduction to the Explicit Finite Element Method for Nonlinear Transient Dynamics*. John Wiley & Sons, 2012. DOI: 10.1002/9781118382011.

[84] R. Shamey and X. Zhao, “5 - solving dynamic equations in dye transport,” in *Modelling, Simulation and Control of the Dyeing Process*, ser. Woodhead Publishing Series in Textiles, Woodhead Publishing, 2014, pp. 100–113, ISBN: 9780857091338. DOI: 10.1533/9780857097583.100. [Online]. Available: https://www.sciencedirect.com/science/article/pii/B9780857091338500050.

[85] ABAQUS Inc., *Abaqus user’s manual, version 6.6*, 2006.

[86] FEA Solutions. “Implicit vs explicit.” (2025), [Online]. Available: https://fea-solutions.co.uk/implicit-vs-explicit/.

[87] ABAQUS Inc., *Getting started with abaqus: Interactive edition, version 6.5*, 2005.

[88] A. Rocha, “Development of ballistic protection for military aircraft: An investigation on material models with strain rate effects,” Supervisor: Prof. Dr. Volnei Tita, Master’s Thesis, Universidade do Porto, Faculdade de Engenharia, Porto, Portugal, 2024.

[89] P. P. Camanho, “Failure criteria for fibre-reinforced polymer composites,” Faculdade de Engenharia da Universidade do Porto, Departamento de Engenharia Mecânica e Gestão Industrial (DEMEGI), Secção de Mecânica Aplicada, Technical Report, 2002.

[90] Z. Hashin and A. Rotem, “A fatigue failure criterion for fiber reinforced materials,” *Journal of Composite Materials*, vol. 7, no. 4, pp. 448–464, 1973. DOI: 10.1177/002199837300700404.

[91] Z. Hashin, “Fatigue failure criteria for unidirectional fiber composites,” *Journal of Applied Mechanics*, vol. 47, no. 4, pp. 329–334, 1980. DOI: 10.1115/1.3153664.

[92] S. L. J. Millen, A. Murphy, G. Catalanotti, and G. Abdelal, “Coupled thermal–mechanical progressive damage model with strain and heating rate effects for lightning strike damage assessment,” *Applied Composite Materials*, vol. 26, no. 10, pp. 1437–1459, 2019. DOI: 10.1007/s10443-019-09789-z. [Online]. Available: https://doi.org/10.1007/s10443-019-09789-z.

[93] I. Goda and J. Girardot, “Numerical modeling and analysis of the ballistic impact response of ceramic/composite targets and the influence of cohesive material parameters,” *International Journal of Damage Mechanics*, vol. 30, no. 7, pp. 1079–1122, 2021. DOI: 10.1177/1056789521992107. [Online]. Available: https://journals.sagepub.com/doi/10.1177/1056789521992107.

[94] P. P. Camanho and C. G. Dávila, “Mixed-mode decoheion finite elements for the simulation of delamination in composite materials,” NASA Langley Research Center, Hampton, Virginia, Technical Report NASA/TM-2001-211041, 2001, University of Porto, Portugal; Langley Research Center, USA.

[95] D. F. Adams, L. A. Carlsson, and R. B. Pipes, *Experimental Characterization of Advanced Composite Materials*, 3rd. CRC Press, 2003, ISBN: 9780849315923.

[96] Dassault Systèmes. “Abaqus.” Accessed: 2024-07-01. (2024), [Online]. Available: https://www.3ds.com/products/simulia/abaqus.

[97] M. R. D. Miranda, “Assessment of composite fuselage crashworthiness: A virtual testing methodology,” Developed during a research stay at the Aeronautical Structural Design Lab (ASD Lab), UC3M Aerospace Engineering Department, M.S. thesis, Universidade do Porto, Faculdade de Engenharia, Porto, Portugal, Jun. 2023.

[98] G. Guo, S. Alam, and L. D. Peel, “Numerical analysis of ballistic impact performance of two ceramic-based armor structures,” *Composites Part C: Open Access*, vol. 3, p. 100 061, 2020. DOI: 10.1016/j.jcomc.2020.100061. [Online]. Available: https://www.sciencedirect.com/science/article/pii/S2666539520300061.

[99] W. Liu, Z. Chen, Z. Chen, *et al.*, “Influence of different back laminate layers on ballistic performance of ceramic composite armor,” *Materials and Design*, vol. 202, p. 109 537, 2021. DOI: 10.1016/j.matdes.2021.109537. [Online]. Available: https://www.sciencedirect.com/science/article/pii/S0264127521001642.

[100] P. J. de Groot, P. A. M. Wijnen, and R. B. F. Janssen, “Real-time frequency determination of acoustic emission for different fracture mechanisms in carbon/epoxy composites,” *Composites Science and Technology*, vol. 55, no. 4, pp. 405–412, 1995. DOI: 10.1016/0266-3538(95)00121-2.

[101] T. Lässig, L. Nguyen, M. May, *et al.*, “A non-linear orthotropic hydrocode model for ultra-high molecular weight polyethylene in impact simulations,” *International Journal of Impact Engineering*, vol. 103, pp. 149–160, 2017. DOI: 10.1016/j.ijimpeng.2017.01.018.

[102] R. Yuan, Y. Wen, W. Nie, D. Liu, Z. Shen, and H. Xu, “Dynamic response of armor-piercing bullets to blunt and penetration with protective gelatin,” *Defence Technology*, vol. 18, no. 11, pp. 2085–2095, 2022. DOI: 10.1016/j.dt.2021.11.014.

[103] University of Colorado Boulder, *Example input file: Impact on silicon carbide (jh2 model)*, https://ceae-server.colorado.edu/v2016/books/eif/exa_impactsiliconcarbide_jh2.inp, Accessed: 2025-05-23, 2016.

Appendix A

Simulating Hybrid Laminates in Abaqus

A.1 Accessing the JH-2 Failure Criterion

Accessing the JH-2 damage model within Abaqus is not a straightforward task, as this material model is not available through the standard GUI. To implement it, one must manually modify the input (`.inp`) file generated by Abaqus. The following section, Section A.2, outlines the complete procedure to achieve this.

The first step, still within the Abaqus CAE environment, is to define a new material that will later be linked to the JH-2 model. This material does not require any predefined properties at this stage. However, it must be named using the exact format: `ABQ_JH2_<userdefinedname>`, for example, `ABQ_JH2_siliconcarbide`.

Note that the prefix `ABQ_JH2_` is not case-sensitive. Abaqus interprets both uppercase and lowercase letters equally for this identifier, so `abq_jh2_` or `ABQ_JH2_`, will be accepted as valid.

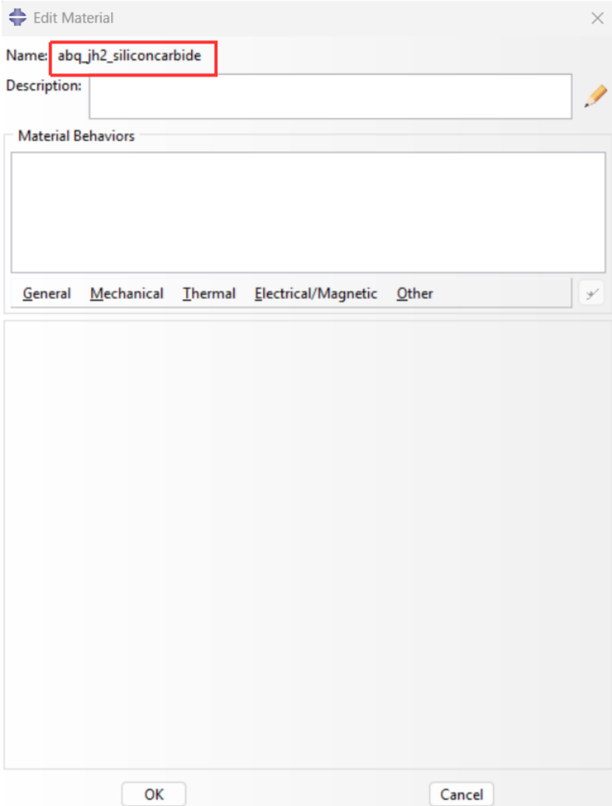

Figure A.1: Material creation in Abaqus CAE.

The prefix `ABQ_JH2_` is essential, as it acts as an identifier linking the material definition in Abaqus to the JH-2 model. This material is then assigned to a specific section of the model in the usual way.

After setting up the model, instead of submitting the job directly, the user must create a job and select the "Write Input" option. This generates the `.inp` file in the working directory without launching the simulation.

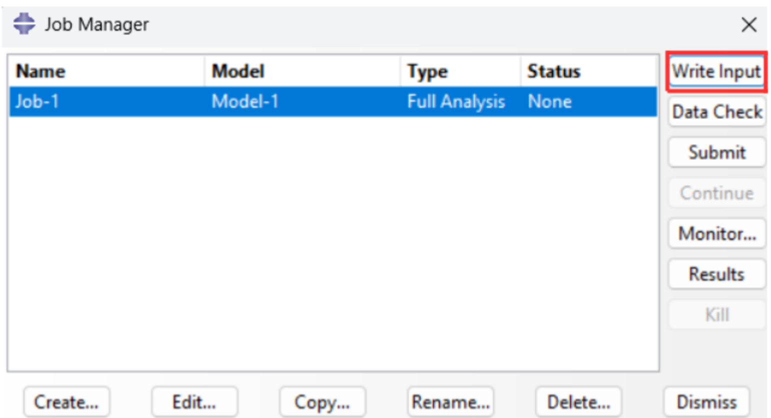

Figure A.2: Writing the input file in Abaqus Job module.

A.2 Editing the Input File

Once the input file has been generated, it is necessary to open it in a text editor (such as Notepad++, Visual Studio Code, Sublime Text, or any code editor of choice) and locate the `*MATERIALS` section. This section contains the material definitions used in the model.

```
*Material, name=abq_jh2_siliconcarbide
```

Listing A.1: Start of the *Material definition block.

Within this section, a specific code block must be added to define the JH-2 model. The required lines are documented in the official Abaqus manual under section "2.1.18 – High-Velocity Impact of a Ceramic Target" [103].

The default code provided in the documentation corresponds to silicon carbide, but it can be adapted to other ceramic materials by adjusting the input parameters accordingly. A example of the code block for silicon carbide is shown below:

```
** MATERIALS
**
*******************************************
*parameter
rho0 = 3.215e-9
G = 193000.
A = 0.96
N = 0.65
B = 0.35
M = 1.0
C = 0.009
edot0 = 1.0
T = 750
sigIMax = 1.23795
sigFMax = 0.1319127
**sigHEL=1.5*(HEL-PHEL)
**sigIMax=sigIMax/sigHEL=12200/9855=1.23795
**sigFMax=sigFMax/sigHEL=1300/9855=0.1319127
HEL = 11700
PHEL = 5130
beta = 1.0
D1 = 0.48
D2 = 0.48
efMax = 1.2
efMin = 0.0
K1 = 220000
```

```
K2 = 361000
K3 = 0.0
FS = 0.2
lDamage = 0
*Material, name=abq_jh2_siliconcarbide
*density
 <rho0>
*user material, constants=32
 <rho0>, <G>, <A>, <N>, <B>, <M>, <C>, <edot0>
 <T>, <sigIMax>, <sigFMax>, <HEL>, <PHEL>, <beta>
 <D1>, <D2>, <efMax>, <efMin>, <FS>, <lDamage>
 <K1>, <K2>, <K3>
*DEPVAR, DELETE=8
8
1, PEEQ , "Equivalent plastic strain"
2, PEEQ_RATE, "Equivalent plastic strain rate"
3, DUCTCRT , "Ductile damage initiation criterion"
4, DAMAGE , "Damage variable"
5, DELTAP , "Pressure increment due to bulking"
6, YIELD , "Yield strength"
7, EVOL , "Volumetric Strain, Mu"
8, MPSTATUS , "Material point status"
*******************************************
```

Listing A.2: Abaqus input block defining the Johnson–Holmquist II ceramic model for silicon carbide.

This code must be inserted directly under the material name defined previously (e.g., `abq_jh2_siliconcarbide`). Care must be taken to preserve the correct formatting and parameter order, as any mistake will result in simulation errors.

After inserting the JH-2 block, the input file must be saved before proceeding to simulation. Failing to save the file after editing will result in the model being run without the newly defined material behaviour.

A.3 Running the Simulation

Once the input file has been updated and saved, the simulation must be executed using the Abaqus command line interface. There are two possible scenarios depending on whether a user-defined material subroutine (VUMAT) is used or not.

A.3.1 Without VUMAT

If the model does not require any additional subroutines beyond the input file definition, the simulation must be run via the Windows Command Prompt. This is necessary because the

Abaqus graphical interface (CAE) cannot be used in this case: submitting the job through the GUI will regenerate the input file and overwrite the manual changes previously made. The correct command to launch the simulation is shown in Figure A.3.

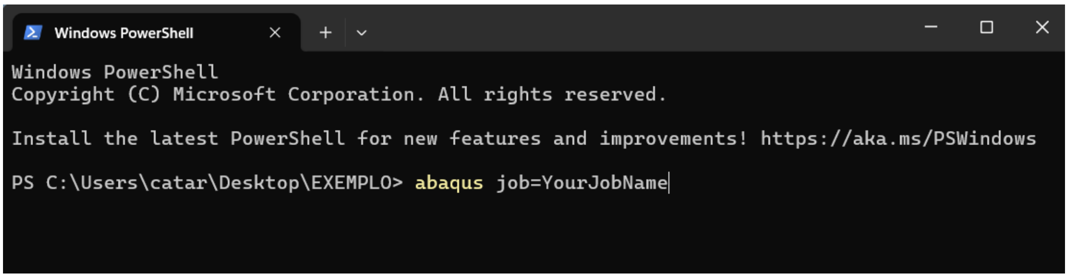

Figure A.3: Running simulation without VUMAT in the Windows Command Prompt.

Here, `YourJobName` refers to the name of the `.inp` file, without the extension. The file must be located in the working directory, and any changes made to it must be saved before executing the command. To enable parallelisation and reduce computation time, the number of CPU cores can be specified with the `cpus=` flag, as shown in Figure A.4.

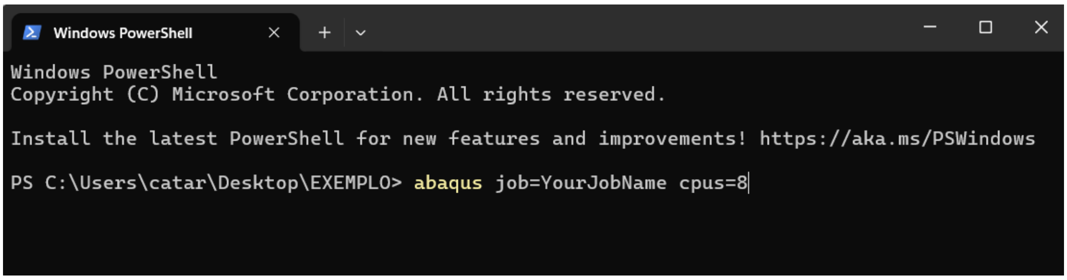

Figure A.4: Running simulation without VUMAT in the Windows Command Prompt with specified number of CPUs.

This will run the job using eight processors. Always ensure that the output files, such as, `.log` and `.msg` are reviewed to confirm the simulation ran correctly.

A.3.2 With VUMAT

If the simulation requires a user-defined material subroutine, such as the implementation of the JH-2 model in Fortran, the job must be run via the Windows Command Prompt using the `user=` flag. This method allows Abaqus to compile and link the external subroutine before running the simulation. The correct command to execute the job is shown in Figure A.5.

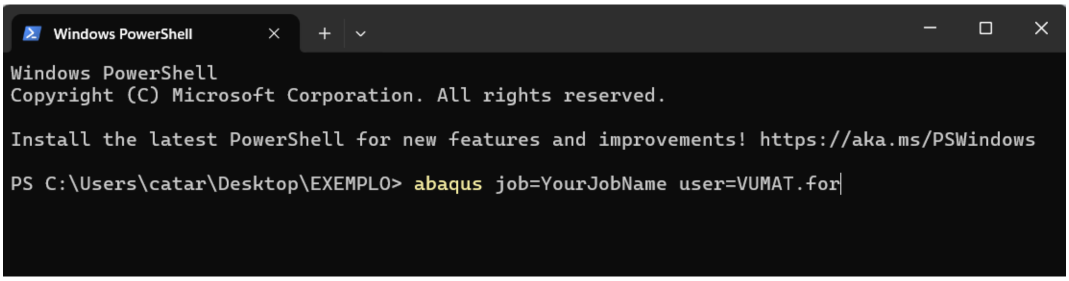

Figure A.5: Running simulation with VUMAT in the Windows Command Prompt.

In this case, `YourJobName` refers to the name of the .inp file, and `VUMAT.for` is the Fortran file containing the material model logic. Both files must be saved and placed in the working directory before executing the command. If desired, the simulation can be parallelised by including the `cpus=` option, as shown in Figure A.6.

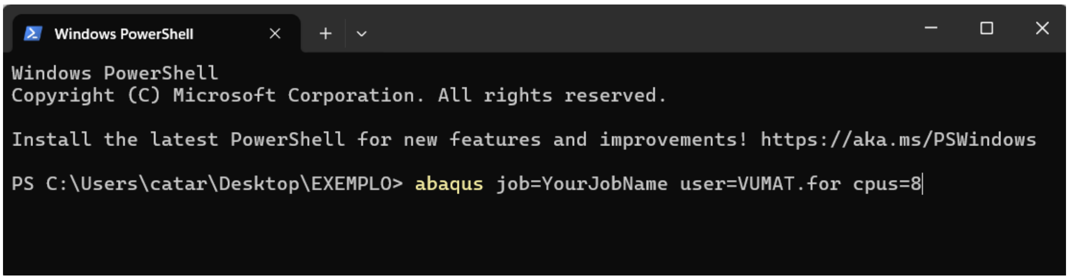

Figure A.6: Running simulation with VUMAT in the Windows Command Prompt with specified number of CPUs.

This command will run the job using eight processors, improving performance for more computationally demanding simulations. After execution, output files such as `.log`, `.msg`, and `.sta` should be checked to ensure the subroutine compiled correctly and the job ran as expected.

Appendix B

VUMAT Subroutine

The following VUMAT subroutine was developed by Mário Miranda and used in this work to implement a user-defined material model for simulating the ballistic behaviour of hybrid laminates in Abaqus/Explicit. The full Fortran source code is presented below.

```
      subroutine vumat(
C Read only (unmodifiable)variables -
     1 nblock, ndir, nshr, nstatev, nfieldv, nprops, lanneal,
     2 stepTime, totalTime, dt, cmname, coordMp, charLength,
     3 props, density, strainInc, relSpinInc,
     4 tempOld, stretchOld, defgradOld, fieldOld,
     5 stressOld, stateOld, enerInternOld, enerInelasOld,
     6 tempNew, stretchNew, defgradNew, fieldNew,
C Write only (modifiable) variables -
     7 stressNew, stateNew, enerInternNew, enerInelasNew )
C
  include 'vaba_param.inc'
******************************************
** 3D Orthotropic material with Hashin 3D failure criterion **
**                  **
** Mario Miranda, University Charles III Madrid **
** **
**Adapted from the Dr.-Ing. Ronald Wagner HashinVumat.for open access script **
*******************************************
```

```
C
C State variables stored as
C state(*,1) = material point status
C state(*,2:7) = damping stresses
C User defined material properties
C props(1) Young's Modulus E1
C props(2) Young's Modulus E2
C props(3) Poisson's ratio nu12
C props(4) Poisson's ratio nu23
C props(5) Shear modulus G12
C props(6) Shear modulus G23
C props(7) Fibre tensile stress Xt
C props(8) Fibre compressesive stress Xc
C props(9) Tranverse tensile stress mt
C propos(10) Tranverse compressive stress
C props(11) Matrix shear stress 12 S12
C props(12) Matrix shear sress 23 S23
C props(13) Fracture toughness E fibre tension Gft
C props(14) Fracture toughness E fibre compression Gfc
C props(15) Fracture toughness E matrix tension Gmt
C props(16) Fracture toughness E matrix compression Gmc

C
      dimension props(nprops), density(nblock), coordMp(nblock,*),
     1 charLength(nblock), strainInc(nblock,ndir+nshr),
     2 relSpinInc(nblock,nshr), tempOld(nblock),
     3 stretchOld(nblock,ndir+nshr),
     4 defgradOld(nblock,ndir+nshr+nshr),
     5 fieldOld(nblock,nfieldv), stressOld(nblock,ndir+nshr),
     6 stateOld(nblock,nstatev), enerInternOld(nblock),
     7 enerInelasOld(nblock), tempNew(nblock),
     8 stretchNew(nblock,ndir+nshr),
     8 defgradNew(nblock,ndir+nshr+nshr),
     9 fieldNew(nblock,nfieldv),
     1 stressNew(nblock,ndir+nshr), stateNew(nblock,nstatev),
     2 enerInternNew(nblock), enerInelasNew(nblock)
C
      character*80 cmname
*
  parameter (zero = 0.d0, one = 1.d0, two= 2.d0, half=.5d0)

  parameter(
     * i_svd_dmgfT = 1,
     * i_svd_dmgfC = 2,
     * i_svd_dmgmT = 3,
```

```
     * i_svd_dmgmC = 4,
     * i_svd_Stress = 5,
c * i_svd_StressXx = 5,
c * i_svd_StressYy = 6,
c * i_svd_StressZz = 7,
c * i_svd_StressXy = 8,
c * i_svd_StressYz = 9,
c * i_svd_StressZx = 10,
     * i_svd_Strain = 11,
c * i_svd_StrainXx = 11,
c * i_svd_StrainYy = 12,
c * i_svd_StrainZz = 13,
c * i_svd_StrainXy = 14,
c * i_svd_StrainYz = 15,
c * i_svd_StrainZx = 16,
     & i_svd_deq0 = 17,
     & i_svd_dfeq = 18,
     & i_svd_deqm0 = 19,
     & i_svd_dfeqm = 20,
     & i_svd_ftrigger = 21,
     & i_svd_ttrigger = 22,
     & i_svd_beta2 = 23,
     & i_svd_beta3 = 24,
     & i_svd_status_el = 25,
     * n_svd_required = 25)


* Read material properties
*
       E1 = props(1)
   E2 = props(2)
   E3 = E2
   xnu12 = props(3)
   xnu13 = xnu12
   xnu23 = props(4)
   G12 = props(5)
   G13 = G12
   G23 = props(6)
   xnu21 = xnu12 * E2 / E1
   xnu31 = xnu13 * E3 / E1
   xnu32 = xnu23 * E3 / E2

* Coupon test values
  ft = props(7)
  fc = props(8)
```

```
  tt = props(9)
  tc = props(10)
      f12 = props(11)
  f23 = props(12)
* Fracture toughness values
  Gft = props(13)
  Gfc = props(14)
  Gmt = props(15)
  Gmc = props(16)

* Elastic step at the beginning of the analysis
    a= zero
         if (totalTime .eq. zero) then
       if (nstatev .lt. n_svd_requiered) then
      call xplb_abqerr(-2,'Subroutine VUMAT requires the ' //
     & 'specification of %I state variables. Check the ' //
     & 'definition of *DEPVAR in the input file.',
     & n_svd_Required,zero,' ')
             call xplb_exit
       end if
       call Ortelas ( nblock,
     & stateOld(1,i_svd_dmgfT),
     & stateOld(1,i_svd_dmgfC),
     & stateOld(1,i_svd_dmgmT),
     & stateOld(1,i_svd_dmgmC),
     & E1,E2,E3,xnu12,
     & xnu21, xnu13, xnu31,xnu23,xnu32,
     & G12, G23, G13,stateOld(1,i_svd_Strain), strainInc,dt,
     & stressNew,stateOld(1,i_svd_ttrigger),
     & stateNew(1,i_svd_beta2),
     & stateNew(1,i_svd_beta3),stateOld(1,i_svd_beta2),
     & stateOld(1,i_svd_beta3))
        return
      end if

* Update strain
       call strainUpdate (nblock, strainInc,
     & stateOld(1,i_svd_Strain), stateNew(1,i_svd_Strain))

* Stress Update
       call Ortelas ( nblock,
     & stateOld(1,i_svd_dmgfT),
     & stateOld(1,i_svd_dmgfC),
     & stateOld(1,i_svd_dmgmT),
     & stateOld(1,i_svd_dmgmC),
```

```
     & E1,E2,E3,xnu12,
     & xnu21, xnu13, xnu31,xnu23,xnu32,
     & G12, G23, G13,stateOld(1,i_svd_Strain),
     & stateNew(1,i_svd_Strain),dt, stressNew,
     & stateOld(1,i_svd_ttrigger),stateNew(1,i_svd_beta2),
     & stateNew(1,i_svd_beta3),stateOld(1,i_svd_beta2),
     & stateOld(1,i_svd_beta3))


* Failure evaluation
      call copyr ( nblock,
     * stateOld(1,i_svd_dmgfT),stateNew(1,i_svd_dmgfT))
      call copyr ( nblock,
     * stateOld(1,i_svd_dmgfC),stateNew(1,i_svd_dmgfC))
      call copyr ( nblock,
     * stateOld(1,i_svd_dmgmT),stateNew(1,i_svd_dmgmT))
      call copyr ( nblock,
     * stateOld(1,i_svd_dmgmC),stateNew(1,i_svd_dmgmC))
      call copyr ( nblock,
     * stateOld(1,i_svd_deq0),stateNew(1,i_svd_deq0))
      call copyr ( nblock,
     * stateOld(1,i_svd_dfeq),stateNew(1,i_svd_dfeq))
      call copyr ( nblock,
     * stateOld(1,i_svd_deqm0),stateNew(1,i_svd_deqm0))
      call copyr ( nblock,
     * stateOld(1,i_svd_dfeqm),stateNew(1,i_svd_dfeqm))
      call copyr ( nblock,
     * stateOld(1,i_svd_ftrigger),stateNew(1,i_svd_ftrigger))
      call copyr ( nblock,
     * stateOld(1,i_svd_ttrigger),stateNew(1,i_svd_ttrigger))

      nDmg = zero
  a=zero
c OPEN (unit=1,file='C:\Users\mario\Desktop\Tese\ABAQUS_FILES\H.txt'
c & ,STATUS='UNKNOWN',ACCESS='APPEND')
c WRITE (1,'(F12.6,2X,F12.6,2X,F12.6,2X,F12.6,2X,F12.6)')
c * ft
c CLOSE(1)
      call hashin3d (nblock, nDmg,
     * ft, fc, f12, f23, tt, tc,
     * stateNew(1,i_svd_dmgfT),
     * stateNew(1,i_svd_dmgfC),
     * stateNew(1,i_svd_dmgmT),
     * stateNew(1,i_svd_dmgmC),Gft,Gfc,Gmt,Gmc,
     * stressNew,stateOld(1,i_svd_Strain),stateNew(1,i_svd_Strain),
```

```
     * dt,charLength,
     * stateNew(1,i_svd_deq0),stateNew(1,i_svd_dfeq),
     * stateNew(1,i_svd_deqm0),stateNew(1,i_svd_dfeqm),
     * stateNew(1,i_svd_ftrigger),stateNew(1,i_svd_ttrigger), stateNew
         (1,i_svd_status_el))
* -- Recompute stresses if new Damage is occurring
      if ( nDmg .gt. zero ) then
         a=one
       call Ortelas ( nblock,
     & stateOld(1,i_svd_dmgfT),
     & stateOld(1,i_svd_dmgfC),
     & stateOld(1,i_svd_dmgmT),
     & stateOld(1,i_svd_dmgmC),
     & E1,E2,E3,xnu12,
     & xnu21, xnu13, xnu31,xnu23,xnu32,
     & G12, G23, G13,stateOld(1,i_svd_Strain),
     & stateNew(1,i_svd_Strain),dt, stressNew,
     & stateNew(1,i_svd_ttrigger),stateNew(1,i_svd_beta2),
     & stateNew(1,i_svd_beta3),stateOld(1,i_svd_beta2),
     & stateOld(1,i_svd_beta3))

        end if



* Integrate the internal specific energy (per unit mass)
*
      call EnergyInternal3d ( nblock, stressOld, stressNew,
     * strainInc, density, enerInternOld, enerInternNew )
*
      return
  end

***********************************
* Ortelas: Orthotropic elasticity *
***********************************
  subroutine Ortelas(nblock, dmgfT, dmgfC, dmgmT, dmgmC, E1,E2,E3,xnu12,
     & xnu21, xnu13, xnu31,xnu23,xnu32,
     & G12, G23, G13,strainold, strain,dt, stress,ttrigger,beta2,beta3,
     & beta2old,beta3old)

        include 'vaba_param.inc'

   parameter( zero = 0.d0, one = 1.d0, two = 2.d0, dec=.1d0,
     & hundred=100.d0, fac=1.29d0)
```

```

   dimension strain(nblock,6), dmgfT(nblock), dmgfC(nblock),
     & dmgmT(nblock), dmgmC(nblock), stress(nblock,6),
     & strainold(nblock,6),beta2(nblock), beta3(nblock),
     & beta2old(nblock), beta3old(nblock),ttrigger(nblock)

       parameter ( smt = 0.3d0, smc = 0.3d0 )
      do k = 1, nblock
* Damage variables
     dft = dmgfT(k)
     dfc = dmgfC(k)
     dmt = dmgmT(k)
     dmc = dmgmC(k)
         df = ( one - dft ) * ( one - dfc )
         dm = (one - smt*dmt) * (one - smc*dmc)
         gg=one-df*dm*xnu12*xnu21-dm*xnu23*xnu32-df*xnu31*xnu13-
     & two*df*dm*xnu21*xnu32*xnu13
         gginv= one / gg

* Strain rate effect
         beta2(k)=one
         beta3(k)=one
         if (ttrigger(k) .lt. one) then
           if (dt .gt. zero) then
            srate2= abs(strain (k,2)-strainold (k,2))/dt
            srate3= abs(strain (k,3)-strainold (k,3))/dt

             if ( srate2 .gt. dec) then
             beta2(k)=(srate2-dec)*(fac-one)/(hundred-dec)+one
             end if
             if ( srate2 .ge. hundred) then
             beta2(k)=fac
            end if

            if ( srate3 .gt. dec) then
            beta3(k)=(srate3-dec)*(fac-one)/(hundred-dec)+one
             end if
             if ( srate3 .ge. hundred) then
             beta3(k)=fac
             end if
           end if

           else if (ttrigger(k) .ge. one) then
               beta2(k) =beta2old(k)
               beta3(k)=beta3old(k)
```

```
      end if
c OPEN (unit=1,file='C:\Users\mario\Desktop\Tese\ABAQUS_FILES\H.txt'
c & ,STATUS='UNKNOWN',ACCESS='APPEND')
c WRITE (1,'(F12.6,2X,F12.6,2X,F12.6,2X,F12.6,2X,F12.6)')
c * beta2,srate2, beta3,srate3
c CLOSE(1)
* Damaged stiffness matrix
        dC11 = gginv*df*E1*(one-dm*xnu23*xnu32)
        dC22 = gginv*dm*beta2(k)*E2*(one-df*xnu13*xnu31)
        dC33 = gginv*beta2(k)*E3*(one-df*dm*xnu12*xnu21)
        dC12 = gginv*df*dm*E1*(xnu21+xnu23*xnu31)
        dC23 = gginv*dm*beta2(k)*E2*(xnu32+df*xnu12*xnu31)
        dC13 = gginv*df*E1*(xnu31+dm*xnu21*xnu32)
        dG12 = df*dm*G12
        dG23 = df*dm*G23
        dG13 = df*dm*G13
c OPEN (unit=1,file='C:\Users\mario\Desktop\Tese\ABAQUS_FILES\H.txt'
c & ,STATUS='UNKNOWN',ACCESS='APPEND')
c WRITE (1,'(F12.1,2X,F12.6,2X,F12.6,2X,F12.6,2X,F12.6)')
c * dC11,df,dC22,dm,dC33
c CLOSE(1)
* Updated stress calculation
     stress(k,1) = dC11 * strain(k,1) + dC12 * strain (k,2) +
    & dC13 * strain(k,3)

       stress(k,2) = dC12 * strain(k,1) + dC22 * strain(k,2) +
    &  dC23 * strain(k,3)

       stress(k,3) = dC13 * strain(k,1) + dC23 * strain(k,2) +
    & dC33 * strain(k,3)

       stress(k,4) = two* dG12 * strain(k,4)

       stress(k,5) =two* dG23 * strain(k,5)

       stress(k,6) =two* dG13 * strain(k,6)
c OPEN (unit=1,file='C:\Users\mario\Desktop\Tese\ABAQUS_FILES\H.txt'
c & ,STATUS='UNKNOWN',ACCESS='APPEND')
c WRITE (1,'(F12.6,2X,F12.5,2X,F12.5,2X,F12.6,2X,F12.6,2X,F12.6)')
c * beta2, beta3
c CLOSE(1)

     end do

*
```

```
  return


  end

******************************
* strainUpdate: Update strain *
******************************
      subroutine strainUpdate (nblock, strainInc, strainOld, strainNew)
*
        include 'vaba_param.inc'
*
    dimension strainInc(nblock,6), strainOld(nblock,6),
     & strainNew(nblock,6)
*
    do k = 1, nblock
       strainNew(k,1)= strainOld(k,1)
     & + strainInc(k,1)
           strainNew(k,2)= strainOld(k,2)
     & + strainInc(k,2)
           strainNew(k,3)= strainOld(k,3)
     & + strainInc(k,3)
           strainNew(k,4)= strainOld(k,4)
     & + strainInc(k,4)
           strainNew(k,5)= strainOld(k,5)
     & + strainInc(k,5)
           strainNew(k,6)= strainOld(k,6)
     & + strainInc(k,6)

    end do
*
    return
  end



**************************************
* hashin3d: Hashin 3D failure criteria*
**************************************
  subroutine hashin3d (nblock, nDmg,
     & ft, fc, f12, f23, tt, tc,
     & dmgfT, dmgfC, dmgmT, dmgmC,Gft,Gfc,Gmt,Gmc, stress, strainold,
     & strain,dt,charLength,deq0,dfeq,deqm0,dfeqm,ftrigger,ttrigger,
         status_el)

```

```
      include 'vaba_param.inc'

    parameter( zero = 0.d0, one = 1.d0, two = 2.d0,half=.5d0)

    dimension dmgfT(nblock), dmgfC(nblock), dmgmT(nblock), dmgmC(nblock),
      & dmgfTold(nblock), dmgfCold(nblock),
      & dmgmTold(nblock), dmgmCold(nblock),
      & stress(nblock,6), strain(nblock,6), charLength(nblock),
      & ftrigger(nblock), ttrigger(nblock), strainold(nblock,6),
      & status_el(nblock)

    do k = 1, nblock

      e11=strain(k,1)
      e22=strain(k,2)
      e33=strain(k,3)
      e12=strain(k,4)
      e23=strain(k,5)
      e13=strain(k,6)

      s11= stress(k,1)
      s22= stress(k,2)
      s33= stress(k,3)
      s12= stress(k,4)
      s23= stress(k,5)
            s13= stress(k,6)
* Effect of strain rate
            sratef=abs((strain (k,1)-strainold (k,1))/dt)
            sratem2=abs((strain (k,2)-strainold (k,2))/dt)
            sratem3=abs((strain (k,3)-strainold (k,3))/dt)

            srf=(sratef-.1d0)/(100.d0-.1d0)
            srmax=MAX(sratem2,sratem3)
            srm=(srmax-.1d0)/(100.d0-.1d0)
* Fibre direction strain rate
            fti=ft
            fci=fc
            if ( sratef .gt. .1d0) then
              fti=(srf*.38d0+one)*ft
              fci=(srf*.39d0+one)*fc
              end if
          if ( sratef .ge. 100d0) then
              fti=1.38d0*ft
              fci=1.39d0*fc
          end if
```

```
* Matrix direction strain rate
        tti=tt
        tci=tc
        Gmti=Gmt
        Gmci=Gmc
         if ( srmax .gt. .1d0) then
            tti=(srm*.38d0+one)*tt
            tci=(srm*.37d0+one)*tc
            Gmti=(srm*.23d0+one)*Gmt
            Gmci=(srm*.63d0+one)*Gmc
         end if
          if (srmax .ge. 100d0) then
            tti=1.38d0*tt
            tci=1.37d0*tc
            Gmti=1.23d0*Gmt
            Gmci=1.63d0*Gmc
        end if

* Turn inv values into double precision
          ftinv=one/fti
          fcinv=one/fci
          ttinv=one/tti
          tcinv=one/tci
          f12inv=one/f12
    f23inv= one/f23
* Store previous iteration damage values
          dmgfTold(k)=dmgfT(k)
    dmgfCold(k)=dmgfC(k)
          dmgmTold(k)=dmgmT(k)
          dmgmCold(k)=dmgmC(k)
* Fibre modes
       if ( s11 .gt. zero) then
* Fibre tension
    ftf = (s11*ftinv)**2 +(s12*f12inv)**2 +(s13*f12inv)**2
       if (ftrigger(k) .le. zero) then
          if (ftf .ge. one) then
              ftrigger(k) = one
              dmg = 1
C Macauley operator
              if (e11 .lt. zero) then
                       e11=zero
              end if
              if (s11 .lt. zero) then
                     s11=zero
              end if
```

```
C Equivalent measures
         deq=charLength(k)*sqrt(e11**2+e12**2+e13**2)
               deqinv=one/deq
       seq=charLength(k)*(s11*e11+s12*e12+s13*e13)*deqinv
       seq0=seq/sqrt(ftf)
       deq0=deq/sqrt(ftf)
       seq0inv=one/seq0
       dfeq=two*Gft*seq0inv
       dmgfT(k)=(dfeq * (deq-deq0))/(deq * (dfeq-deq0))
c OPEN (unit=1,file='C:\Users\mario\Desktop\Tese\ABAQUS_FILES\H.txt'
c & ,STATUS='UNKNOWN',ACCESS='APPEND')
c WRITE (1,'(F12.6,2X,F12.6,2X,F12.6,2X,F12.6,2X,F12.6)')
c * s12,f12inv
c CLOSE(1)
      end if
        else if (ftrigger(k) .ge. one) then
             if (e11 .lt. zero) then
                        e11=zero
               end if
               if (s11 .lt. zero) then
                      s11=zero
                   end if
               dmg = 1
         deq=charLength(k)*sqrt(e11**2+e12**2+e13**2)
       dmgfT(k)=(dfeq * (deq-deq0))/(deq * (dfeq-deq0))

           dmgfT(K) = MIN(dmgfT(K),one)
           dmgfT(K) = MAX(dmgfT(K),zero)
           dmgfT(K) = MAX(dmgfT(K),dmgfTold(K))
c OPEN (unit=1,file='C:\Users\mario\Desktop\Tese\ABAQUS_FILES\H.txt'
c & ,STATUS='UNKNOWN',ACCESS='APPEND')
c WRITE (1,'(F12.6,2X,F12.6,2X,F12.6,2X,F12.6,2X,F12.6)')
c * ft,dmgfT(k)
c CLOSE(1)
      end if

          else if (s11 .lt. zero) then
* Fibre compression

              fcf= abs(s11)*fcinv
            if (ftrigger(k) .le. zero) then
        if (fcf .ge. one) then
                  ftrigger(k) = one
        dmg = 1
                    if (-e11 .lt. zero) then
```

```
                        e11=zero
                   end if
                     if (-s11 .lt. zero) then
                      s11=zero
                    end if
         deq=charLength(k)*abs(e11)
         deqinv= one/deq

          seq=charLength(k)*s11*e11*deqinv
        seq0=seq/sqrt(fcf)
        deq0=deq/sqrt(fcf)
        seq0inv=one/seq0
        dfeq=two*Gfc*seq0inv
        dmgfC(k)=(dfeq * (deq-deq0))/(deq * (dfeq-deq0))
                  end if
             else if (ftrigger(k) .ge. one) then
                 if (-e11 .lt. zero) then
                        e11=zero
                 end if
                 if (-s11 .lt. zero) then
                       s11=zero
                     end if
                    dmg = 1
         deq=charLength(k)*abs(e11)
        dmgfC(k)=(dfeq * (deq-deq0))/(deq * (dfeq-deq0))
            dmgfC(K) = MIN(dmgfC(K),one)
            dmgfC(K) = MAX(dmgfC(K),zero)
            dmgfC(K) = MAX(dmgfC(K),dmgfCold(K))
           end if
         end if


* Matrix modes
       if ( (s22+s33) .ge. zero ) then
* Matrix tension
      ttf=((s22+s33)*ttinv)**2 + (s23**2 - s22*s33)*(f23inv**2)+
      & (s12**2+s13**2)*(f12inv**2)
         if (ttrigger(k) .le. zero) then

             if (ttf .ge. one) then
       dmg=1
               ttrigger(k) = one
            if (e22 .lt. zero) then
                        e22=zero
            end if
```

```
          if (s22 .lt. zero) then
                    s22=zero
          end if
          if (e33 .lt. zero) then
                      e33=zero
          end if
          if (s33 .lt. zero) then
                    s33=zero
          end if

     deqm=charLength(k)*sqrt((e22)**2+(e33)**2+e12**2+e23**2+
    &   e13**2)
     deqminv=one/deqm
      seqm=charLength(k)*((s22)*(e22)+(s33)*(e33)+
    & s12*e12+s23*e23+s13*e13)*deqminv

      seqm0=seqm/sqrt(ttf)
      deqm0=deqm/sqrt(ttf)
             seqm0inv=one/seqm0
      dfeqm=two*Gmti*seqm0inv+deqm0
      dmgmT(k)=dfeqm*(deqm-deqm0)/(deqm*(dfeqm-deqm0))
c OPEN (unit=1,file='C:\Users\mario\Desktop\Tese\ABAQUS_FILES\H.txt'
c & ,STATUS='UNKNOWN',ACCESS='APPEND')
c WRITE (1,'(F12.6,2X,F12.6,2X,F12.6,2X,F12.6,2X,F12.6)')
c * seqm0,deqm0,dfeqm
c CLOSE(1)
         end if
      else if (ttrigger(k) .ge. one) then
            dmg=1
           if (e22 .lt. zero) then
                      e22=zero
          end if
          if (s22 .lt. zero) then
                    s22=zero
          end if
          if (e33 .lt. zero) then
                      e33=zero
          end if
          if (s33 .lt. zero) then
                    s33=zero
          end if
     deqm=charLength(k)*sqrt((e22)**2+(e33)**2+e12**2+e23**2+
    &   e13**2)
      dmgmT(k)=dfeqm*(deqm-deqm0)/(deqm*(dfeqm-deqm0))
c OPEN (unit=1,file='C:\Users\mario\Desktop\Tese\ABAQUS_FILES\H.txt'
```

```
c & ,STATUS='UNKNOWN',ACCESS='APPEND')
c WRITE (1,'(F12.6,2X,F12.6,2X,F12.6,2X,F12.6,2X,F12.6)')
c * seqm0,deqm0,dfeqm
c CLOSE(1)
          dmgmT(k) = MIN(dmgmT(k),one)
          dmgmT(k) = MAX(dmgmT(k),zero)
          dmgmT(k) = MAX(dmgmT(k),dmgmTold(k))
      end if

      else if ( (s22+s33) .lt. zero ) then
* Matrix compression

           tcf = tcinv *(s22+s33)*((tci/(two*f23))**2 - one) +
     & ((s22+s33)/(two*f23))**2+ (s23**2-s22*s33)*(f23inv**2)+
     &  (s12*f12inv)**2 + (s13*f12inv)**2
         if (ttrigger(K) .le. zero) then
      if (tcf .ge. one) then

     dmg=1
            ttrigger(k) = one
             if (-e22 .lt. zero) then
                      e22=zero
          end if
          if (-s22 .lt. zero) then
                    s22=zero
          end if
          if (-e33 .lt. zero) then
                      e33=zero
          end if
          if (-s33 .lt. zero) then
                    s33=zero
          end if
          deqm=charLength(k)*sqrt((-e22)**2+(-e33)**2+e12**2+e23**2+
     & e13**2)
            deqminv=one/deqm
      seqm=charLength(k)*((-s22)*(-e22)+(-s33)*(-e33)+
     & s12*e12+s23*e23+s13*e13)*deqminv
      seqm0=seqm / sqrt(tcf)
      deqm0=deqm / sqrt(tcf)
             seqm0inv=one/seqm0
      dfeqm=two*Gmci*seqm0inv+deqm0
      dmgmC(k)=dfeqm*(deqm-deqm0)/(deqm*(dfeqm-deqm0))

            end if
         else if (ttrigger(k) .ge. one) then
```

```
              dmg=1
          if (-e22 .lt. zero) then
                      e22=zero
          end if

          if (-s22 .lt. zero) then
                    s22=zero
          end if
          if (-e33 .lt. zero) then
                      e33=zero
          end if
          if (-s33 .lt. zero) then
                    s33=zero
          end if
             deqm=charLength(k)*sqrt((-e22)**2+(-e33)**2+e12**2+e23**2+
     & e13**2)
       dmgmC(k)=dfeqm*(deqm-deqm0)/(deqm*(dfeqm-deqm0))
           dmgmC(k) = MIN(dmgmC(k),one)
           dmgmC(k) = MAX(dmgmC(k),zero)
           dmgmC(k) = MAX(dmgmC(k),dmgmCold(k))

            end if
       end if

       if ((dmgfT(k) .ge. 0.99) .or. (dmgfC(k) .ge. 0.99)
     & .or. (dmgmT(k) .ge. 0.99) .or. (dmgmC(k).ge. 0.99)) then
       status_el(k) = 0.0
       else
         status_el(k) = 1.0
       end if

            nDmg = nDmg + dmg

    end do
    return
    end

************************************************************
* CopyR: Copy from one array to another *
************************************************************
      subroutine CopyR(nCopy, from, tom )
*
      include 'vaba_param.inc'
*
      dimension from(nCopy), tom(nCopy)
```

```
*
      do k = 1, nCopy
         tom(k) = from(k)
      end do
*
      return
      end

***********************************************************
* EnergyInternal3d: Compute internal energy for 3d case *
***********************************************************

  subroutine EnergyInternal3d(nblock, sigOld, sigNew ,
     * strainInc, curDensity, enerInternOld, enerInternNew)
*
       include 'vaba_param.inc'
*

      parameter( two = 2.d0, half = .5d0 )
*
      dimension sigOld (nblock,6), sigNew (nblock,6),
     * strainInc (nblock,6), curDensity (nblock),
     * enerInternOld(nblock), enerInternNew(nblock)
*
      do k = 1, nblock
         stressPower = half * (
     * ( sigOld(k,1) + sigNew(k,1) )
     * * ( strainInc(k,1) )
     * + ( sigOld(k,2) + sigNew(k,2) )
     * * ( strainInc(k,2))
     * + ( sigOld(k,3) + sigNew(k,3) )
     * * ( strainInc(k,3))
     * + two*( sigOld(k,4) + sigNew(k,4) )
     * * strainInc(k,4)
     * + two*( sigOld(k,5) + sigNew(k,5) )
     * * strainInc(k,5)
     * + two*( sigOld(k,6) + sigNew(k,6) )
     * * strainInc(k,6) )
*
         enerInternNew(k) = enerInternOld(k) + stressPower/curDensity(k)
      end do
*
      return
       end
```

Listing B.1: VUMAT subroutine.

This subroutine was compiled and linked to the simulation using the `user=` flag in the Abaqus command line, as described in Appendix A.